ALMA MATER STUDIORUM
UNIVERSITÀ DI BOLOGNA

DOTTORATO DI RICERCA IN

MECCANICA E SCIENZE AVANZATE DELL'INGEGNERIA

Ciclo 38

Settore Concorsuale: 09/B1 - TECNOLOGIE E SISTEMI DI LAVORAZIONE

Settore Scientifico Disciplinare: ING-IND/16 - TECNOLOGIE E SISTEMI DI LAVORAZIONE

EXPERIMENTAL AND NUMERICAL INVESTIGATION OF ADHESIVELY BONDED JOINT FOR HIGH VOLUMES AUTOMOTIVE APPLICATIONS

Presentata da: Michele Tropeano

Coordinatore Dottorato

Lorenzo Donati

Supervisore

Lorenzo Donati

Co-supervisore

Andrea Zucchelli

Esame finale anno 2026

Abstract

The automotive industry's increasing adoption of lightweight materials like carbon fiber composites, especially employing Sheet Molding Compound for high productivity, necessitate advanced joining technologies for high structural performance and safety. This thesis presents an integrated methodology combining experimental characterization, numerical modeling and optimization to develop a predictive model for structural adhesives, specifically addressing manufacturing-induced non-uniformities in bondline thickness. The research focuses on the quasi-static and fracture behavior of bonded joints, primarily using ductile polyurethane-based adhesive commonly employed with carbon fiber components. An extensive experimental campaign, utilizing standardized tests under various conditions (temperature, bondline thickness, surface preparation), provided data for calibrating and validating Finite Element models in Abaqus. Cohesive Zone Models were implemented to simulate fracture initiation and propagation. An inverse calibration procedure, facilitated by HyperStudy optimization software, was developed to systematically generate a validated "material card" (a set of constitutive parameters) that accurately describes adhesive behavior in Finite Element simulations, relevant to large-scale automotive models. This work addresses the lack in the literature of adhesive models for bonded SMC joints that are both predictive and transferable to industrial-scale FE simulations by explicitly considering manufacturing-induced bondline thickness variability and by developing an optimization-based cohesive zone modeling approach calibrated and validated using multiple experimental test configurations.

Summary

Figure Summary

The following is a list of nomenclatures utilized in this work, specifically useful in Chapter 2:

$\boldsymbol{A} = bonded\ area\ of\ interest\ [mm^2]$

$\boldsymbol{a} = crack\ lenght\ [mm]$

$\boldsymbol{\alpha} =\ non\ dimensional\ parameter\ referred\ to\ the\ softening\ response$

$\boldsymbol{C} =\ compliance, \frac{\delta}{F}, of\ specimen\ \left[\frac{mm}{N}\right]$

$\boldsymbol{D} =\ damage\ variable\ for\ damage\ criterion\ [-]$

$\boldsymbol{\delta, \delta_{cr}} =\ force\ /\ critical\ force\ related\ displacement\ \ [mm]$

$\boldsymbol{\varepsilon} = percentage\ strain\ usually\ referred\ to\ force\ value\ [\%]$
$\boldsymbol{Fmax}\ /\ \boldsymbol{Fcr} = maximum\ /\ critical\ force\ at\ failure\ [N]$
$\boldsymbol{G_{Ic}} = Mode\ I\ interlaminar\ fracture\ energy\ \left[\frac{J}{m^2}\right]$
$\boldsymbol{G_{IIc}} = Mode\ II\ interlaminar\ fracture\ energy\ \left[\frac{J}{m^2}\right]$
$\boldsymbol{h} =\ thickness\ of\ the\ adherend\ material\ [mm]$

$\boldsymbol{K}\ /\ \boldsymbol{K_{xy}} =\ stiffness\ matrix\ /\ matrix\ element\ where\ "x"\ and\ "y"\ can\ represent$

$n = normal\ direction,\ \ s = first\ shear\ direction\ and\ t = second\ shear\ direction$

$\eta\ =\ relevant\ material\ parameter\ in\ the\ BK\ law$

$\boldsymbol{L} =\ total\ lengtht\ \ [mm]$

$\boldsymbol{m} = slope\ of\ plot\ of\ log\left(\frac{C}{N}\right) versus\ log(a)$

$\boldsymbol{\sigma_{max}} = maximum\ tensile\ stress\ at\ failure\ [MPa]$

$\boldsymbol{\tau_{max}} = maximum\ shear\ stress\ at\ failure\ [MPa]$

$\boldsymbol{t} = cohesive\ traction\ [N]$

$\boldsymbol{v} = vertical\ distance\ from\ the\ center\ of\ the\ pin\ hole\ to\ the$

$midplane\ of\ the\ specimen\ arm\ [mm]$

$\boldsymbol{W} = width\ of\ the\ specimen\ [mm]$

Chapter 1: Introduction

Lightweight structural design has become a cornerstone of modern engineering innovation across sectors such as automotive, aerospace and renewable energy. The increasing pressure to reduce greenhouse gas emissions, enhance energy efficiency and to improve product performance has driven a rapid shift toward advanced materials and joining technologies. The widespread adoption of fiber-reinforced polymer (FRP) composites in critical structural components is driven by their exceptional specific strength, corrosion resistance and remarkable versatility in design and performance [1–3].

Sheet Molding Compound (SMC) materials have rapidly gained ground as viable choice for high-volume automotive manufacturing. Its fast-molding cycles, automated process integration and compatibility with recycled fibers enable both economic and environmental advantages. The application of SMC components (body panels, tailgates, fenders and interior structures) has led to measurable improvements in vehicle mass, crash performance and lifecycle sustainability [4–6].

The transition to electric vehicles (EVs) amplifies the demand for lightweight, robust and recyclable composites. SMC plays a pivotal role in the design and manufacture of battery enclosures, underbody shields and mounting structures, all of which require both mechanical protection and electrical insulation properties. In Automotive, SMC is used also to reduce vehicle mass and its tunable thermal conductivity and flame resistance address safety requirements unique to EV platforms. Additionally, SMC enables rapid production of structurally complex components through compression molding, enhancing crash safety and barrier protection for integrated electronic modules.

Maximizing the benefits of FRP and SMC requires reliable joining techniques suitable for complex, load-bearing assemblies. Several authors have numerically and theoretically investigated crack propagation and interface mechanics in adhesively bonded composite joints. For instance, Chen and Dillard [7] used finite element modeling to analyze directionally unstable crack growth, underlining the role of stiffness mismatch at the interface in determining crack path stability.

Mechanical fastening for joining materials, once dominant, faces limitations including stress concentrations, fiber disruption and local delamination [8–10]. The evolution toward advanced adhesives, particularly polyurethane and toughened epoxies, reduces these risks and enables dissimilar materials joints commonly

present in multi-material automotive bodies. Hybrid joints, which combine adhesives and fasteners, are increasingly critical for balancing energy dissipation and crash resistance. Advanced numerical and analytical models have been developed to investigate crack propagation paths and angles under mixed Mode I/II loading, enabling a better understanding of joint behavior and providing engineers with novel criteria for optimization and safe design of hybrid joint geometries [11].

Bonded composite joints are susceptible to a wide range of defects and failure phenomena, including debonding, crack initiation and fatigue-induced delamination [12–16]. Fatigue studies conducted by Azari and Bernasconi [17,18] highlight that cycles of mechanical and environmental loading, coupled with material or process discontinuities, can drastically affect bonded joint service life.

Blackman and Kinloch [19] provided a critical review of fracture tests on structural adhesive joints, discussing how parameter identification for toughness and energy release rates has evolved to support both experimental and computational studies [20–24], with attention to multi-mode and thick-adherend configurations. Heide-Jørgensen and Teixeira de Freitas [25] demonstrated the detrimental impact of bondline discontinuities on crack stability in FRP joints, using modeling to show how micro-defects initiate interface failure. Azevedo [26] performed ENF-type Mode II tests on adhesive composite joints, showing how cohesive law and energy dissipation nonlinearly depend on interface and adhesive properties. Floros [27] characterized Mode I, II and mixed-mode failures with DCB/ENF/mixed-mode specimens, demonstrating geometry and toughening influence on crack onset. Canãs [28] compared symmetric/unsymmetric DCB, proving specimen design affects interlaminar fracture measurements.

Recent studies address the effects of loading rate, temperature and environmental conditions on fracture and fatigue behavior in automotive adhesives. This highlights the influence of high strain rates or thermal cycling on mode II toughness and crack path stability in ductile adhesives, crucial for service reliability in EV assemblies [29,30].

Environmental ageing, humidity and repeated thermal cycling have a pronounced effect on interfacial properties of epoxy adhesives, making the implementation of humidity-degraded cohesive zone elements and cyclic testing a necessity for evaluating modern automotive adhesives [31,32].

The production of SMC-based assemblies in automotive and EV sectors presents a distinct challenge: controlling adhesive gap variability during large-scale bonding. The mechanical response and reliability of SMC and CFRP in automotive adhesively bonded joints are profoundly affected by the adhesive layer thickness and the nature of substrate interfaces [33–39]. Recent research demonstrates that optimal gap control and substrate matching can significantly mitigate stress concentrations and reduce the onset of critical debonding under service conditions. Manufacturing tolerances, surface waviness and geometric complexity can often result in non-uniform bondlines on the adhesive path across complex components [40].

Banea, da Silva and Campilho's studies [41] provide systematic insight into how this gap heterogeneity translates into local stress concentrations, premature crack onset and unpredictable failure under vibration and impact. Mall and Ramamurthy [42] demonstrated that excess adhesive thickness can non-linearly degrade fatigue performance, especially in conditions typical for service life exposure. Wu, Yuan and Niu [43] developed an analytical model for stress transfer and fracture propagation in various adhesive joint configurations, establishing theoretical relations between interface properties and the onset of debonding.

Despite the advantages of SMC in the automotive sector, the transition from laboratory-scale testing to large-scale industrial assembly introduces significant challenges, primarily related to adhesive gap variability and interface consistency. While literature establishes the theoretical influence of bondline thickness, there remains a critical gap in predictive models capable of accounting for the stochastic nature of manufacturing tolerances in complex multi-material geometries. This work is motivated by the necessity to bridge the gap between idealized fracture mechanics and the industrial reality of EV manufacturing, where environmental conditions and process parameters profoundly affect joint integrity.

Non-destructive methods such as acoustic emission and thermography have been increasingly utilized to detect hidden defects in adhesive joints, providing crucial support for early intervention and process optimization in high-value composite assemblies [44]. Studies on adhesive thickness and modulus effects in metal joints show that increasing layer thickness can lower local interface strength (especially in high-performance metallic bonding) making geometric control and tailored adhesive selection critical for both static and fatigue strength [45,46].

Shah and Tarfaoui [47] conducted a comparative study on the effect of adhesive thickness in Mode I and II SERRs, proposing calculation procedures for real-world geometry and delamination response. Liao, Huang and Sawa [48] addressed how scarf angles and adhesive type affect strength and mixed-mode fracture behavior in composite joints, showing by simulation and test that bondline architecture can be tuned to delay crack initiation.

Recent investigations on the mechanical behavior of metal-composite and metal-metal joints highlight that tailored surface treatments and compositional adjustments, including 3D-printed aluminum substrates, can significantly increase mode I fracture toughness and joint reliability even in challenging geometries [49]. In EV applications, where thermal cycling and structural monitoring are stringent, controlling and optimizing the adhesive gap is essential for joint safety and reliability.

Industrial best practices now include process monitoring by sensors, enhanced fixture design and the adoption of more tolerant adhesive formulations. Recently, non-destructive monitoring techniques such as digital image correlation and full-field strain analysis have been successfully applied for the evaluation of mode I and mode II fracture toughness of composite joints, allowing accurate mapping of local fracture energy and providing robust experimental data for CZM calibration in automotive applications [50–53].

Fernández-Cañadas[54] tested single-lap joints to show that both adhesive thickness and overlap must be optimized to prevent efficiency loss or fast crack propagation. Davies[55] demonstrated an optimum bondline thickness, below which joints are weak, above which stress transfer is poor. Tankut [56] emphasized adhesive type and bondline thickness in joint performance.

Recent systematic studies on bondline thickness and ductility, both at the adhesive and adherend scale, demonstrate that toughness and crack onset can be strategically tuned and crack deflection promoted, by controlling thickness parameters alone, providing important criteria for the design of multi-material and thick-bonded assemblies [57–61]. New advances in the assessment of shear and peel strength (thanks to refined interface experimental methods) have promoted the testing of adhesively bonded composite specimens, revealing the effect of bondline on geometrical design on damage and fatigue strength [62–71].

Progress in adhesive and interface engineering (especially high-toughness, nano-modified adhesives and plasma-based surface treatments) continues to improve joint durability and reparability, supporting long-term sustainability strategies [72–75]. The reinforcing action of carbon fibers in composite adhesives does not only increase joint strength, but more importantly, it promotes energy-dissipation mechanisms during crack growth, as demonstrated by recent microstructural investigations and mechanical tests [76].

Further investigations into plasma and chemical surface modification of SMC and CFRP have shown increased interfacial bonding strength, improved ageing resistance and potential for fire retardancy in EV structures [77–80]. A growing body of literature demonstrates that advanced surface modifications and atmospheric plasma treatments of CFRP and SMC dramatically enhance environmental durability, mitigating adhesion loss due to humidity, fatigue or fire. These concepts are of particular importance for the next generation of lightweight and safe automotive structures, especially if accompanied by automated infrastructure for assembly lines technologies [81,82].

These developments open new avenues for composite joints in demanding environmental scenarios and expand the spectrum of adhesives suitable for multi-material automotive assemblies. The convergence of new materials and rigorous process technology has enabled composite designs with enhanced ease of disassembly and recyclability.

A recent focus in the literature is the integration of simulation-driven component design with advanced sensing and process monitoring to address the challenges of large-scale adhesive bonding in automotive SMC and CFRP applications. Data-driven calibration of cohesive zone models, supported by in situ optical and acoustic diagnostics during DCB and ENF testing, has enabled robust identification of damage evolution parameters across a wide range of substrates, including those found in hybrid bonded–riveted structures for EV battery enclosures. Recent studies have advanced digital techniques for fracture characterization of SMC and CFRP joints in EV applications, employing compliance-based methods, acoustic emission and optical measurement to map local toughness and crack growth resistance [83–88]. These approaches allow for early detection of cohesive failure, localized debonding and provide robust calibration for numerical models addressing industry needs for predictive performance in electrified platforms. This multi-scale approach offers a path to improve

repeatability, enhance digital twin models and develop predictive maintenance strategies for next-generation electric vehicles [89].

Modern joint design is increasingly informed by cohesive zone modeling (CZM) and advanced computational simulation [90]. Comprehensive reviews of fatigue delamination in composite and adhesive bonds have consolidated the understanding of the mechanisms leading to lifetime reduction, highlighting how micro-defects and environmental cycling amplify crack growth rates and require extended CZM-based predictive tools for accurate service life assessment [91–93]. Anyfantis and Tsouvalis [94] and Teixeira[95] have pioneered calibration strategies for traction-separation laws. Pirondi and Moroni [96,97] and Di Caprio [98] established experimental-numerical workflows for predicting crack initiation and growth, both under static and cyclic conditions. Comparing cohesive and classical linear elastic fracture mechanics, Chen CR and Mai [99] demonstrated the greater predictive power of CZMs for mode I crack growth across interfaces of varying stiffness, suggesting theoretical models should prioritize cohesive approaches in complex multi-material assemblies. Krueger [100] did a comprehensive review of the virtual crack closure technique (VCCT) detailing its mathematical foundations and its synergies with CZM for simulating crack extension in composite bonds. Nojavan, Schesser and Yang [101] modeled fatigue crack growth via 2D CZM; mixed-mode tests revealed real crack rates depend on plasticity and load sequence. Chen Q. [102] mixed-mode fatigue life tests showed correct modeling of energy release rates is central to accurate joint life prediction. Giuliese, Pirondi and Moroni [103] extended CZM modeling to multi-axial fatigue and delamination, stressing the impact of defects. Moazzami [104] designed degradable CZM for composite/metal joints with cyclic ageing exposure, showing the need for dynamic parameter calibration. Jaillon [105] implemented digital image correlation for CZM parameter uncertainty, leading to more robust modeling. Law [106] validated plasma treatment removal for composites, increasing joint static and fatigue reliability. Valoroso [107] showed that benchmark analytical and computational solutions enable the extraction of cohesive parameters from experimental DCB data, thus bridging experimental and pure-simulation domains. Pascoe [108] systematically reviewed modeling techniques for fatigue delamination in composites, emphasizing the theoretical basis and extensions of CZM and Paris law for lifetime prediction. Mackerle [109] compiled a thorough bibliography of simulation methods, summarizing advances in FEM and CZM approaches in adhesive joint modeling over two decades. Pardoen [110] analyzed constraint effects in adhesive joint fracture using both theoretical and simulation models,

underlining that local stress state and plastic zone size must be incorporated for realistic energy release rate assessment [111,112].

Sekiguchi, Hayashi and Sato [113] presented an analytical approach for determining deformation in DCB with an elastic–plastic layer, providing an accurate link between observed opening and material constitutive parameters for numerical modeling. Recent simulation work by Li and Li [114] mathematically linked the parameters of cohesive traction laws to the size of the fracture process zone, providing guidelines for model setup and interpretation of CAE simulations in composites applications. Krasucki [115], through detailed debonding simulations, highlighted how local interface strength and microstructural variability can be directly tied to macroscopic failure via CZM.

This research project is fundamentally driven by the following questions:

- To what extent does the coupling of geometric variability and service temperature alter the fracture process zone in SMC-bonded joints?
- Can a standardized plasma surface treatment protocol mitigate the detrimental effects of chemical releasing agents used in high-volume molding?
- Is it possible to automate the calibration of cohesive zone parameters to ensure high-fidelity predictions in full-vehicle crash scenarios? The main assumption is that the adhesive material card must be treated as a system-level property, influenced by the specific interaction between the polyurethane matrix and the SMC substrate.

International standards (ASTM, ISO and others) continue to provide the technical backbone for comparative fracture research. Their protocols, while referenced briefly here, are discussed in depth in Section 2.5.

The general objective of this thesis is to establish a comprehensive experimental-numerical framework for the characterization and simulation of automotive SMC joints. Specifically, the research aims to quantify the influence of thickness and temperature on Mode I and II fracture energies and to develop a semi-automated optimization workflow for CZM parameter identification. The methodology integrates high-resolution mechanical testing (DCB, ENF, SLJ) with a computational loop utilizing HyperStudy and Abaqus, allowing for a data-driven calibration of the constitutive laws.

. The present work is organized into the following chapters:

- **Chapter 1** provides introduction, motivations and research objectives.
- **Chapter 2** details theoretical framework of fracture mechanics and cohesive zone modeling.
- **Chapter 3** describes materials, manufacturing processes and experimental methods.
- **Chapter 4** investigates identification of geometric parameters for adhesion characterization.
- **Chapter 5** analyzes influence of adhesive thickness on joint performance.
- **Chapter 6** assesses impact of service temperature on fracture behavior.
- **Chapter 7** compares adhesive properties using Glass-SMC substrates.
- **Chapter 8** evaluates behavior of Aluminum-SMC bonded joints.
- **Chapter 9** focuses on mixed-mode fracture and fatigue degradation.
- **Chapter 10** complements dataset with characterization of bulk adhesive specimens.
- **Chapter 11** presents semi-automated procedure for Material Card generation and optimization.
- **Chapter 12** summarizes final conclusions and proposes future research directions.

Chapter 2: Theoretical framework on fracture mechanics of adhesively bonded joints

2.1 Introduction to Fracture Mechanics

Classical Linear Elastic Fracture Mechanics (LEFM) has been successful in predicting fractures in ideally brittle and homogeneous materials. The LEFM framework is built around the concept of stress singularity at the tip of an infinitesimally sharp crack. However, this assumption breaks down for materials like polymeric adhesives, which exhibit significant non-linear deformation and energy dissipation through mechanisms such as plasticity and micro-cracking. These events occur within a finite-sized region ahead of the macroscopic crack tip, a region known as the Fracture Process Zone (FPZ – See Figure 1). The LEFM framework, with its singular stress field, is incapable of capturing these crucial physical phenomena, making it unsuitable for accurately modeling the failure of most structural adhesive joints.

The fundamental distinction between LEFM and Non-Linear Elastic Fracture Mechanics (NLEFM) lies in the treatment of the plastic or damaged zone surrounding the crack tip. While LEFM assumes that all material behavior remains linear elastic until failure (confining any non-linear effects to an infinitesimally small point at the crack tip) NLEFM accounts for a finite-sized region of non-linear deformation and energy dissipation. In the context of structural adhesives, NLEFM is essential because the FPZ is often large compared to the bond line thickness, meaning the stress intensity factors or energy release rates derived from linear assumptions would lead to significant underestimations of the joint's actual strength.

The FPZ is not merely a mathematical abstraction but a physical region where energy-dissipating micro-mechanisms occur before and during crack propagation. In polymer adhesives, these mechanisms include (See Figure 2):

- **Void Nucleation and Growth:** Under the high hydrostatic stresses near the crack tip, microscopic voids can form, often around toughening particles, fillers or impurities within the adhesive.

- **Bridging:** As the main crack opens, adhesive lamellar chunks can sometimes detach themselves spanning between the crack faces, transferring load and resisting further separation until they eventually fail.

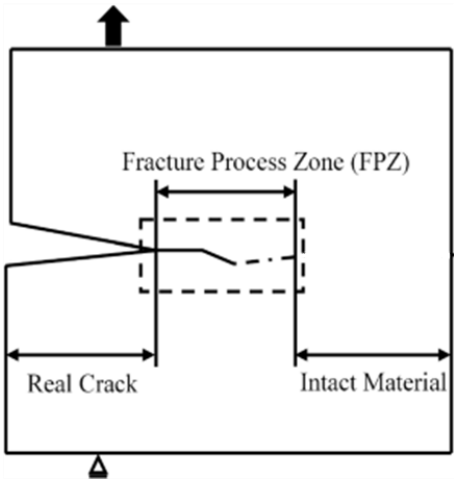

Figure 1: Representation of Fracture Process Zone

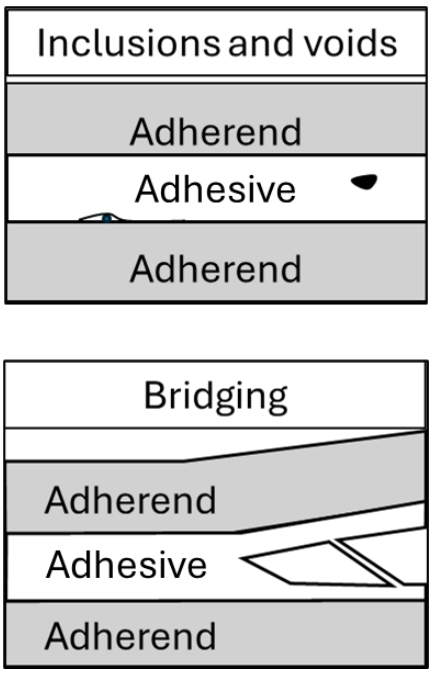

Figure 2: Typical defects and failure problems in adhesively bonded joints

2.2 Modeling with Cohesive Zone Model

Cohesive Zone Models (CZM) overcome the limitations of LEFM by conceptually collapsing all the complex energy dissipation events occurring within the FPZ onto a single plane or interface. For mixed-mode delamination and adhesive joint failure, recent work supports the implementation of advanced cohesive zone formulations that include branching, softening and stochastic approaches to more faithfully reproduce local crack initiation, deflection and interface instability typical of modern multi-material bonded systems [116,117]. Semi-analytical and numerical solutions for DCB specimens with non-linear interfaces have recently provided valuable reference benchmarks to validate mode I and mixed-mode traction-separation law parametrization, as well as new insights on brittle versus quasi-brittle delamination in composite joints [119–121].

It is worth noting that CZM is inherently a subset of NLEFM, as it effectively accounts for the non-linear energy dissipation occurring within the FPZ. By replacing the linear elastic singularity with a traction-separation law, the CZM framework incorporates material non-linearity and softening, providing a robust constitutive approach to simulate the complex failure stages that characterize structural adhesives beyond the limits of classical LEFM. By adopting a CZM, the simulation transitions into the NLEFM domain, as the traction-separation law explicitly models the non-linear degradation (softening) of the material, which LEFM is inherently unable to capture.

CZM replaces the stress singularity with a constitutive law that describes the gradual decohesion process. Instead of a sharp crack, the model introduces a "cohesive zone" where tractions/stresses are transmitted between the separating surfaces, allowing for the modeling of damage in a physically representative manner. This enables direct comparison between the predicted and observed failure mechanisms and supports the robust design of bonded SMC and CFRP assemblies. Comprehensive parametric optimization and benchmarking of CZM element models have been supported by systematic sensitivity analyses and multi-algorithm optimization studies, enabling tailored design and acceleration of simulation-based joint development in automotive and aerospace fields [118].

2.3 The Traction-Separation Law

The base of any Cohesive Zone Model is the Traction-Separation Law (TSL). TSL is a constitutive material related law that defines the relationship between the cohesive traction (***t***) acting across an interface and the corresponding separation (**δ**) between the surfaces. This law mathematically describes the entire failure process, from initial elastic loading, through damage initiation and material softening to complete separation. The shape of the TSL can be tailored to represent the behavior of different materials (See Figure 3):

- **Bilinear TSL:** This is the most widely used shape due to its simplicity and ability to capture the fundamental features of fracture with a small number of parameters. It consists of a linear elastic loading phase followed by a linear softening phase.

- **Trapezoidal (or Trilinear) TSL:** This shape is particularly well-suited for adhesives that exhibit a distinct plastic yielding plateau before the onset of material softening and final failure.

- **Polynomial and Exponential TSL:** This law provides smooth and continuous softening behavior, which can be more physically realistic for certain polymers and can offer numerical advantages by avoiding abrupt changes in stiffness.

Alfano and Crisfield [76] demonstrated that bilinear traction–separation laws provide numerical stability and improved convergence for delamination and adhesive fracture modeling.

Whatever of its specific shape, a TSL is fundamentally defined by three key parameters:

- **Initial Stiffness (*K*):** This parameter defines the slope of the initial, undamaged elastic portion of the TSL. In this linear elastic segment of the traction-separation law, the following relations are applied:

$$\boldsymbol{t} = \begin{matrix} t_n \\ t_s \\ t_t \end{matrix} = \begin{bmatrix} K_{nn} & K_{ns} & K_{nt} \\ K_{sn} & K_{ss} & K_{st} \\ K_{tn} & K_{ts} & K_{tt} \end{bmatrix} * \begin{matrix} \delta_n \\ \delta_s \\ \delta_t \end{matrix} = \boldsymbol{K} * \boldsymbol{\delta} \qquad \text{Eq. (1)}$$

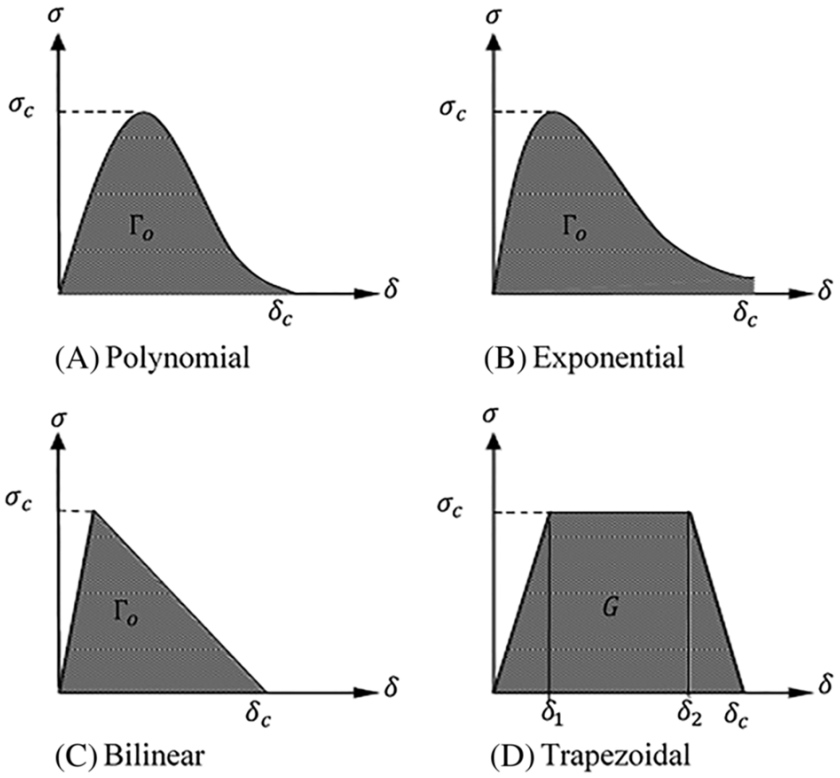

Figure 3: Typical shapes of common employed traction-separation laws: a) polynomial, b) exponential, c) bilinear and d) trapezoidal

where ***K*** is called penalty stiffness matrix and contains the various components of the stiffness, generally a symmetric matrix. Under the hypothesis that the normal and shear components of cohesive stress are uncoupled, the cross terms vanish, i.e. K_{ns}= K_{nt}= K_{st}= 0 and ***K*** becomes a diagonal matrix.

- **Cohesive Strength (t_{max}):** This represents the maximum traction that the interface can withstand. Reaching this stress value of damage initiation, after which the material begins to soften and lose its load-carrying capacity.

- **Fracture Energy (G_c):** This is the total energy dissipated per unit of fracture surface area and is represented by the total area under the TSL curve. It is a fundamental material property that quantifies the material's resistance to crack propagation and governs the damage evolution process.

Experimental comparison of cohesive traction-separation relationships using commercial FE software platforms has clarified the strengths and limitations of different constitutive approaches, promoting convergence towards robust, physically motivated traction laws for the simulation of adhesive joint failure in industry [122,123]. Recent work on butt-joint and lap-joint configurations demonstrates that variation in adhesive modulus and layer design facilitate increased crack resistance; elastic modulus optimization strategies provide a pathway to robust adhesion even with thermoplastics, thermosets and challenging laminate pairings [124].

2.4 Failure Criteria

In most structural applications, adhesive joints are subjected to complex loading states that result in a combination of fracture modes. The three fundamental modes are Mode I (opening/tensile), Mode II (in-plane shear) and Mode III (out-of-plane shear), visually represented in Figure 4.

To model failure under these Mixed-Mode conditions, the TSL framework must be extended. This is typically achieved by defining separate TSLs for the normal (Mode I) and shear (Mode II/III) directions and then coupling them through specific criteria for damage initiation and evolution (See Figure 5).

In this case only the Mode I and Mode II directions were investigated because, usually from state-of-art, Mode III is assumed to be equal or comparable to Mode II or however is dependent on the CAD model material orientation system and specific loading condition.

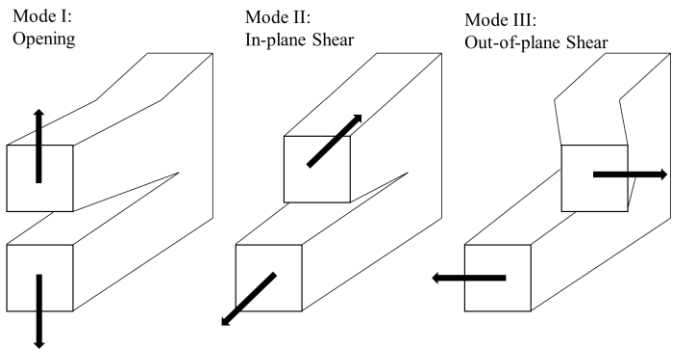

Figure 4: Main damage directions: Mode I for opening, Mode II and Mode III for shear failure

2.4.1 Damage Initiation Criteria:

In the context of material mechanics, damage initiation refers to the onset of degradation in a material's mechanical response, characterized by a loss of stiffness and load-bearing capacity. The degradation process begins when the stresses and/or strains within the material satisfy a specific initiation criterion. Computationally, each criterion is associated with an output variable and damage is considered to have initiated once the value of this variable reaches or exceeds unity.

Within the framework of cohesive zone modeling, as implemented in Finite Element software like Abaqus software, these initiation thresholds are defined by the peak values of the traction-separation law. The terms t_n^0 , t_s^0 and t_t^0 represent the maximum allowable stress (cohesive strength) in the normal direction and the two orthogonal shear directions, respectively. Similarly, ε_n^0, ε_s^0 and ε_t^0 represent the corresponding peak separations (or strains) at which these maximum stresses are reached. These values serve as the fundamental limits that must be exceeded for damage to begin. For a general triaxial stress or strain state, several criteria exist to combine these uniaxial thresholds to predict the onset of damage as presented as follows:

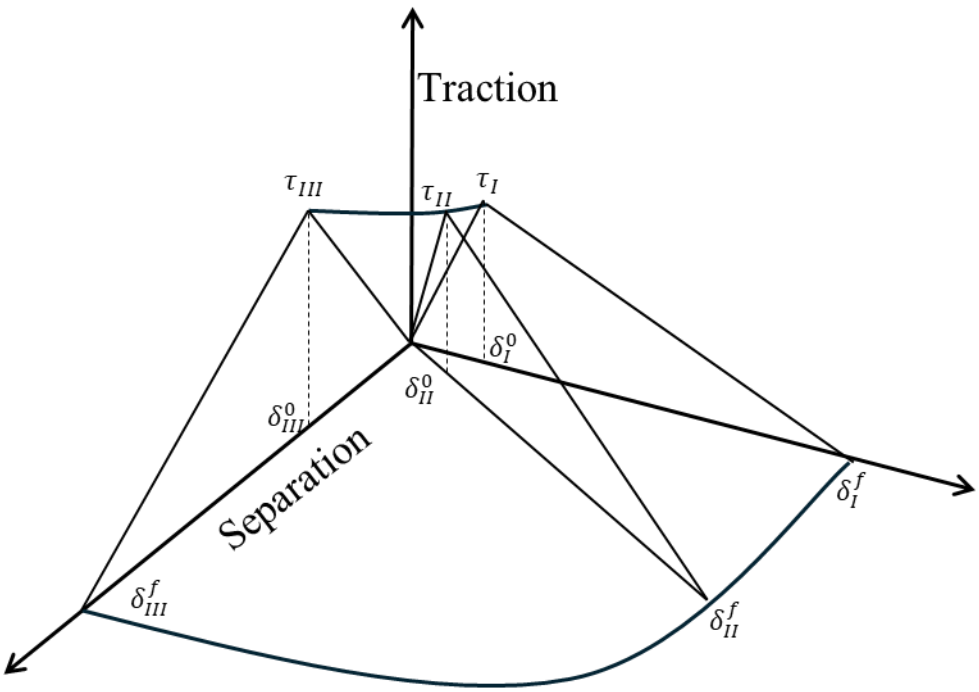

Figure 5: Traction separation law displayed in the three main damage direction describing the complex mixed modes under certain loading conditions.

MAXE - Maximum Nominal Strain $1=\boldsymbol{max}\{\frac{\langle\varepsilon_n\rangle}{\varepsilon_n^0}, \frac{\langle\varepsilon_s\rangle}{\varepsilon_s^0}, \frac{\langle\varepsilon_t\rangle}{\varepsilon_t^0}\}$ Eq. (2)

MAXS - Maximum Nominal Stress $1=\boldsymbol{max}\{\frac{\langle t_n\rangle}{t_n^0}, \frac{\langle t_s\rangle}{t_s^0}, \frac{\langle t_t\rangle}{t_t^0}\}$ Eq. (3)

MAXPE - Maximum Principal Strain $1=\{\frac{\langle\varepsilon_{max}\rangle}{\varepsilon_{max}^0}\}$ Eq. (4)

MAXPS - Maximum Principal Stress $1=\{\frac{\langle\sigma_{max}\rangle}{\sigma_{max}^0}\}$ Eq. (5)

QUADE - Quadratic Nominal Strain $1=\{\frac{\langle\varepsilon_n\rangle}{\varepsilon_n^0}\}^2+\{\frac{\langle\varepsilon_s\rangle}{\varepsilon_s^0}\}^2+\{\frac{\langle\varepsilon_t\rangle}{\varepsilon_t^0}\}^2$ Eq. (6)

QUADS - Quadratic Nominal Stress $1=\{\frac{\langle t_n\rangle}{t_n^0}\}^2+\{\frac{\langle t_s\rangle}{t_s^0}\}^2+\{\frac{\langle t_t\rangle}{t_t^0}\}^2$ Eq. (7)

The selection of a damage initiation criterion depends on the specific failure physics of the adhesive and the degree of interaction between different loading modes. Criteria such as MAXS and MAXE are based on a non-interactive logic, where damage is triggered as soon as the peak threshold is reached in any single direction (normal or shear), regardless of the state of stress in the others. In contrast, QUADS and QUADE are interactive criteria; they assume that damage can initiate even if no individual stress component has reached its respective cohesive strength, provided that their quadratic combination reaches unity. This second approach is generally more representative of structural adhesives, as it accounts for the coupled effect of tension and shear which often accelerates degradation.

For this study, the QUADS - quadratic nominal stress criterion (Eq. (7)**)** was selected, which starts the damage initiation process when a quadratic combination of the stress ratios (traction divided by cohesive strength in each mode) reaches unity. The selection of this criterion is justified by the complex multi-axial stress states typically encountered in structural bonded joints, particularly when employing anisotropic substrates like carbon fiber SMC. Unlike non-interactive criteria (MAXS), the quadratic formulation accounts for the interaction between normal and shear stresses. This is particularly critical where the coupling of Mode I and Mode II loading often leads to a reduction in the effective initiation threshold compared to pure-mode conditions. Therefore, the QUADS criterion provides a more comprehensive and conservative prediction of damage onset, accurately capturing the physical behavior of the adhesive interface under realistic mixed-mode loading conditions

2.4.2 Damage Evolution Laws:

Once the damage initiation criterion has been met, the material does not fail instantaneously. Instead, it enters a phase of progressive degradation known as damage evolution. This phase is governed by the material's fracture energy, which represents the energy dissipated per unit area during the failure process and it describes the process of material softening, where the stiffness gradually decreases and the load-carrying capacity is reduced until complete failure (i.e. total separation of the surfaces) occurs. State-of-the-art experimental campaigns now deploy wedge-loaded DCB, sandwich, hinge and butt-joint geometries to validate mode I and II traction-separation laws for both stiff and flexible adhesive formulations, thus informing multi-scale model setups [125–127].

Experimental investigations into cyclic fatigue crack growth in automotive adhesives, under both static and dynamic loading, reveal that accurate prediction of service life requires cyclic cohesive zone models and fatigue modeling environments able to capture both crack closure and load-ratio effects [128,129].

The state of damage is typically characterized by a single scalar damage variable**,** D. This variable evolves monotonically from 0 (undamaged material) at the point of damage initiation, to 1 (failed material) at the point of complete separation. Advanced CZM simulations have been used to replicate not only the softening process under monotonic loading, but also progressive fatigue degradation under high-cycle and mixed-mode conditions, validating the applicability of these frameworks for lifetime prediction in bonded joints [130,131].

The primary effect of the damage variable is the degradation of the material's stiffness. The cohesive tractions (t) acting across the interface are reduced as a function of D according to the fundamental relationship:

$$t = (1 - D) \cdot t0 \qquad \text{Eq. (8)}$$

where $t0$ represents the "undamaged" traction components that would be predicted by the initial elastic behavior at the current separation.

The evolution of the damage variable D is defined as a function of the effective separation, δ_m, relative to its value at damage initiation, δ_0 and at final failure, δ_f. The specific mathematical form of this function determines the shape of the softening portion of the Traction-Separation Law (TSL).

- **Linear Softening:** This is the simplest evolution law, resulting in a bilinear TSL. The damage variable increases linearly with the displacement. This law is computationally efficient and is often sufficient for modeling materials with a relatively brittle post-peak behavior:

$$D = \frac{\delta_f * (\delta_m - \delta_0)}{\delta_m * (\delta_f - \delta_0)} \qquad \text{Eq. (9)}$$

- **Exponential Softening:** For many polymers and ductile adhesives, an exponential law provides a more physically realistic representation of the softening behavior, with a more gradual initial degradation. Here, **α** is a non-dimensional parameter that controls the curvature of the softening response:

$$D = 1 - \left(\frac{\delta_0}{\delta_m}\right) * [1 - \frac{1 - \exp\left(-\alpha \left(\frac{\delta_m - \delta_0}{\delta_f - \delta_0}\right)\right)}{1 - \exp\left(-\alpha\right)}] \qquad \text{Eq. (10)}$$

The displacement at final failure δ_f is not an independent parameter but is calculated from the material's fundamental fracture energy G_c. For mixed-mode loading, the total fracture energy itself is not constant but depends on the relative proportions of Mode I and Mode II loading. To describe this dependency, mixed-mode fracture criteria are used:

- **Power Law Criterion:** This is a common and robust criterion that relates the total mixed-mode fracture energy, G_c, to the pure-mode fracture energy:

$$\left(\frac{G_I}{G_{Ic}}\right)^{\alpha} + \left(\frac{G_{II}}{G_{IIc}}\right)^{\alpha} + \left(\frac{G_{III}}{G_{IIIc}}\right)^{\alpha} = 1 \qquad \text{Eq. (11)}$$

- **Benzeggagh-Kenane (BK) Criterion:** This is another widely used power-law formulation, particularly effective for composite delamination and adhesive bonding. It interpolates between the pure-mode fracture energies based on the mode mixity ratio:

$$G_{\mathrm{C}} = G_{\mathrm{IC}} + (G_{\mathrm{IIC}} - G_{\mathrm{IC}})\left(\frac{G_{\mathrm{II}} + G_{\mathrm{III}}}{G_{\mathrm{I}} + G_{\mathrm{II}} + G_{\mathrm{III}}}\right)^{\eta} \qquad \text{Eq. (12)}$$

Being G_C, G_{IC} and G_{IIC} respectively the total, normal and shear critical energies release rates and G_I, G_{II} and G_{III} the energy release rate under Mode I, Mode II and Mode III respectively. η is the relevant material parameter in the BK law, as well as peak stresses and the critical energy release rates.

The combination of a damage initiation criterion with a damage evolution law, governed by the appropriate mixed-mode fracture criterion, provides a complete and powerful framework for the predictive simulation of failure in adhesive joints. The impact of test geometry on the measured mode I fracture resistance has been systematically analyzed, showing that variations in specimen width and rigidity, like sandwich specimens, can influence the apparent energy release rate and must be accounted for when extracting cohesive parameters [132–134]. Da Silva [78] experimentally quantified the interaction between Mode I and Mode II fracture energies in bonded joints, confirming the validity of polynomial interaction criteria. Turon [77] and Campilho [81] proposed mixed-mode CZMs combining cohesive traction and damage variables, achieving accurate correlation with DCB and ENF test results. Benchmark studies comparing simulation software, analytical models and closed-form solutions confirm that hybrid numerical-experimental workflows provide the most robust path for parameter calibration, uncertainty reduction and predictive modeling in structural adhesive joints [135,136].

2.5 Experimental framework to determine mechanical properties from standard tests

2.5.1 Double Cantilever Beam (DCB) test by ASTM D5528

DCB test was employed to derive the adhesive's fracture energy, G_I (J/m^2) under Mode I direction using the simplest mathematical form given by the standard, such as Modified Beam Theory (MBT) Method; the critical fracture toughness, G_{Ic}, can be then calculated as follows [137]:

$$G_{Ic} = \frac{3\,F_c\,\delta_c}{2\,b\,a} \cdot 1000 \qquad \text{Eq. (13)}$$

where b is the width of the specimen, a is the crack length, F_c is force at failure and relative displacement δ_c. Same consideration was made to analyze fracture energy of mixed-mode and fatigue DCB specimens during testing. DCB specimens being compliant with the ASTM D6671 standard for mixed-mode testing methodology and data analysis [138].

2.5.2 End Notched Flexure (ENF) Tests by ASTM D7905

ENF test was employed to derive the adhesive's critical fracture energy, G_{IIc} (J/m^2) under Mode II direction that can be calculated as follows [139]:

$$G_{\mathrm{IIc}} = \frac{3\,m\,F_{\max}^2\,a_{\mathrm{c}}^2}{2\,b} \cdot 1000 \qquad \text{Eq. (14)}$$

where $F_{\max}$ is the maximum force recorded on the force-displacement curve, m (1/Nmm^2) the slope of the linear fit of compliance versus crack length cubed data and b is the specimen width. The crack length a_{c} (mm) was computed through the formula:

$$a_{\mathrm{c}} = \left(\frac{C_{\mathrm{u}} - A}{m}\right)^{1/3} \qquad \text{Eq. (15)}$$

where C_{u} (mm/N) is the specimen compliance after unloading and A (mm/N) is the intercept of the linear fit of compliance versus crack length cubed data.

2.5.3 Single Lap Joint (SLJ) Tests by ASTM D3165

SLJ test were evaluated for shear stress strength, based on ASTM standards so considering the maximum load at break and the relative shear stress calculated as follows and based on the selected adhesive bonded area *A* [140]:

$$\tau_{max} = \frac{F_{max}}{A} \qquad \text{Eq. (16)}$$

2.5.4 Dogbone Tensile Tests by ASTM D638

Dogbone test was employed for to assess the adhesive's elastic response under tensile load. The key parameters were the section area, force and relative displacement at failure used to calculate tensile stress as follows [141]:

$$\sigma_{max} = \frac{F_{max}}{A} \qquad \text{Eq. (17)}$$

The modulus of elasticity is determined as the slope of the stress-strain curve by extending the initial linear portion of the load-displacement curve and dividing the difference in stress corresponding to any segment of section on this straight line by the corresponding difference in strain. To ensure consistency, this calculation is performed over a precisely defined strain interval, typically between 0.05% and 0.25% strain, however, because of the non-linear behavior of the adhesive and so having more consistent data, a bigger interval between 0.5% and 1% was selected. The most robust method stipulated by the standard for determining this slope is a linear regression analysis of all data points within this range. After linear regression, the elastic modulus can be calculated as follows:

$$E = \frac{L_0 * (F_{i+1} - F_i)}{A * (L_{i+1} - L_i)} \qquad \text{Eq. (18)}$$

Poisson' ratio is also an important parameter, calculated as follow with measurements derived by a VideoXtens optical extensometer *dεt* is the change in transverse strain and *dεa* is the change in axial strain:

$$\mu = \frac{d\varepsilon t}{d\varepsilon a} \qquad \text{Eq. (19)}$$

2.5.5 Thick Adherend Lap Shear (TLS) Tests by ASTM D5656

TLS test was used to assess the adhesive's elastic response under shear load. The key parameters were the section area, force and relative displacement at failure and the shear modulus of elasticity determined as for the dogbone specimen above, so from the interval between 0.5% and 1% of the regression linear trait of the stress-strain curve, as follows [142]:

$$G_Q = \frac{L_0 * (F_{i+1} - F_i)}{A * (L_{i+1} - L_i)} \quad \text{Eq. (20)}$$

2.5.6 Rod Joint Tensile Tests by ASTM D2095

Rod joint specimen was employed to assess the adhesive's strength under tensile stress. The key parameters were the section area, force and relative displacement at failure, as follows [143]:

$$\sigma_{max} = \frac{F_{max}}{A} \quad \text{Eq. (21)}$$

2.5.7 Compact Tension (CT) Tensile Tests by ASTM D5045

CT test was used to assess the adhesive strength under tensile stress. The test was used to assess the adhesive's plane-strain fracture toughness, K_{Ic} and the strain energy release rate, G_{Ic}. Because of uncertainty in adhesive behavior, some simple mathematical assumptions were made to finally derive the plane-strain fracture toughness, K_{Ic} and the strain energy release rate, G_{Ic}, as follows [144]:

$$K_{Ic} = \frac{F_Q}{B * \sqrt{W}} \quad \text{Eq. (22)}$$

$$G_{Ic} = \frac{U}{B * W} \quad \text{Eq. (23)}$$

where: B is the specimen thickness, W is a characteristic length of the specimen (See Figure 17), F_Q is a force threshold derived from ASTM standards calculation, by definition lower than F_{max} at failure and U is an energy derived from the area under the force-displacement curve, calculated through an algorithm from the TestXpert © software from ZwickRoell.

Chapter 3: Materials and methods

3.1 Introduction

This study examines the mechanical behavior and bonding properties of adhesives and composite joints focusing on the combination of Carbon SMC bonded with polyurethane adhesive supported by atmospheric plasma surface treatment. The materials were chosen for their complementary mechanical and processability characteristics for a real-case industrial application: carbon SMC composite components have a high-volume manufacturing process while polyurethane adhesives are suitable for automated robot-driven deposition processes, both empowering fast and controlled assembly processes in big production lines.

This section provides an overview of the manufacturing and preparation methodologies employed for all specimens during the extensive experimental campaign. The fundamental manufacturing procedure for bonded specimens and bulk adhesive specimens remained consistent and it's detailed in the following chapters. The final dimensions of all the bonded specimens were tailored to be compliant with the specific requirements of each mechanical test standard (See Section 2.5).

3.2 Specimen materials

For this study a commercial Carbon-based SMC STR120N131 (Mitsubishi Chemical©) was employed for all relevant adhesive joint specimens (See Table 1).

As previously anticipated, SMC is a fast-curing thermosetting composite material made with a vinyl ester resin and reinforced with a 53% weight fraction of TR50S-15L Pyrofil® chopped strands randomly distributed within the sheet. Whereas tow width, thickness and length are subject to variation due to the manufacturing process, average values are 8 mm, 0.115 mm and 25 mm, respectively. The material is typically formed through a compression molding process, where sheets of SMC are placed into a heated mold cavity (usually around 180 °C) and compressed under high pressure (around 5-15 ton). This process allows for the rapid production of complex, intricate geometries with integrated features, such as ribs and mounting points and can achieve a surface finish suitable for exterior body panels. The random orientation of the fibers generally means quasi-isotropic mechanical properties in the plane of the sheet, providing a balance of strength and stiffness in multiple directions.

In addition to standard SMC, variants such as Glass SMC (utilizing glass fibers instead of carbon) which may feature different resin systems, will also be considered for comparative analysis under specific test configurations.

For aluminum members, the alloy is certainly of the Ergal type but for reasons of company confidentiality the exact name of the alloy is not due to know.

The specific adhesive under investigation is a commercial Parker LORD 7545 A/D (Parker Lord Engineered Materials Group, Cary, USA – See Table 2) that is a two-component urethane structural adhesive system designed for bonding fiber-reinforced plastics. The adhesive achieves optimal performance and an excellent resistance to mechanical stress after a 7-day curing period at ambient temperature. Alternatively, it can undergo an accelerated curing process, reaching similar properties in a few hours when exposed to elevated temperatures up to 80°C. This flexibility in curing provides versatility for both experimental setups and manufacturing procedures.

Table 1: Material properties of Carbon-SMC adherends: str120n131 from Mitsubishi chemicals

Property	**Value**
Resin	VE
Tow size	15K
Carbon Fiber length	25.4 mm
Carbon Fiber content	53%
Areal Weigth	3100 g/m^2
Density	1.46 g/cm^3
Tensile Strength	171 MPa
Modulus of Elasticity (Tensile) Flexural Stregnth Modulus of Elasticity (Flexural) Tg (Glass Transition Temperature – Tan(δ) max)	29 GPa 376 MPa 27 GPa 158°C

Table 2: Mechanical commercial properties of Parker LORD 7545 A/D adhesive

Typical Properties	**Value**
Appearance	Off White or Black Paste
Viscosity, cP (25°C)	230.000-650.000
Density (kg/m^3)	1270-1318
Flash Point (°C)	>200
Mix Ratio, Resin to Curative by Volume (by Weight)	1:1 (1:0-85)
Solids Content, % by Weight	100
Working Time, min (24°C)	11-18
Purge Time, min (24°C)	15
Time to Handling Strength (24°C)	90 min

3.3 Specimen manufacturing

3.3.1 Adherends manufacturing

The SMC raw material was extracted from cold storage and cut into preforms of 300 x 300 mm. Preforms were stacked to obtain the desired charge thickness, which were press-molded into 500 × 500 mm cavity to obtain the final SMC plate, obtained under controlled machinery settings to ensure consistent design thickness of 4.1 mm and contain possible material defects (See Figure 6). First batch of specimens for sandblasted tests were designed to have 4.8 mm.

The molding process was conducted using a Cannon hydraulic press (15 ton). A chemical releasing agent was sprayed on the molds surfaces to facilitate demolding after curing, then the molding process followed confidential pressure-temperature-time controls settings to ensure best manufacturing conditions.

While it is recognized that the application of chemical releasing agents to both mold surfaces may compromise subsequent adhesive bonding by reducing surface energy and inhibiting proper wetting, several factors in this study ensure the reliability of the results. Firstly, the agent was applied with a spray technique to ensure the bare minimum quantity required for demolding, thus preventing excessive transfer to the composite skin. Secondly, the molding protocol did not involve re-application for every cycle, but only once every ten or more plates; this approach, combined with the selective extraction of specimens from the central plates of each batch and a high sample population, ensures that any potential influence of the release agent is statistically diluted and remains negligible.

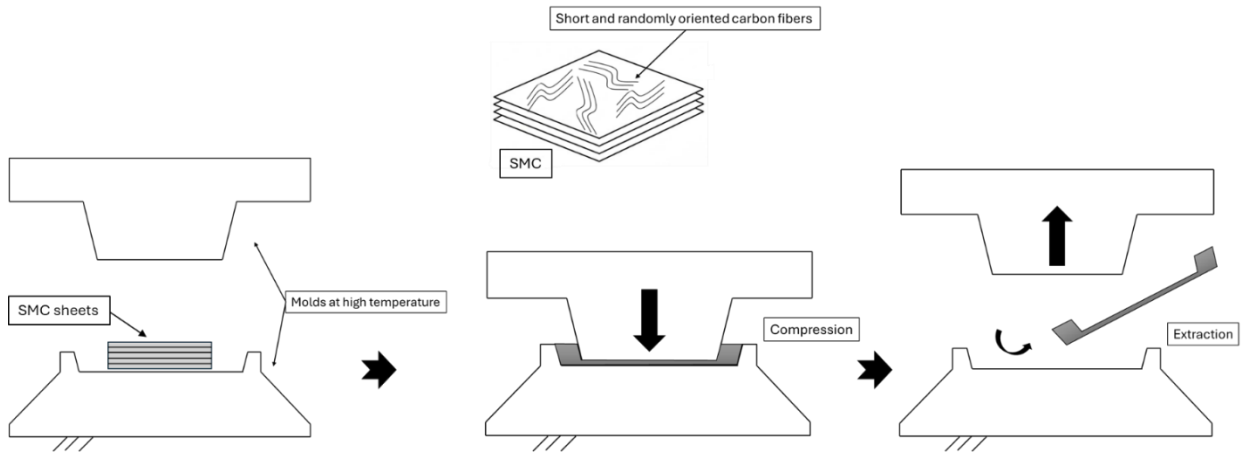

Figure 6: Schematic representation of SMC components manufacturing process and material architecture

The resultant plates were then cut into specimens' shapes (small thin plates) using automated water-jet technology, ensuring clean and accurate edges and reducing at minimum thermal or mechanical damages. From these plates, individual adherends for DCB, ENF, Mixed Mode, Fatigue and SLJ were manually extracted. Each adherend was subsequently cleaned from excess materials using sandpaper and ultimately measured with calipers to confirm conformity to the designated dimensions and geometrical tolerances. Following measurement, a systematic cleaning protocol was employed where each specimen was cleaned with isopropyl alcohol and white cloths to remove residual contaminants; such attention is due to the surface treatment sensibility. The specimens were then preserved in a controlled environment to prevent dust accumulation prior to bonding preparation.

Some defects were observed in the plates manufacturing, probably linked to the parameters with which they are manufactured in mold pressing and/or during the cutting process: for example, some adherends were discarded due to excessively accentuated curvature which could lead to non-uniform glue gaps or in any case to a non-compliant specimen.

Additionally, adhesively bonded hybrid SMC-Aluminum were tested. Aluminum samples were extracted from a 6 mm and a 3 mm (respectively for DCB and SLJ specimens) from a bigger plate by CNC cutting.

3.3.2 Surface Treatments

To prepare the adherends for bonding, plasma treatment on the adhesion surfaces was selected as main process of interest. For industrial purposes was applied with an automated industrial robot-arm. Also, sandblasted specimens were prepared with a sandblasting machine: preparation followed masking the non-treated surfaces with tape, by putting the samples in an isolated chamber and applying a flow of material with a pressure of approximately 4 bar and with a flow angle respect to the plane surface of the specimens of 45°. Additionally, both cleaned specimens and hinges/blocks were masked with releasing tape and positioned in an isolated chamber to perform sandblasting process to the bonding surfaces to enhance surface energy and adhesion. Note that the general bonding process must be completed within at least 1 hour from the surface treatment to prevent surface re-contamination.

Aluminum adherends were not sandblasted or plasma treated as SMC samples, but rather they followed a strict chemical process to obtain an E-coating surface protection on the bare aluminum material; samples were then cleaned with isopropyl alcohol and white clothes.

3.3.3 Bonding procedure

In the bonding process, the adhesive deposition was performed manually. The Parker LORD 7545 A/D adhesive was applied using a compressed air-gun. Custom-designed gluing jigs were utilized to position the adherends accurately and maintain consistent alignment and pressure during curing. Prior to bonding, the jigs were prepared by coating them with a primer followed by chemical releasing agent, which was properly distributed to ensure ease of demolding after curing and for protection of the jigs.

Once the jigs were prepared and the specimens positioned, the correct spacer to obtain the designed adhesive gap was selected cleaned and positioned (necessary to obtain the designed initial crack length). Adhesive application was performed and the jigs were closed. The curing process was carried out at room temperature, with a relative humidity not exceeding 70% to ensure optimal adhesive performance. Specimens were left undisturbed in the jigs for the entire curing duration (7days) to achieve a robust and consistent bond. Figure 7 shows the procedure described to manufacture adhesively bonded joints, specifically with plasma surface treatment (certain details are obscured for confidentiality purposes under a Non-Disclosure Agreement).

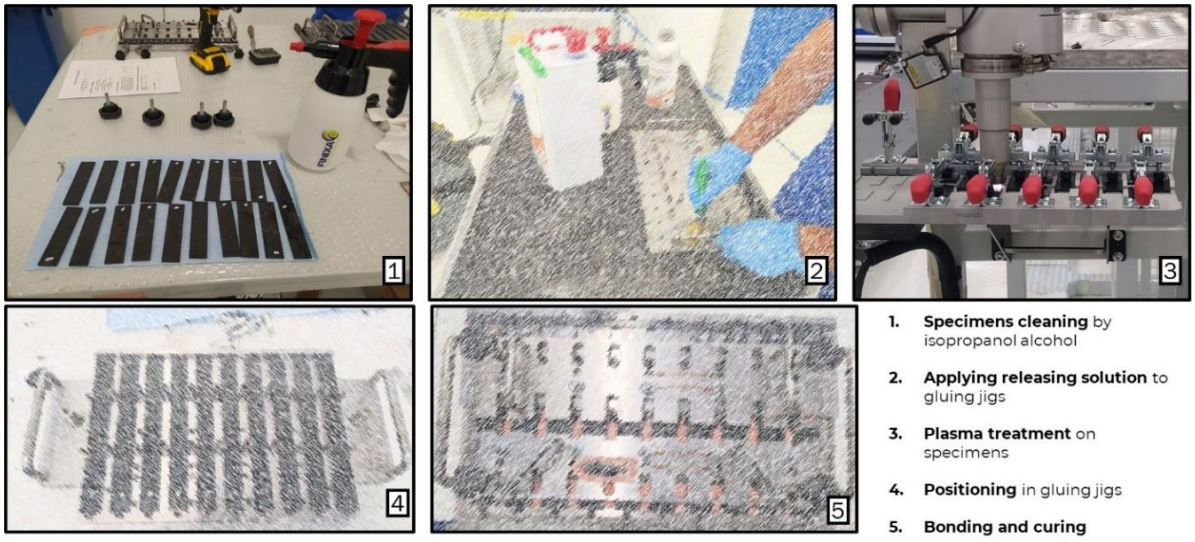

Figure 7: Procedure for bonding of adhesively bonded SMC joints

3.3.4 Specimens' pre-test preparation: Hinges, blocks, speckles and others

After the curing cycle, specimens were extracted from the jigs and cleaned by cutter, removing the excess adhesive derived from the squeezing process and so allowing a correct view of the side of the specimen and consequently the crack propagation during the mechanical testing phase.

For the DCB, Mixed Mode and Fatigue specimens, a dedicated secondary procedure was performed to bond hinges for DCB and Mixed Mode while using blocks for Fatigue tests only; both systems are necessary during the tests for gripping. The already glued and cleaned specimens and the hinges / blocks were masked with protective tape; the bonding surfaces and the SMC's tip-surfaces were therefore sandblasted as a surface treatment and positioned in a second custom-jig built specifically for hinges' bonding, also for blocks a custom-jig was designed and produced by 3D printing, within the Research Groups Labs of the Istituto Tecnico Superior.

The employed hinges were of two different kind where the first used were glued with Henkel Loctite EA 9466 and then secured with screws to the kinematic chain of the machine fixture, the second type of hinges for the subsequent tests were glued with 3M DP490 epoxy adhesive and secured to the fixture with a common manual pressure gripping, while blocks for fatigue testing were glued with Araldite Epoxy Extra Strong Adhesive, then jointed with a second block with screws and secured to the fixture inserting a pin.

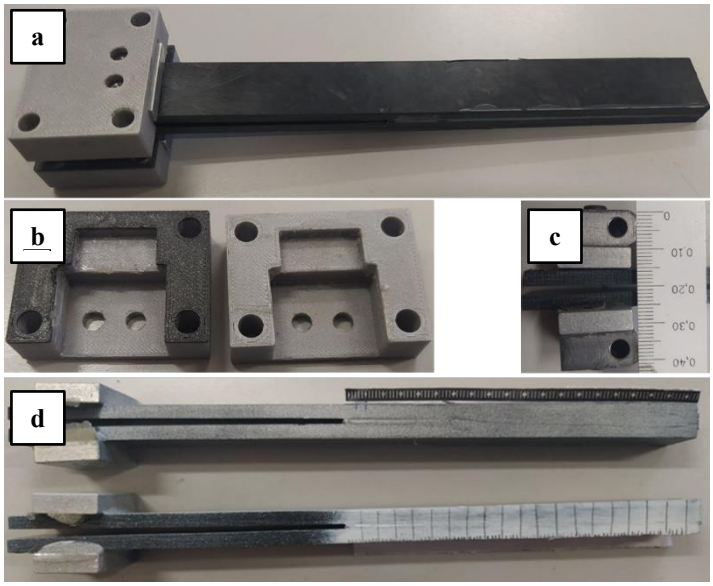

Figure 8: DCB fatigue testing specimens: a) curing phase of blocks, b) 3D printed jigs for blocks, c) measurements of the blocks system and d) DIC pattern (up) and marks on white paint (down) of the two sides of the specimens for crack advancement measurements.

For all hinges and blocks, the adhesive was applied with a manual mechanical gun and thickness was controlled by inserting copper wires with a diameter of 0.5 mm into the glue gap. These adhesives are both cured at room temperature for 7 days prior to testing to ensure maximum strength. During the bonding process, the pressure was assured by means of industrial plastic clamps adequately protected from adhesive excess and maintained in clamping position until complete cure of the adhesive.

White paint was also homogeneously applied on just one side of both DCB and Mixed Mode specimens, then a paper ruler was glued on the same side.

Additionally, for Fatigue specimens' speckles were applied to the other side of the specimen to obtain a recognizable pattern for DIC correlation by applying homogeneously white paint followed by black paint fine drops (See Figure 8).

Both strategies were taken to be able to observe and measure the crack propagation between the adhesive layer by means of a camera.

Some procedure differences were also employed to further develop the experimental methodology:

- For DCB plasma treated specimens, a different type of hinge was employed that required a clamping fixture instead of a screwed one. Also, a sharp razor blade was employed to cut open a small crack on the adhesive layer and facilitate crack initiation between the adhesive layer.

- For SLJ specimens, Carbon SMC tabs (small plates) were bonded with the same adhesive; the meaning of that is to enhance the stiffness of the sample thus reducing the bending moment on the joint.

- For ENF specimens, the flexural failure of the adherend was first connected to the excess stiffness of the sample and the friction between the specimens' not-bonded arms. To solve this, some frictionless shims (a greased releasing rolled paper, a solid plastic sheet) were employed to facilitate relative movement between arms and using a sharp razor blade to cut open a small crack on the adhesive layer.

3.3.5 Bulk specimen manufacturing

For CT, Rod Joint, Dogbone and TLS specimens' custom molds and jigs were designed and manufactured for each specimen type (See Figure 9 and Figure 10). Parker LORD 7545 A/D polyurethane adhesive was selected as base material for bulk adhesive characterization tests.

For CT and Dogbone specimens the adhesive was injected into custom molds by compressed air-gun and previously cleaned from impurities. For Rod Joint and Thick Shear specimens' custom-jigs and, respectively, cylindric steel adherends and aluminum block adherends were manufactured where the lap shear adherends were designed to be sufficiently stiff to minimize bending and ensure that the failure occurred predominantly in shear within the adhesive layer.

Aluminum blocks and steel adherends bonding area surfaces were treated by manual abrasion with sandpaper to facilitate adhesion and bonded with a custom designed gluing-jig. Adherends were then cleaned with isopropyl alcohol, positioned and aligned on the gluing jig, then the adhesive was applied with a mechanical gun.

All bulk specimens were left to cure at room temperature for 7 days with a relative humidity under 60%; after curing, specimens' edges were cleaned with a cutter to remove excess adhesive material. Also, Dogbone and CT specimens were painted only on one face with white paint to observe the failure mechanism.

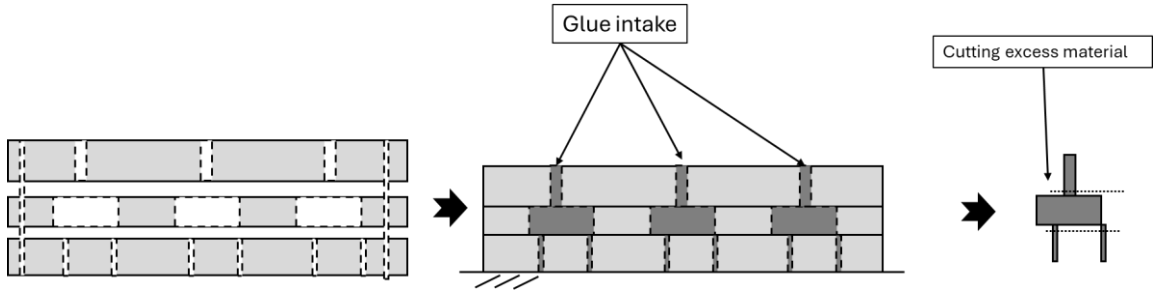

Figure 9: Schematic representation of bulk specimen manufacturing process.

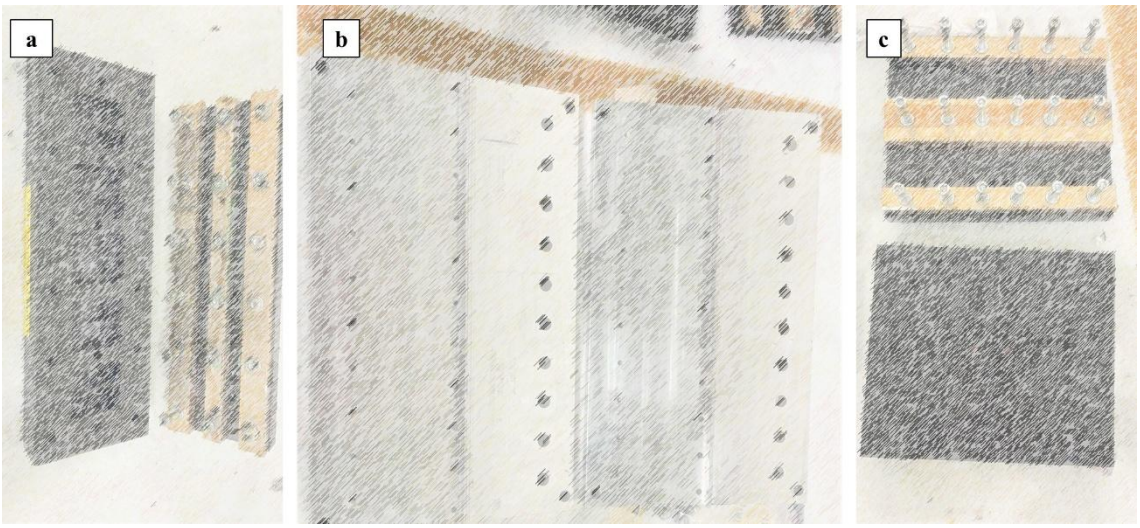

Figure 10: Pictures of some of the custom designed gluing jig to manufacture bulk adhesive specimens where: Mask a) was employed to obtain CT specimens, mask b) was employed to bond TLS and mask c) was used to produce dogbone specimens (certain details are obscured for confidentiality purposes under a Non-Disclosure Agreement).

3.4 Geometric parameters of the specimens: size and definition

3.4.1 Tensile loaded bonded specimen for Mode I fracture energy (DCB)

DCB test was selected to investigate the Mode I fracture energy of adhesively bonded joints in quasi-static tensile and mixed mode and fatigue cycling (See Section 2.5.1 and Table 3). Specimens were made of small SMC plates where main dimensions can be seen on Figure 11. For sandblasted specimens the dimensions were of length L = 155 mm, hinge length e = 25 mm, pre-crack length a0 = 35/ 45/ 75/ 115 mm, adhesive zone length l = 95/ 85/ 55/ 15 mm, adherend thickness h = 4.8 mm, width W = 20 mm and adhesive gap η = 1.5 mm; while for the plasma treated specimens main changes in dimensions were a total specimen length L = 200 mm with a pre-crack length of 75 mm, an adhesive zone length l = 100 mm, adherend thickness 4.1 mm and adhesive gap η = 1/ 1.5/ 2 mm. Ten specimens were tested for each different condition. The mixed mode and fatigue testing specimens all share the same dimensions as DCB plasma treated samples.

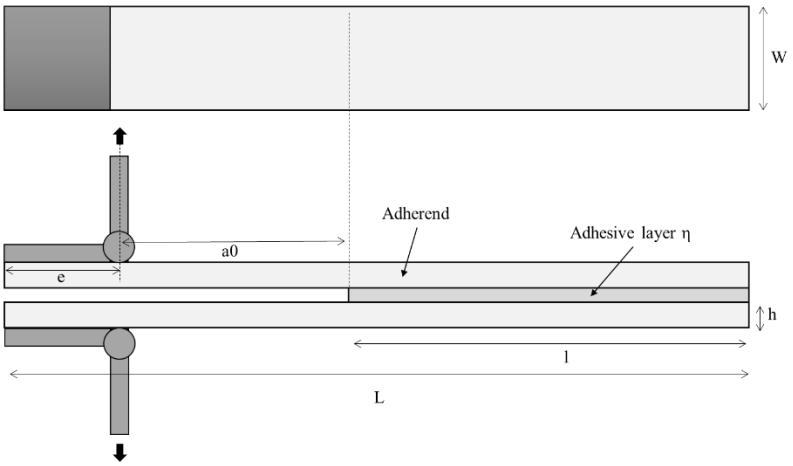

Figure 11: DCB specimen dimensions where L is the total length of the specimen, l is the adhesive bonded length, e is the hinge length, a0 is the initial crack length, w is the width of the specimen and h is the adherend material thickness

Table 3: DCB specimen dimensions for the present work

TEST	Surf. Prep.	Length [mm]	Width [mm]	Adherend Thickness [mm]	Adhesive Gap [mm]	Adhesive Area [mm^2]	Crack Length [mm]	N° Spec.
DCB	Sandblasted	155	20	4.8	1.5	20 x (95/ 85/ 55/ 15)	35/ 45/ 75/ 115	10 x 4
	Plasma	200	20	4.1	1/ 1.5/ 2	20 x 100	75	10 x 5
	Plasma / E-coated	200	20	SMC 4.1 / Aluminum 6	1.5	20 x 100	75	10

3.4.2 Flexural loaded bonded specimen for Mode II fracture energy (ENF)

ENF test was selected to investigate the Mode II fracture energy of adhesively bonded joints (See Section 2.5.2 and Table 4). Specimens' main dimensions can be seen on Figure 12. For sandblasted specimens the dimensions were total specimen length L = 200 mm, arm's length e = 50 mm, a pre-crack length a0 = 30 mm, adhesive zone length l = 150 mm, width W = 20 and adhesive gap η =1.5 mm; while for plasma treated specimens' main dimensions changes were the adherend thickness h = 4.1 mm. Ten specimens were tested for each condition.

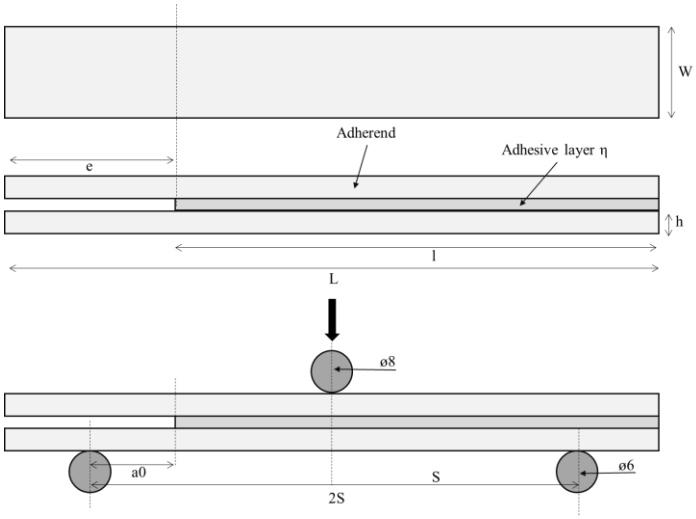

Figure 12: ENF dimensions: L length, l bonded length, e length of the free arms, a0 initial crack length, w width and h adherend thickness, while S is half the span length in contact with the rollers.

Table 4:ENF specimen dimensions for the present work

TEST	Surf. Prep.	Length [mm]	Width [mm]	Adherend Thickness [mm]	Adhesive Gap [mm]	Adhesive Area [mm^2]	N° Spec.
ENF	Sandblasted	200	20	4.8	1.5	20 x 150	10
	Plasma	200	20	4.1	1.5	20 x 150	10 x 3

3.4.3 Shear loaded bonded specimen (SLJ)

SLJ test was selected to investigate the shear stress of adhesively bonded joints (See Section 2.5.3). Specimens' main dimensions can be seen on Figure 13. For plasma treated specimens the dimensions changes were the adhesive area of A (W x l) = 25.4 x 15 mm, adhesive gap η = 1/ 1.5/ 2 mm and adherend thickness h = 4.1 mm. Ten specimens were tested for each condition (See Table 5).

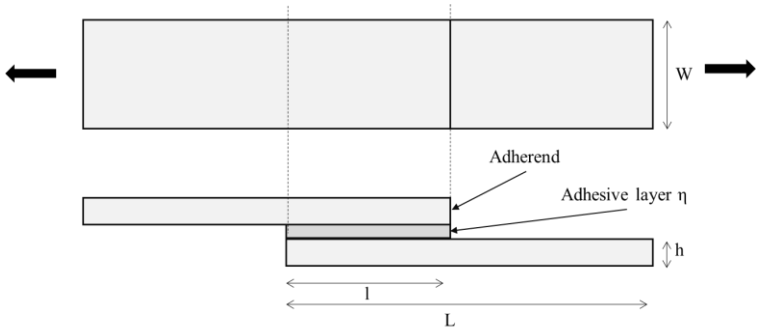

Figure 13: SLJ specimen dimensions where L is the total length of the adherend, l is the adhesive bonded length, w is the width of the specimen and h is the adherend material thickness.

Table 5: SLJ specimen dimensions for the present work

TEST	Surf. Prep.	Length [mm]	Width [mm]	Adherend Thickness [mm]	Adhesive Gap [mm]	Adhesive Area [mm^2]	N° Spec.
SLJ	Plasma	101.6	25.4	4.1	1/ 1.5/ 2	25.4 x 15	10 x 5
	E-coated	101.6	25.4	3	1.5	25.4 x 15	10

3.4.4 Bulk adhesive specimen for determination of tensile elastic modulus (Dogbone)

Dogbone test was selected to investigate the elastic property in tensile loading of the adhesive (See Section 2.5.4). Specimens' main dimensions can be seen on Figure 14. Specimens were made of bulk adhesive material in a uniform thickness shape of 4 mm, selecting specimen type number 4 from the ASTM standard where: outer radius RO = 25 mm, radius of fillet R = 14 mm, distance between grips d = 65 mm, gage length g = 25 mm, overall length L = 115 mm, overall width W = 19 mm, length of narrow section l = 33 mm and width of the narrow section wc = 6 mm. Ten specimens were tested.

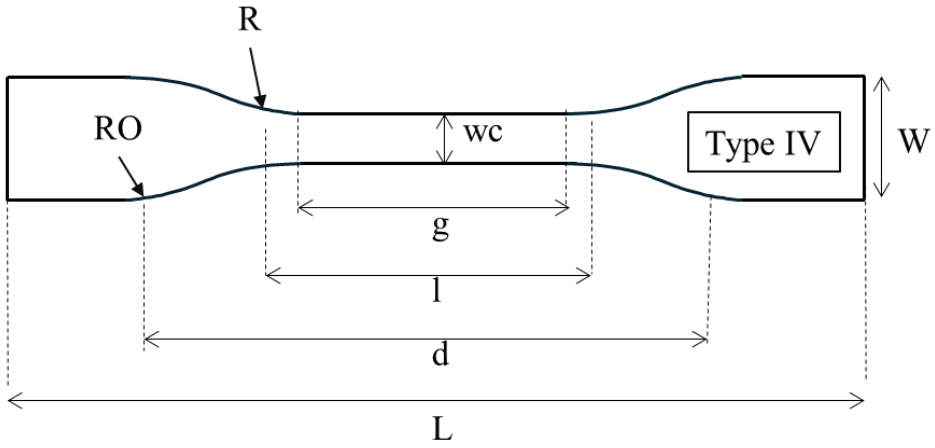

Figure 14: Dogbone specimen shape and dimensions for type 4

3.4.5 Bulk adhesive specimen for determination of shear modulus (TLS)

Thick Lap Shear test was selected to investigate the elastic property in shear loading of the adhesive (See Section 2.5.5). Specimens' main dimensions can be seen on Figure 15. Specimens were prepared similarly to standard specifications by bonding aluminum blocks with a uniform adhesive gap η = 1.5 mm, the adhesive bonded area was A = 25.4 x 15 mm, total block length L = 110 mm, short length l = 94 mm, total width W = 20.55 mm and small step length w = 9.5 mm. Ten specimens were tested.

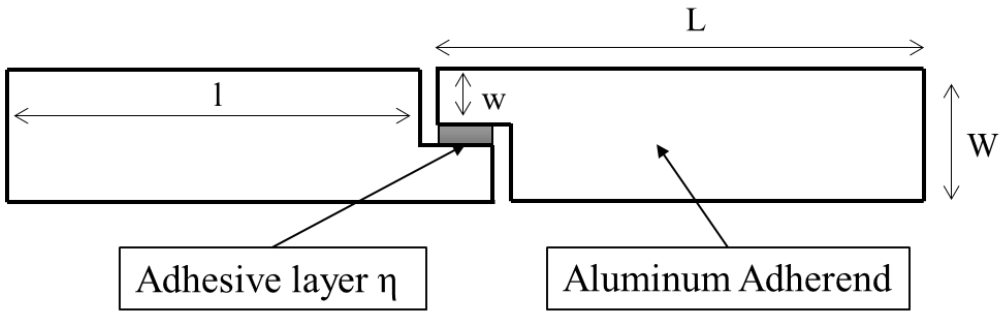

Figure 15: Thick Lap Shear specimen shape and dimensions

3.4.6 Bulk adhesive specimen for determination of tensile strength (Rod joint)

Rod Joint test was selected to investigate the tensile strength of the adhesive (See Section 2.5.6). Specimens' main dimensions can be seen on Figure 16. Two cylindrical steel rods with a diameter of 10 mm and 30 mm length were bonded with a 1.5 mm uniform adhesive gap. Ten specimens were tested.

3.4.7 Bulk adhesive specimen for the determination of Mode I fracture energy (CT)

Compact Tension test was selected to investigate the Mode I fracture energy of the adhesive (See Section 2.5.7). Specimens main dimensions can be seen on Figure 17, with a specimen thickness of 15 mm following ASTM standard specifications where length L = 37.5 mm, Height H = 36 mm, width up to the hole W = 30 mm, hole-to-side length h = 9.8 mm, pre-crack length a0 = 15 mm and a pin diameter of d = 7.5 mm. Ten specimens were tested.

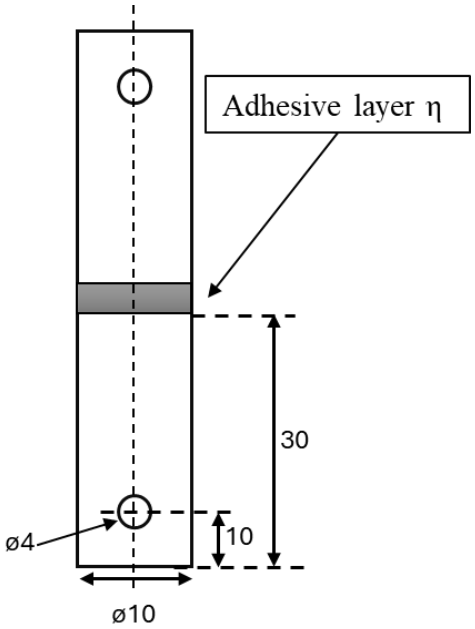

Figure 16: Rod joint specimen shape and dimensions

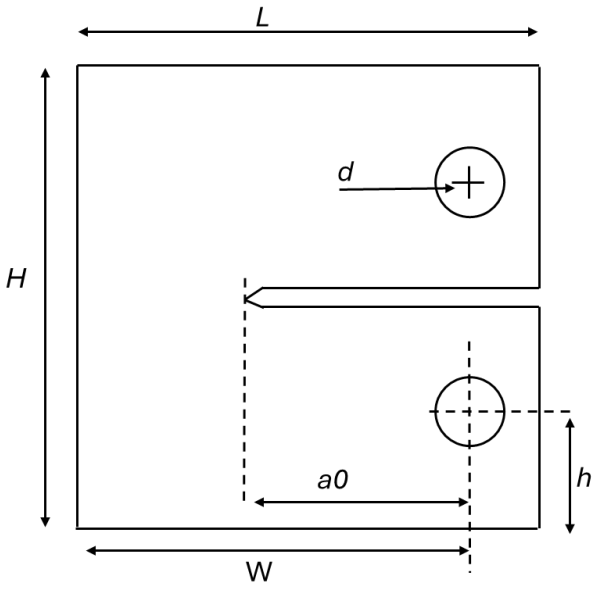

Figure 17: Compact Tension specimen shape and dimension

Chapter 4: Experimental identification of geometric parameters of the specimens to correctly characterize the adhesion properties of a joint.

4.1 Introduction

This exploration campaign was designed to obtain an experimental identification of the geometric parameters of the adhesively bonded specimens and aims to establish a robust framework for the reliable evaluation of joint integrity and performance, in accordance with established ASTM standards for adhesive testing.

The reasons for analyzing geometric effects as a distinct phase of this research lie in the high sensitivity of fracture mechanics parameters on components' structural response. Particularly, in specimens involving heterogeneous substrates, like SMC, the measured energy release rate is not solely a material property but is significantly influenced by the global stiffness and the stress distribution within the adherends. If the geometry or other secondary processes are not optimized, parasitic phenomena can precede the cohesive failure of the adhesive, leading to an incorrect characterization of the bondline. Therefore, this chapter evaluates these geometric variables to decouple the intrinsic adhesive performance from the specimen's structural constraints, ensuring that the subsequent material cards are based on valid fracture events rather than geometry-induced effects.

This investigation was needed to check the suitability of an ASTM-compliant specimen dimensions to analyze the correlation between the microstructure of the material, the production process and the surface preparation with a particular focus on the integrity and performance of the hinges bonded area.

4.2 Materials and methods

4.2.1 Specimen definition

To investigate and determine optimized geometrical parameters of samples an experimental testing campaign was planned. Four sample types for DCB tests were selected with distinct crack length of 35, 45, 75 and 115 mm as main parameters (See Section 3.3). As for Section 0, to investigate the ENF Mode II flexural failure, three distinct types of specimens were manufactured where one is a classic ENF specimen used for both sandblasted and plasma treated samples. A second type is made for plasma treated samples by gluing the full length of the specimen and inserting a plastic sheet between the arms up to the initial crack length. A third

specimen type was made by inserting a frictionless shim in between the arms of the specimen. These methodologies have the main goal of facilitating the relative movements of the ENF free arms and so enhancing the crack initiation within the adhesive layer (See Section 0). For SLJ specimens slipping of the clamping fixture is observed on the specimen surface; the issue was solved by applying sandpaper on the specimen in correspondence to the gripping fixture (See Section 3.4.3). Mechanical test results are presented and discussed in Section 4.2.2 while fractographic evidence are presented in Section 4.4.

4.2.2 Mechanical Testing

The tests were carried out on an Instron Universal testing machine with a 10 kN load cell equipped with a fixture that connects to the specimen, ensuring correct alignment to minimize bending moments. All specimens were pre-loaded at 5 N and the test was conducted at a constant crosshead speed of 2 mm/min for DCB until total opening of the specimen, not performing the unloading part of the test described in the standard; for ENF the test was conducted at a constant crosshead speed of 0.5 mm/min until failure and for SLJ the test was conducted at 13 mm/min until failure. Pictures of the testing phase are presented in Figure 18. For this phase samples with a 1.5 mm adhesive thickness were tested for a total of 90 specimens:

- N° 10 specimens for DCB sandblasted specimens with a pre-crack of 35 mm.
- N° 10 specimens for DCB sandblasted specimens with a pre-crack of 45 mm.
- N° 10 specimens for DCB sandblasted specimens with a pre-crack of 75 mm.
- N° 10 specimens for DCB sandblasted specimens with a pre-crack of 115 mm.
- N° 10 specimens for ENF sandblasted specimens.
- N° 10 specimens for ENF plasma treated specimens.
- N° 10 specimens for ENF plasma treated specimens with a plastic sheet.
- N° 10 specimens for ENF plasma treated specimens with a frictionless shim.
- N° 10 specimens for SLJ plasma treated specimens

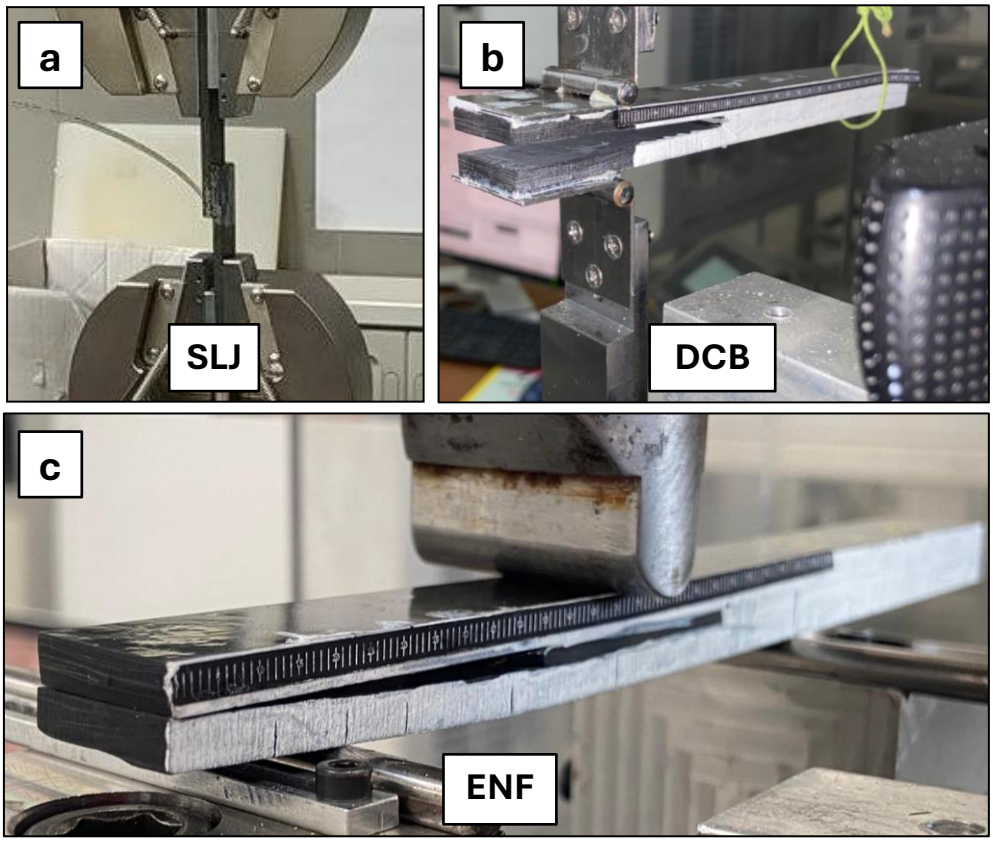

Figure 18: Specimens during mechanical testing phase: a) Single Lap Joint, b) Double Cantilever Beam and c) End Notch Flexure

4.3 Mechanical testing results

4.3.1 DCB Results

Force-Displacement results from DCB test are reported in Figure 19 where only one most representative sample results for each series are shown to support the direct comparison of the different conditions. Between samples, the coefficient of variations of mean values of mean values ranges from 10% to 28%; this relatively wide range can be a consequence of the high variability of the SMC material, both in terms of fiber direction and distribution. A clear trend can be observed among the specimens with pre-crack lengths of 35, 45, 75 and 115 mm. As the initial crack length increases, both the stiffness and the maximum load decrease, while the overall displacement at failure increases. The specimen with a 35 mm pre-crack shows a brittle response, with a sharp drop after the peak indicating adherend failure around a registered displacement of 3.8 mm, while the 45 mm and 75 mm samples exhibit more progressive crack growth with a relative displacement at peak force respectively around 8 and 16 mm.

For the 115 mm pre-crack specimen, the response is characterized by the lowest stiffness and a gradual load decrease after the peak, suggesting a more controlled energy release during delamination with a relative displacement at peak load of 48 mm.

Fracture energy comparison can be seen in Figure 20. The experimental data for the 35 mm pre-crack specimens were excluded from the statistical analysis due to a high rate of unwanted failure modes, primarily involving hinge debonding and subsequent re-bonding. This resulted in an insufficient number of valid specimens to constitute a statistically significant population according to ASTM standards. Consequently, to ensure the reliability and robustness of the comparative study, only the 45, 75, and 115 mm configurations (which provided a consistent and sufficient sample size) were considered for the definitive analysis. The corresponding mean and standard deviation values of the fracture energy and peak force are summarized in Table 6.

This significant scatter in the experimental data is attributable to the inherent heterogeneity of SMC substrate. Unlike continuous fiber composites, the random orientation and non-uniform distribution of chopped fibers lead to localized variations in flexural modulus along the DCB arms. Since the calculation of the strain energy release rate is sensitive to local stiffness, any fluctuation in density or orientation directly translates into a wider standard deviation.

Table 6: Results values for DCB tests: peak load and fracture energy comparison based on initial crack length

TEST	Surf. Prep.	Crack Length [mm]	Mean G_Ic [J/m^]	G_std. Dev.	Mean Peak Load [N]	Load_std. Dev.
DCB	Sandblasted	35	1436.59	146.7	251.12	25.19
	Sandblasted	45	3707.45	749.47	278.31	20.93
	Sandblasted	75	2930.07	504.36	177.91	6.91
	Sandblasted	115	4202.91	1209.3	124.13	14.75

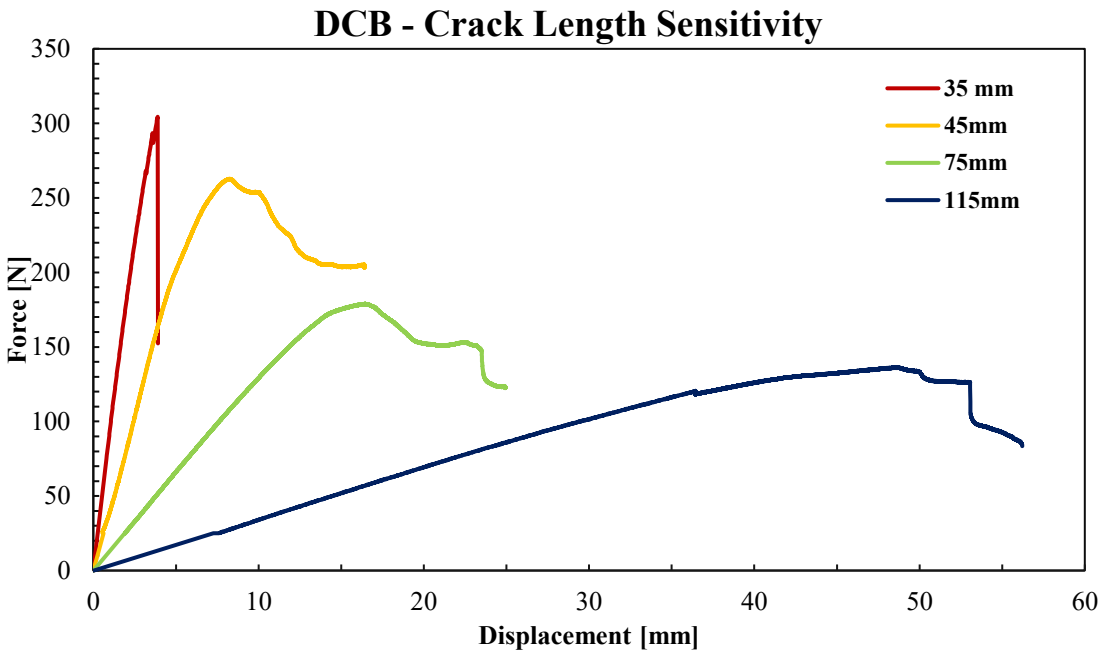

Figure 19: Results from mechanical testing of DCB: analysis of crack length influence

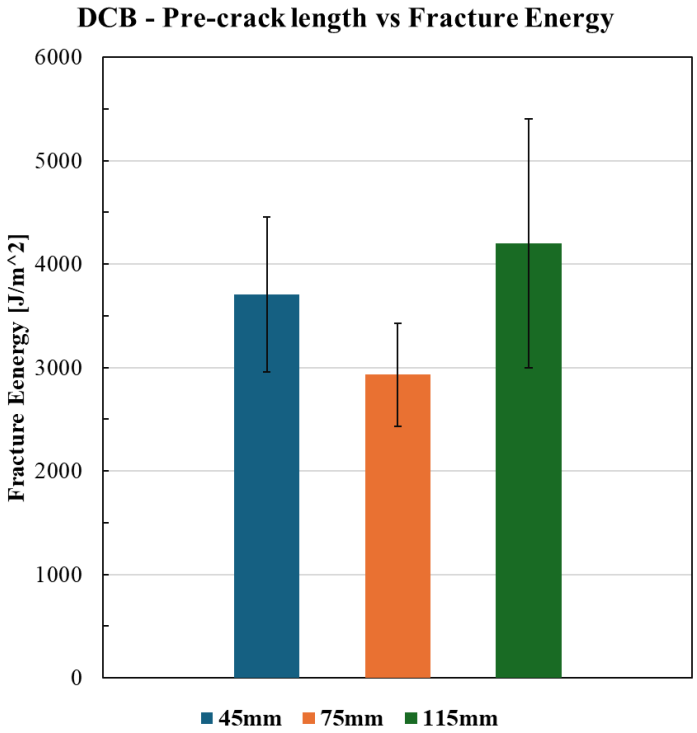

Figure 20: Comparison of Fracture Energy for DCB sandblasted specimens.

4.3.2 ENF Results

Force-Displacement results from ENF test are reported in Figure 21 where only one most representative sample results for each series are shown to support the direct comparison of the different conditions. Between samples, the coefficient of variations of mean values of mean values ranges from 10% to 25%, confirming the SMC properties variability. All specimens show a brief linear trait up to 100 N with a slight increase in stiffness up to flexural adherend failure at 2600 N for sandblasted specimens, clearly visible from the sharp drop in force. For plasma treated specimens, data were more overlapping on the first linear trait up to 2500 N for standard specimens and 4500 N for specimens with a plastic sheet in between the arms while the frictionless shim specimens showed a more consistent linear trait up to failure. All specimens in general showed variability up to flexural failure after the linear trait, probably caused by the SMC failing with relative displacements at break between 2.7 and 4 mm registered from the testing machine. Means and standard deviations values for fracture energy and peak force are showed in Table 7.

Values of fracture energy must be considered as "apparent" as they are calculated from ASTM standards specifications on the first flexural failure during testing and not, as usually expected, on the adhesive failure.

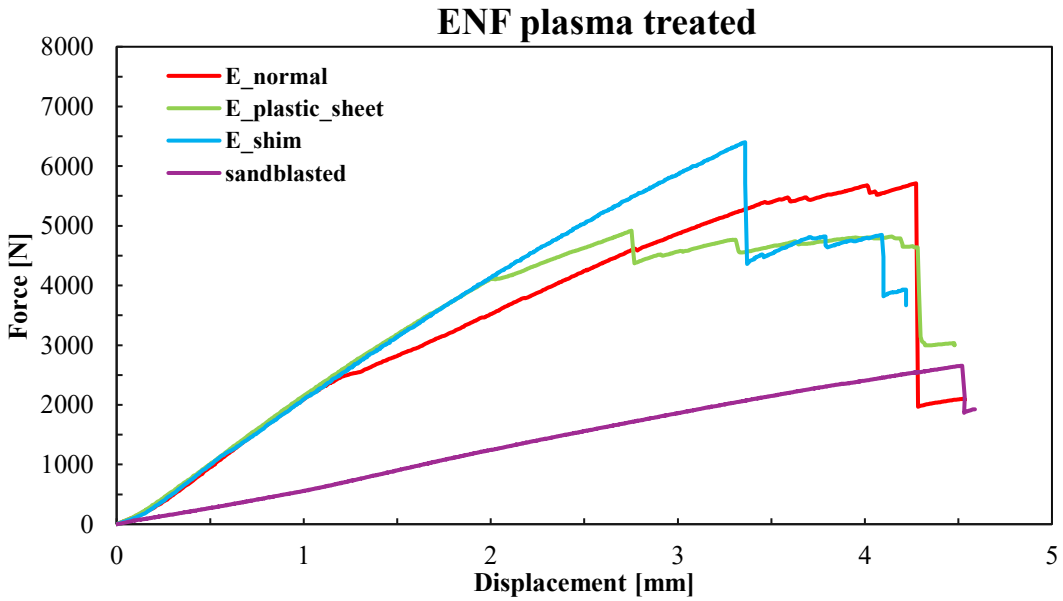

Figure 21: Results from mechanical testing of ENF: comparison between sandblasted specimens and plasma treated specimens with different aid tools

Table 7: Results values for ENF tests: peak load and fracture energy comparison based on different aid tools.

TEST	Surf. Prep.	Aid Tool	Mean G_IIc [J/m^]	G_std. Dev.	Mean Peak Load [N]	Load_std. Dev.
ENF	Sandblasted	None	6971.62	1403.48	2694.14	308.22
	Plasma	None	14324.25	3650.99	5803.73	456.02
	Plasma	Plastic sheet	13168.98	1048.47	5768.37	726.72
	Plasma	Frictionless Shim	13658.51	1442.2	6722	402.02

4.3.3 SLJ Results

Force-Displacement results from SLJ shear test are reported in Figure 22 where only most representative sample result is shown. Between samples, the coefficient of variations of mean values is less than 10%. A great variation in behavior is visible with a linear trait up to 400 N and a peak force of less than 2000 N. Means and standard deviations values for shear stress and peak forces are showed in Table 8.

While sandblasting was utilized as a reliable baseline for the geometric calibration in DCB and ENF tests, the SLJ testing phase was exclusively dedicated to an investigative screening of the atmospheric plasma treatment process to evaluate plasma-activated interface sensitivity. As shown in Figure 22 and Table 8, plasma-treated specimens exhibited a peak load of approximately 2000 N. Although this value is lower than the structural limits observed in other applications, the visual inspection of the fracture surfaces (see Section 4.4.3) provides critical insights: a thin veil of adhesive is clearly visible across the entire bonded area of the substrates. This evidence confirms that the failure is not purely adhesive but rather a thin-layer cohesive failure. The reduced peak load is therefore not attributable to a lack of interfacial adhesion, but to a localized stress concentration within the non-optimized boundary layer of the adhesive, which promoted crack initiation at lower global stress levels.

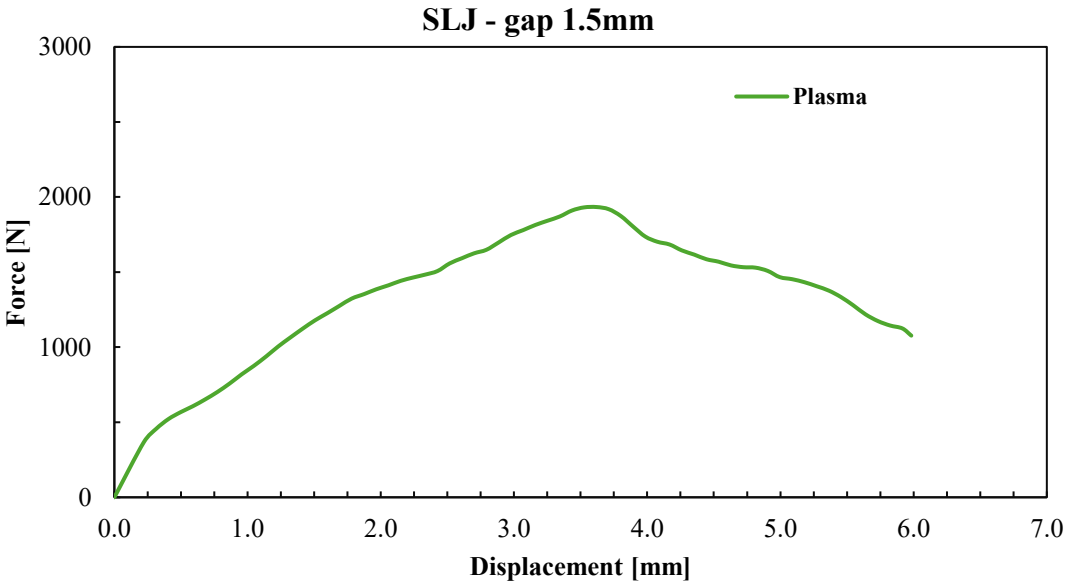

Figure 22: Mean results from mechanical testing of SLJ

Table 8: Results values for SLJ tests: peak load and shear stress

TEST	Surf. Prep.	Bonded Area [mm^2]	Mean Shear Stress [Mpa]	Shear_std. Dev.	Mean Peak Load [N]	Load_std. Dev.
SLJ	Plasma	25.4 x 15	6.06	0.65	2003.1	214

4.4 Fracture Surfaces

4.4.1 DCB Fracture surfaces

DCB tests showed a majority of the 35 mm pre-crack specimens exhibited undesirable failure modes such as hinge debonding and substrate failure adjacent to the bondline, characterized by the delamination of thin SMC layers (a mode often referred to as Light-Fiber Tear (LFT) - Figure 23). This phenomenon can be attributed to the high flexural stiffness of the DCB arms associated with the shorter 35 mm initial crack length. In this configuration, the reduced lever arm necessitates significantly higher loads to reach the critical energy required for crack propagation. Such loading conditions induce a severe stress concentration in the bonded area beneath the loading blocks, exceeding the interlaminar strength of the SMC substrate or the hinge-to-adherend interface before a stable cohesive crack can initiate within the adhesive layer. Consequently, the high peak stresses promote hinge debonding and Light-Fiber Tear (LFT) rather than the desired cohesive failure, confirming that a longer initial crack is necessary to mitigate the influence of specimen stiffness on the fracture process. These tests successfully demonstrated that an initial crack length of at least 45 mm was necessary to mitigate hinge debonding and achieve a more stable failure condition. Failure surfaces of most representative specimens are showed in Figure 24.

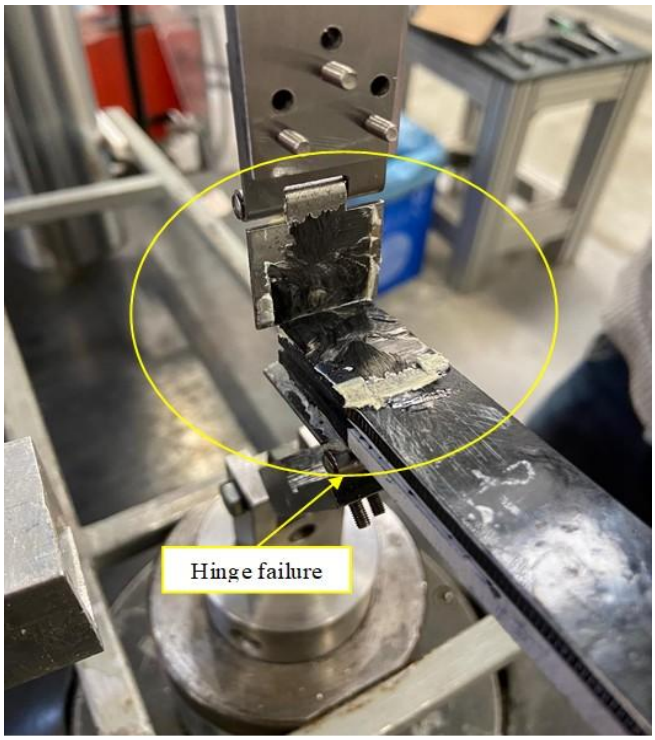

Figure 23: Sandblasted DCB specimen with 35 mm initial crack length exhibiting hinge debonding by fiber tearing.

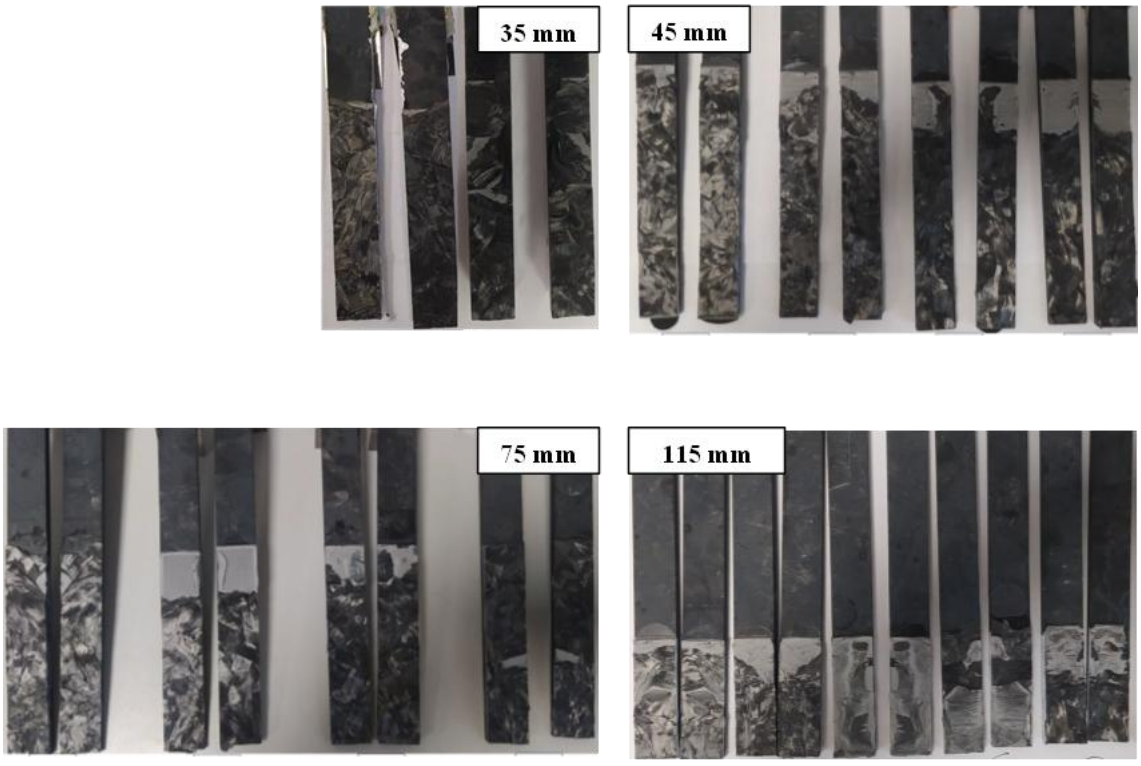

Figure 24: Fracture surfaces of DCB sandblasted specimens depending on initial crack length

4.4.2 ENF fracture surfaces:

ENF test methodology proved to be unsuitable for characterizing the Mode II fracture energy: for all tested specimens the failure mode was caused by flexural fracture of the lower SMC adherend before any crack propagation occurred within the adhesive layer (See Figure 25). This outcome is a direct result of the material combination: the high toughness and strength of the polyurethane adhesive in shear significantly exceeded the flexural strength of the relatively brittle SMC substrate. While the calculated apparent fracture energy values are reported in Table 7 for completeness, they do not represent the adhesive's intrinsic, G_{II} . Instead, they may reflect the total energy absorbed by the entire joint system up to the point of substrate flexural failure. For plasma treated specimens, despite modifications to the test setup (ex. using low-friction films between the specimen arms, altering support spans), the outcome remained unchanged: all specimens failed via substrate flexural fracture, confirming that the ENF test is fundamentally not viable for characterizing, G_{II} for this material system.

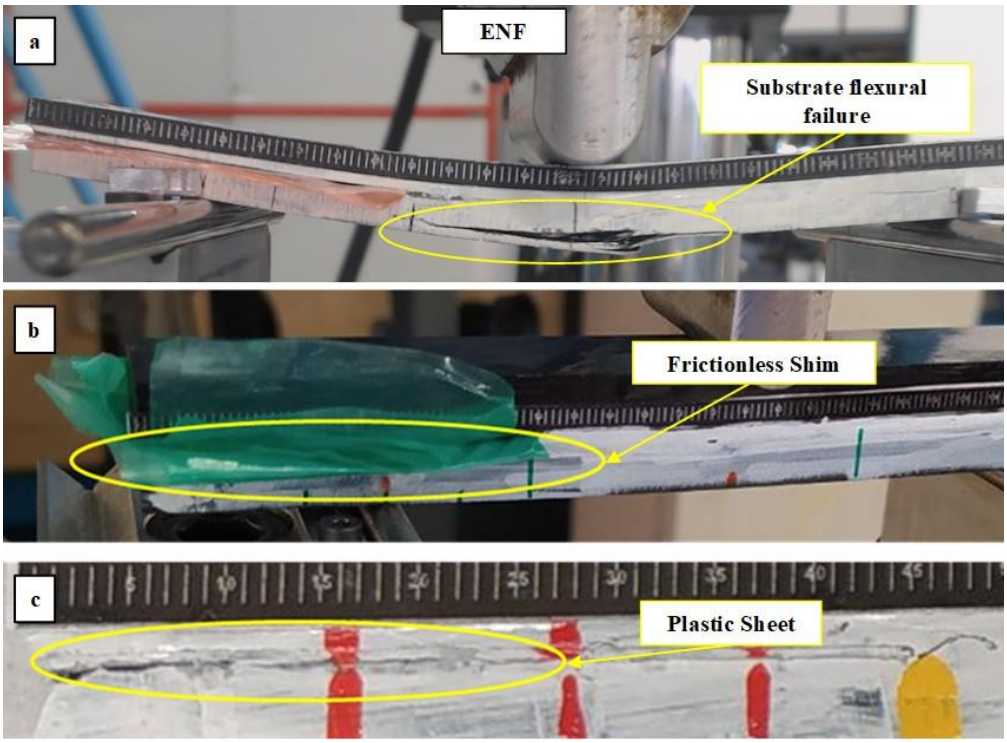

Figure 25: ENF specimens during mechanical test: a) normal ENF specimen experiencing flexural failure of the substrate, b) ENF specimen with frictionless shim between free arms and c) ENF specimen with a plastic sheet between the adhesive layers.

4.4.3 SLJ fracture surfaces:

The fracture surfaces of the plasma-treated SLJ specimens (Figure 26) reveal a distinct failure morphology. Despite the macroscopic appearance of interfacial debonding, a closer inspection confirms the presence of a continuous thin film of polyurethane adhesive remaining on the SMC surface. This thin veil (visually identified with a difference in color between the adhesive thin layer in gray and the adherend material in black) indicates that the atmospheric plasma treatment successfully activated the surface energy of the SMC, facilitating a chemical bond that somehow exceeded the internal strength of the adhesive in the immediate proximity of the interface.

Figure 26: Fracture surfaces of plasma treated SLJ specimens: a difference in colors may be observed on SMC bare adherend, debonded surface with thin-veil adhesive and adhesive layer. Also, on the first specimen from the left, small patches of detached adhesive material are visible.

4.5 Conclusion

The comprehensive experimental program clarified fundamental limitations and optimal procedures for characterizing the adhesion properties of polyurethane-bonded Carbon-SMC joints

DCB tests revealed a clear trend of decreasing stiffness and peak load with increasing pre-crack length, as already known from literature, identifying 45mm as the minimum suitable threshold for stable crack propagation for this specific case study of SMC-to-polyurethane adhesive.

ENF tests demonstrated that this configuration is unsuitable for Mode II characterization of this material system, since all failures occurred in the SMC substrate rather than within the adhesive layer, confirming that the measured energy represents substrate bending rather than interfacial shear toughness.

SLJ tests identified the high sensitivity of plasma-treated interfaces to process parameters. The observed thin-layer cohesive failure (thin veil) demonstrates that chemical adhesion was achieved, although the global strength was influenced by the specific experimental setup, highlighting the need for rigorous process control for the next phases and especially in general industrial plasma applications.

Chapter 5: Assessing the influence of adhesive thickness in bonded joints.

5.1 Introduction

The analysis of adhesive layer thickness represents a critical aspect of this study. Variations in the adhesive gap in this case are an inherent consequence of SMC manufacturing processes, where surface waviness, fiber architecture and part tolerances prevent the achievement of a uniform bondline. Unlike idealized laboratory specimens, bonded components in real automotive production exhibit spatially varying adhesive thickness, which directly affects local stress states, deformation modes and energy dissipation within the adhesive layer.

Bondline thickness variability influences fracture mechanisms by also altering the balance between peel and shear stresses, modifying constraint conditions and changing the extent of plastic deformation preceding crack initiation. Thicker adhesive layers tend to promote increased ductile deformation and energy dissipation, while thinner regions may lead to higher stress concentrations, premature damage initiation and transition toward more brittle fracture responses. As a result, fracture behavior cannot be completely described by a single set of cohesive parameters without explicitly accounting for thickness effects.

Addressing adhesive thickness effects is thus essential not only for improving joint reliability, but also for developing predictive and transferable adhesive material models capable of representing realistic manufacturing conditions and supporting robust CAE-based design.

5.2 Materials and Methods

5.2.1 Specimen definition

Specimens for both DCB and SLJ tests for this phase follow the same dimensions as described in Section 3.3. They will be kept the same for the subsequent mechanical testing specimens. Mechanical test results are presented and discussed in Section 5.3 while fractographic evidence are presented in Section 5.4. Adherends were Carbon-SMC for both DCB and SLJ samples; adhesive employed was polyurethane Parker LORD. A plasma surface optimized treatment was chosen as main surface preparation of interest for subsequent studies, especially accounting for the low performance from specimen of Section 0 that differs from previously tested SLJ specimens from archives.

5.2.2 Mechanical Testing

The tests were carried out on a ZwickRoell Z010 Universal testing machine with a 10 kN load cell equipped with a fixture that connects to the specimen, ensuring correct alignment to minimize any bending moments. All specimens were pre-loaded at 5 N and the test was conducted at a constant crosshead speed of 2 mm/min for DCB until total failure of the specimen, not performing the unloading part of the test described in the standard and for SLJ the test was conducted at 1.27 mm/min until failure. Pictures of the testing phase are reported in Figure 27, following same ASTM-compliant procedure as previous tests from the same tests (See Section 3.4.1and Section 3.4.3 for reference).

For this phase samples were tested with a 75 mm pre-crack for DCB and an adhesive zone of 25.4 x 15 m for SLJ for a total of 60 specimens:

- N° 10 specimens for DCB plasma treated specimens with adhesive thickness of 1 mm.
- N° 10 specimens for DCB plasma treated specimens with adhesive thickness of 1.5 mm.
- N° 10 specimens for DCB plasma treated specimens with adhesive thickness of 2 mm.
- N° 10 specimens for SLJ plasma treated specimens with adhesive thickness of 1 mm.
- N° 10 specimens for SLJ plasma treated specimens with adhesive thickness of 1.5 mm.
- N° 10 specimens for SLJ plasma treated specimens with adhesive thickness of 2 mm.

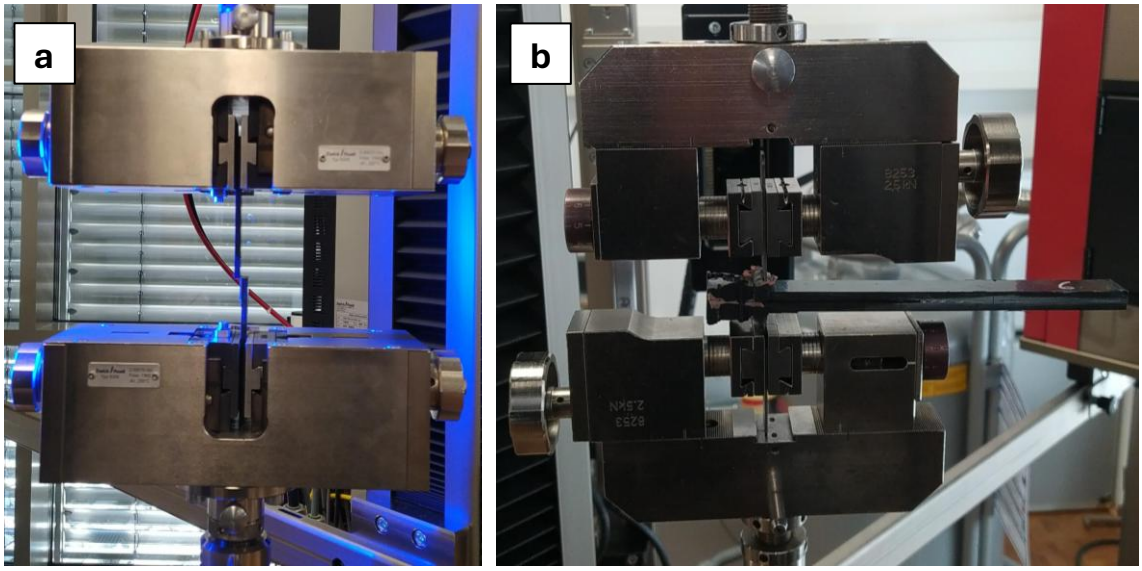

Figure 27: New experimental setup for adhesive gap investigation of a) SLJ and b) DCB specimens

5.3 Mechanical testing results

5.3.1 DCB Results

Force-Displacement results from DCB test are reported in Figure 28 where only one most representative sample results for each series are shown to support the direct comparison of the different conditions. Between samples, the coefficient of variations of mean values is greater than 15%. Force–displacement curves from DCB tests conducted with adhesive gaps of 1, 1.5 and 2 mm reveal an initial linear response up to approximately 80–100 N for all configurations, indicating comparable initial stiffness across the tested bondline thicknesses. The maximum load attained varies slightly between specimens, reaching approximately 78 N for the 1 mm gap, 83 N for the 1.5 mm gap and 105 N for the 2 mm gap. Following peak load, all specimens display plateau behavior with minor undulations, maintaining elevated loads up to displacements in the range of 30–35 mm; no abrupt load drops or brittle failure modes are observed. The displacement at failure is therefore similar for all adhesive gap configurations, generally around 30 mm. The average mode I fracture energy (GIc) is of the same order for all groups (approximately 1100–1265 J/m^2), with the 1.5 mm gap specimens exhibiting the largest standard deviation, indicative of greater experimental variability in this case. Means and standard deviations values for fracture energy and peak force are showed in Table 9.

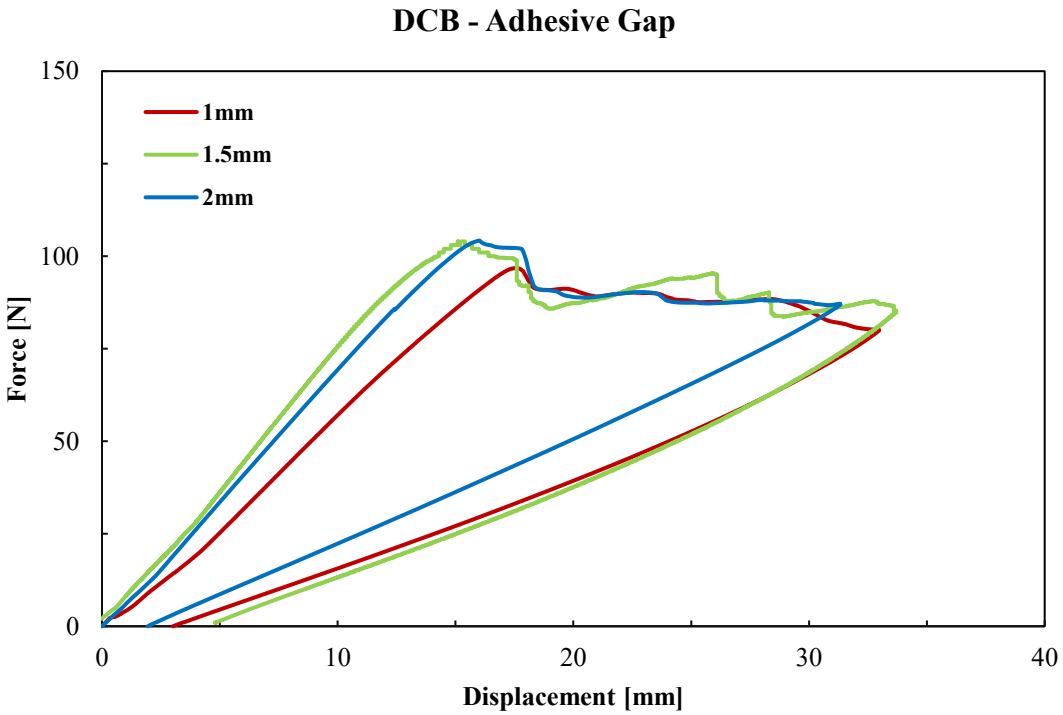

Figure 28: Results from mechanical testing of DCB: influence of the adhesive thickness

Table 9: Mean experimental results from DCB adhesive gap investigation

TEST	Adhesive gap [mm]	Crack Length [mm]	Mean G_Ic [J/m^]	G_std. Dev.	Mean Peak Load [N]	Load_std. Dev.
DCB	1	75	1174.51	204.46	78.3	12.02
	1.5	75	1085.46	432.88	83.5	43.28
	2	75	1265.33	313.81	105.44	26.15

5.3.2 SLJ Results

Force-Displacement results from SLJ shear test are reported in Figure 29 where only one most representative sample results for each series are shown to support the direct comparison of the different conditions. Between samples, the coefficient of variations of mean values is less than 10%. Force–displacement curves from SLJ shear tests for adhesive gaps of 1, 1.5 and 2 mm demonstrate an overlapping initial linear segment up to approximately 1100 N, evidencing similar initial shear stiffness among all specimens. Beyond this region, all configurations exhibit ductile behavior, with force increasing gradually to a peak followed by a characteristic descending branch after damage onset. The maximum load values observed from the curves are approximately 2300 N for the 1 mm gap, 3300 N for the 1.5 mm gap and 2500 N for the 2 mm gap. This trend is consistent with the mean peak load values reported in Table 10, which indicate 2655 N, 3276 N and 2686 N, respectively, for the three configurations.

Notably, the specimens with a 1.5 mm gap attained the highest shear stress at failure (8.6 MPa). These results collectively indicate that peak performance in terms of shear stress and load is achieved for the 1.5 mm adhesive gap configuration, while increasing the gap to 2 mm does not further enhance and may even limit joint strength under shear loading. Means and standard deviations values for shear stress and peak force are showed in Table 10.

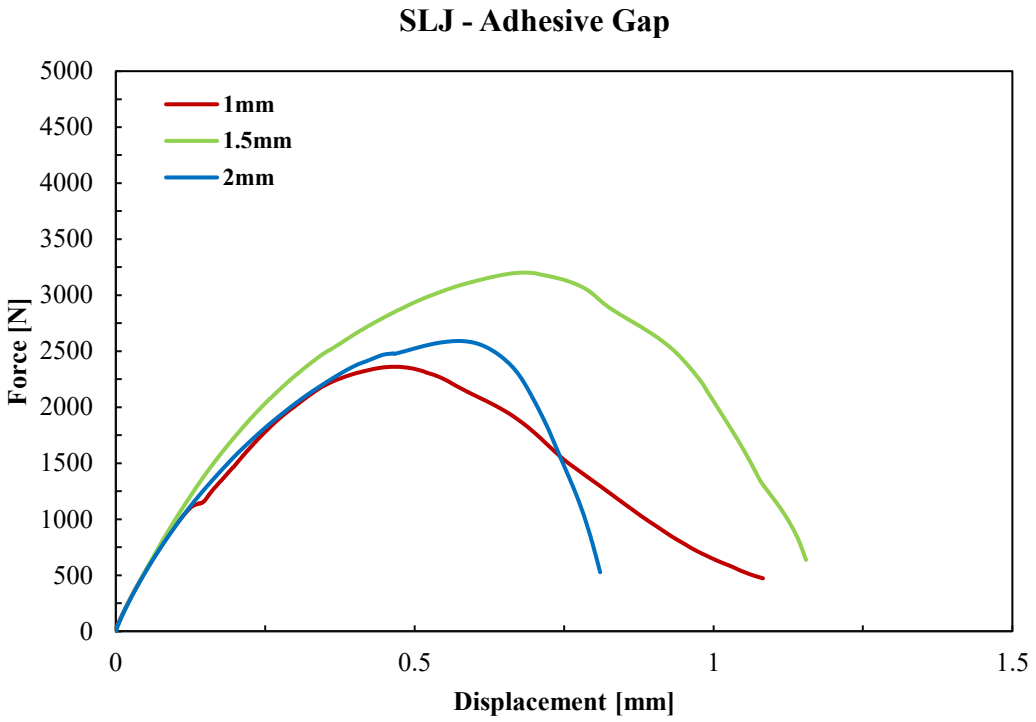

Figure 29: Results from mechanical testing of SLJ: influence of adhesive thickness

Table 10: Mean experimental results for SLJ adhesive gap investigation

TEST	Adhesive gap [mm]	Bonded Area [mm^2]	Mean Shear Stress [Mpa]	Shear_std. Dev.	Mean Peak Load [N]	Load_std. Dev.
SLJ	1	25.4 x 15	6.97	0.55	2655.57	209.55
	1.5	25.4 x 15	8.6	0.73	3276.6	278.13
	2	25.4 x 15	7.05	0.55	2686.05	209.55

5.4 Fracture Surfaces

Detailed inspection of the fracture surfaces from both DCB and SLJ specimens revealed an apparent adhesive mode of failure across all adhesive gap configurations. Notably, in the 1.5 mm gap samples, small cohesive patches of adhesive were observed on the adherend, indicating a localized and possibly suboptimal adhesion process that could arise from local gap non-uniformity or surface condition. High-resolution fractographic analysis confirmed that the failure mechanism remains consistently co-exclusive within the adhesive volume, specifically transitioning to a thin-layer cohesive failure mode at the interface. Microscopic inspection revealed a persistent, albeit thin, film of polyurethane resin covering the SMC fibers, even in regions that appeared interfacial to the naked eye. This evidence negates the occurrence of purely adhesive debonding, which is often an artifact of macroscopic observation and lacks realism in high-performance structural bonding. For DCB specimens, after an initial propagation phase of approximately 10–15 mm, crack deviation from the adhesive layer into the carbon adherend was frequently detected, suggesting a transition from interfacial to adherend-dominated fracture as the test progressed. This phenomenon points to a possible mismatch in property gradients within the joint, leading to redirection of the crack path under sustained loading. A comparison for both SLJ shear strength and DCB Mode I fracture energy for this adhesive gap investigation is presented in Figure 30. Failure surfaces of most representative specimens are showed in Figure 31.

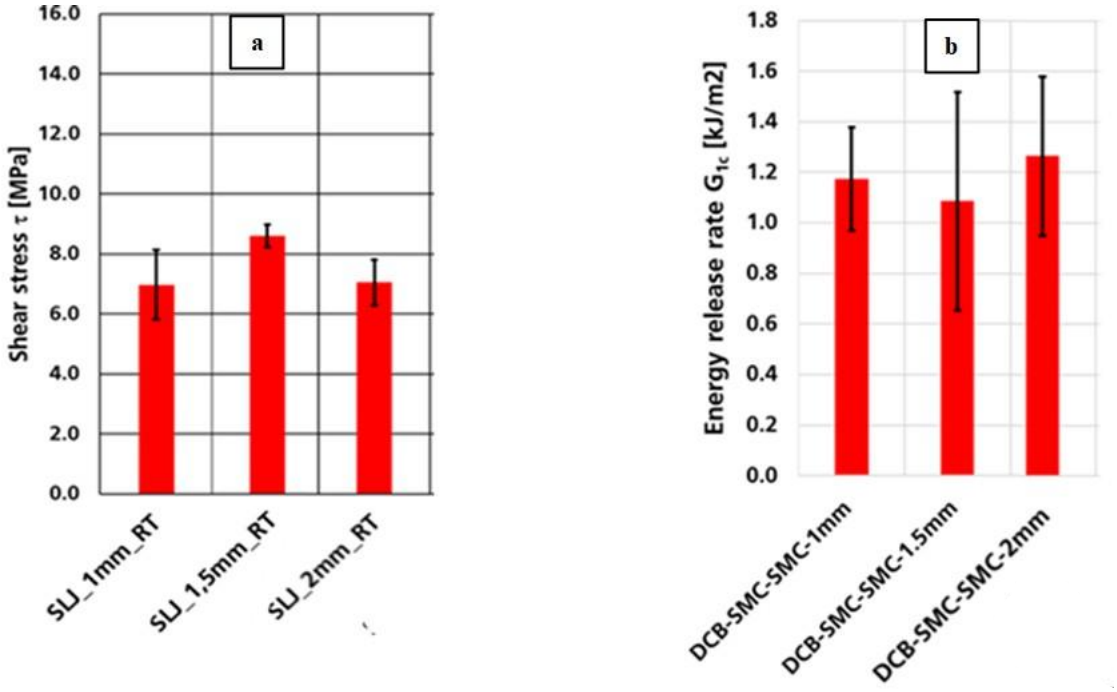

Figure 30: Comparison of adhesive thickness influence for a) SLJ specimens shear stress and b) DCB specimens fracture energy

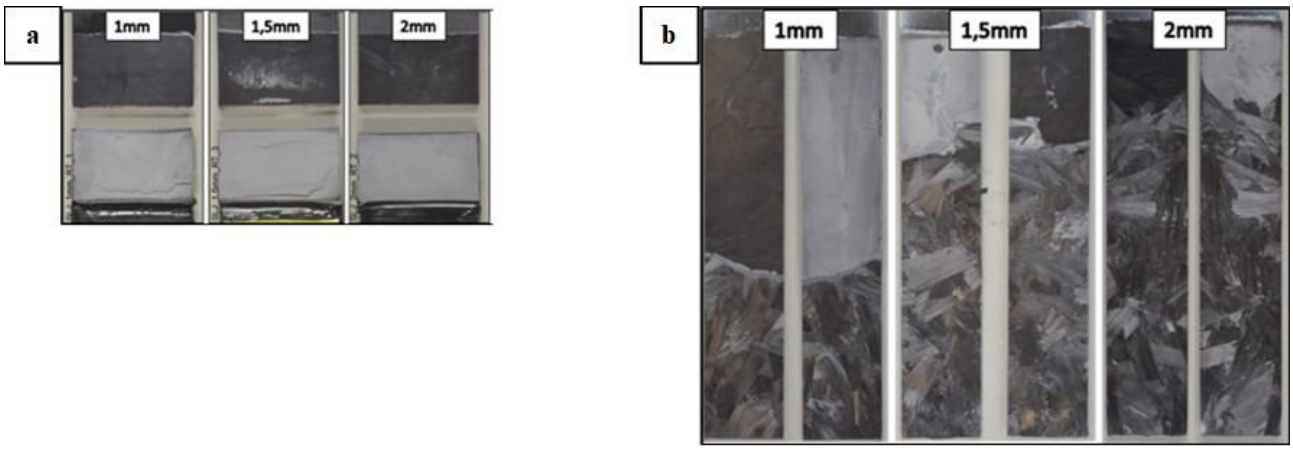

Figure 31: Fracture surfaces from adhesive thickness influence analysis: a) SLJ specimens and b) DCB specimens

5.5 Conclusion

This experimental campaign systematically elucidated the effect of adhesive gap thickness on the failure mechanisms and mechanical performance of polyurethane-bonded joints in SMC-carbon assemblies. The DCB tests demonstrated comparable fracture energies across gaps of 1, 1.5 and 2 mm, with the 1.5 mm gap exhibiting slightly lower average energy but greater dispersion, highlighting enhanced sensitivity to local variations typical of industrial manufacturing. In contrast, the SLJ tests revealed that peak load and shear strength increase with adhesive gap up to 1.5 mm, beyond which additional thickness did not confer higher strength and in fact induced a decrease, likely due to increased strain localization and altered stress distribution within the thicker adhesive layers.

The local crack deviations and the stability of the fracture process zone, particularly in DCB specimens, further demonstrate that the energy dissipation is governed by the adhesive's internal deformation capacity near the substrate, rather than a lack of interfacial adhesion.

Overall, the results confirm that optimizing the adhesive gap is crucial for maximizing joint strength and reliability in SMC/polyurethane systems, with the optimal gap for Mode I and shear performance identified between 1 and 1.5 mm.

Chapter 6: Assessing the influence of temperature in bonded joints service condition.

6.1 Introduction

Temperature critically influences the performance and reliability of adhesive joints in SMC-based structures, as both the polymeric matrix and adhesive are highly sensitive to thermal variations. Thermal excursions encountered during service or manufacturing can modify the stiffness, strength and failure mechanisms of bonded joints, resulting in significant deviations from their nominal mechanical properties. This section systematically investigates the effect of a range of temperature conditions on fracture and shear behavior, providing insights necessary for the robust design and qualification of adhesive joints in environments like service conditions.

6.2 Materials and methods

6.2.1 Specimen definition

Specimens for both DCB and SLJ tests for this phase follow the same dimensions (plasma treated, same SLJ bonded area of 25.4 x 15 mm, adhesive thickness of 1.5 mm, pre-crack length for DCB of 75 mm, dimensions, etc.) as described in Section 3.4.1and Section 3.4.3. To investigate and determine the behavior of the adhesive joint under different temperature conditions, a temperature chamber by ZwickRoell was employed. The temperature chamber was previously heated or cooled, depending on the temperature test, at constat rate until equilibrium. Humidity values were not controlled but kept below 60%. Specimens were then positioned in the gripping system and left for 2 minutes for the temperature conditioning. Mechanical test results are presented and discussed in Section 6.3 while fractographic evidence are presented in Section 6.4.

6.2.2 Mechanical Testing

The tests were carried out on a ZwickRoell Z010 Universal testing machine with a 10 kN load cell equipped with a fixture that connects to the specimen, ensuring correct alignment to minimize any bending moments. All specimens were pre-loaded at 5 N and the test was conducted at a constant crosshead speed of 2 mm/min for DCB until total failure of the specimen, not performing the unloading part of the test described in the standard and for SLJ the test was conducted at 1.27 mm/min until failure. Picture of the temperature chamber

employed for this testing phase is presented in Figure 32. The temperature chamber was electrically powered with heater, fans and Nitrogen gas barrels to be able to change inside temperature.

For this phase samples were tested for a total of 40 specimens, taking the Room Temperature data results (RT at +23 °C) from previous experiments (See Section 5.3):

- N° 10 specimens for DCB plasma treated specimens in Low Temperature (LT) at -10 °C.
- N° 10 specimens for DCB plasma treated specimens in High Temperature (HT) at +85 °C.
- N° 10 specimens for SLJ plasma treated specimens in Low Temperature (LT) at -10 °C.
- N° 10 specimens for SLJ plasma treated specimens in High Temperature (HT) at +85 °C.

Figure 32: Temperature chamber employed for DCB and SLJ in temperature tests (-10 and +85 °C)

6.3 Mechanical testing Results

6.3.1 DCB results

Force-Displacement results from DCB test are reported in Figure 33 where only one most representative sample for each series is shown to support the direct comparison of the different conditions. Variations in all measurements exceed 10%, reflecting the sensitivity of the joint system to both temperature and experimental scatter. Force–displacement curves from DCB tests conducted at low temperature (LT, –10 °C), room temperature (RT, 23 °C) and high temperature (HT, 85 °C) reveal a pronounced influence of thermal conditions on joint performance. All configurations display an initial linear segment of comparable slope, reflecting similar initial stiffness across the temperature range. LT specimens register the highest peak force, reaching approximately 110 N, followed by RT specimens with a peak of about 80–100 N. In both LT and RT cases, the transition to failure occurs at comparable displacement values and the mode I fracture energies are similar. Specimens tested at HT demonstrate a dramatically reduced maximum force (approximately 22 N) and fracture energy (near 108 J/m²), corresponding to a reduction of about 90% relative to RT specimens. The force–displacement response for HT also reveals an anomalous post-peak increase in force, which may be ascribed to temperature-induced changes in the adhesive's ductility or localized toughening mechanisms.

These findings underscore the severe degradation of adhesive performance at elevated temperatures, while confirming the comparability of joint properties under cold and ambient conditions. Means and standard deviations values for fracture energy and peak force are shown in Table 11.

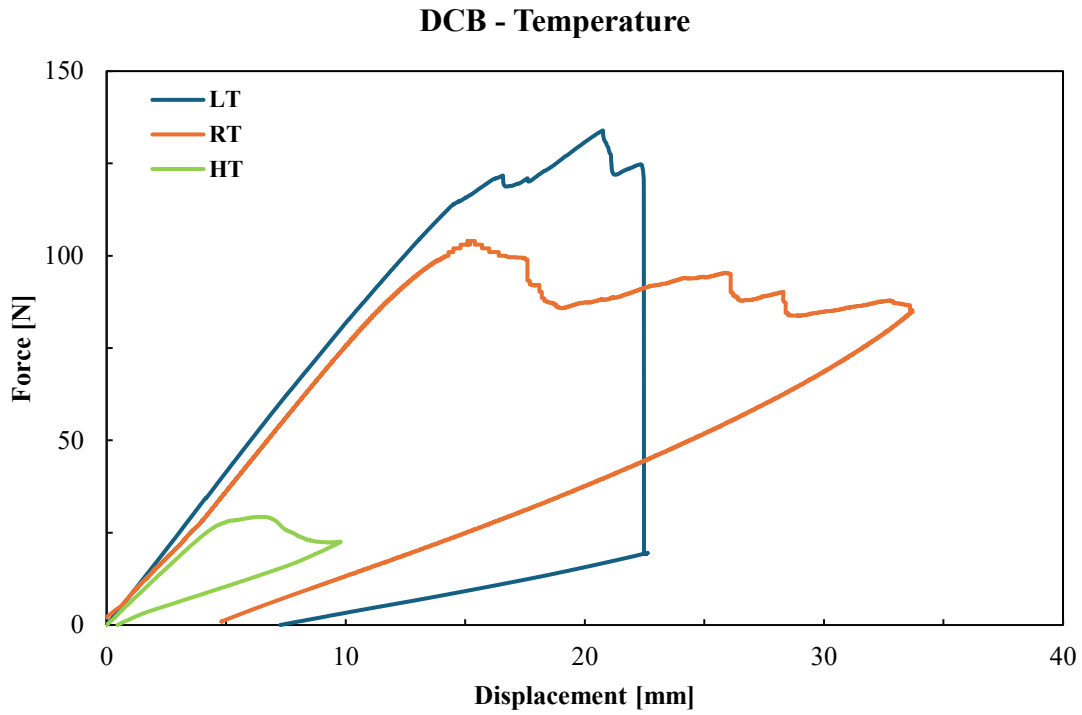

Figure 33:Results from mechanical testing of DCB: influence of the temperature

Table 11: Mean experimental results for DCB in temperature specimens

TEST	Temperature [°C]	Adhesive gap [mm]	Crack Length [mm]	Mean G_Ic [J/m^]	G_std. Dev.	Mean Peak Load [N]	Load_std. Dev.
DCB	LT (-10)	1.5	75	1099.65	510.32	109.96	51.03
	RT (23)	1.5	75	1085.46	432.88	83.5	43.28
	HT (85)	1.5	75	108.1	18.9	21.62	1.89

6.3.2 SLJ results

Force-Displacement results from SLJ test are reported in Figure 34 where only one most representative sample results for each series are shown to support the direct comparison of the different conditions. Between samples, the coefficient of variations of mean values is less than 10%. Force–displacement curves from SLJ tests at LT, RT and HT demonstrate a marked and progressive decrease in joint performance with increasing temperature. The LT specimen displays an initial linear region up to approximately 750 N, followed by a pronounced increase in stiffness until sudden adherend failure at a peak load exceeding 4500 N, suggestive of brittle fracture characteristics. RT specimens show a more gradual force–displacement profile, with an almost linear increase up to 1750 N and subsequent ductile behavior preceding peak load and ultimate failure at roughly 3300 N. The HT specimen exhibits low initial stiffness (approximately 80 N), followed by a gentle linear ascent, culminating in a markedly lower peak force around 1000 N and a distinctly ductile failure mode.

Correspondingly, the mean apparent shear strength declines sharply from 11.8 MPa at LT to 8.6 MPa at RT, then drops to just 2.7 MPa under HT conditions, reflecting both the reduced load capacity and increased ductility at elevated temperature. These results clearly show that rising temperatures induce substantial losses in stiffness, strength and overall mechanical integrity of polyurethane-bonded joints, while also altering the nature of joint failure from brittle to ductile. Means and standard deviations values for shear stress and peak force are shown in Table 12.

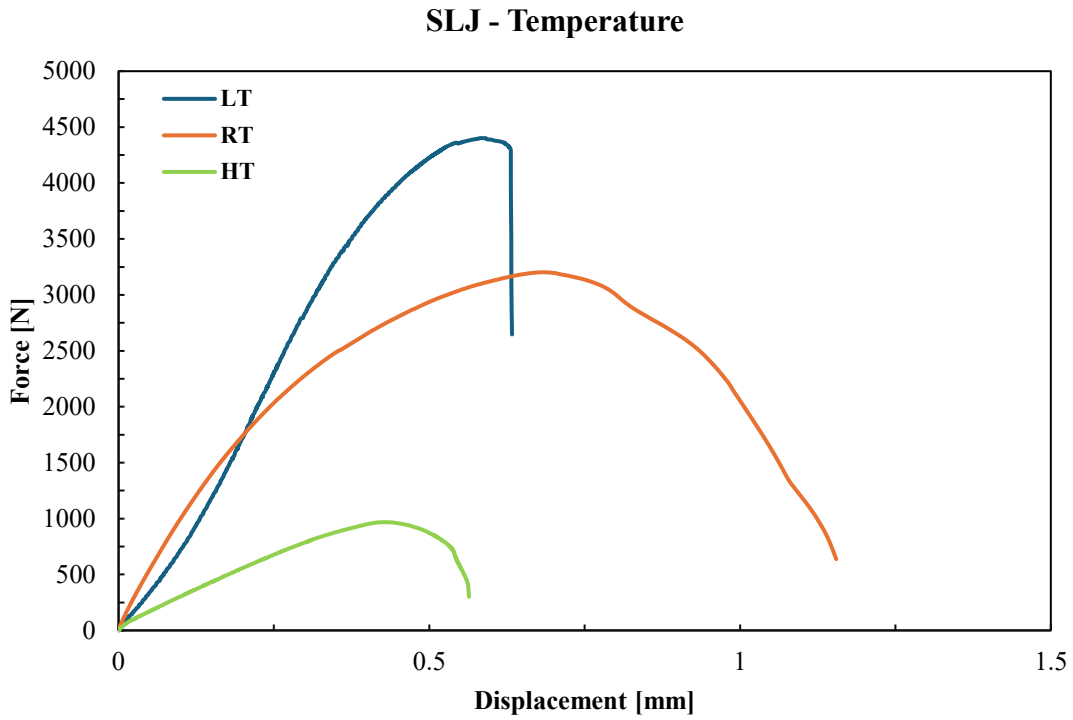

Figure 34:Results from mechanical testing of SLJ: influence of the temperature

Table 12: Mean experimental results for SLJ in temperature specimens

TEST	Temperature [°C]	Bonded Area [mm^2]	Adhesive gap [mm]	Mean Shear Stress [Mpa]	Shear_std. Dev.	Mean Peak Load [N]	Load_std. Dev.
SLJ	LT (-10)	25.4 x 15	1.5	11.83	0.56	4507.23	213.36
	RT (23)	25.4 x 15	1.5	8.6	0.73	3276.6	278.13
	HT (85)	25.4 x 15	1.5	2.71	0.4	1032.51	152.4

6.4 Fracture Surfaces

Detailed examination of fracture surfaces from both DCB and SLJ specimens revealed a pronounced temperature dependency in failure modes. At LT, failure consistently occurred within the SMC substrate via light-fiber tear, indicating that, under these conditions, the substrate's interlaminar strength becomes the limiting factor. This is attributable to the adhesive and interface strength surpassing that of the substrate, a phenomenon particularly evident with plasma-treated bonds at sub-ambient temperatures.

At both RT and HT, the locus of failure shifted to the adhesive region. Careful inspection of the fractured interfaces identified a persistent thin veil of grey adhesive residue on the substrate, signifying a pseudo-cohesive failure confined to the first few microns of the adhesive close to the substrate. Such failure is classified as adhesive but suggests a marginally suboptimal interface, possibly due to specific plasma activation parameters or local curing variations.

This subtle, repeatable observation at operational temperatures points to the importance of surface treatment protocol optimization for reliable joint performance across a broad service window. A comparison of both SLJ shear strength and DCB Mode I fracture energy for this temperature range investigation is presented in Figure 35. Failure surfaces of most representative specimens are showed in Figure 36.

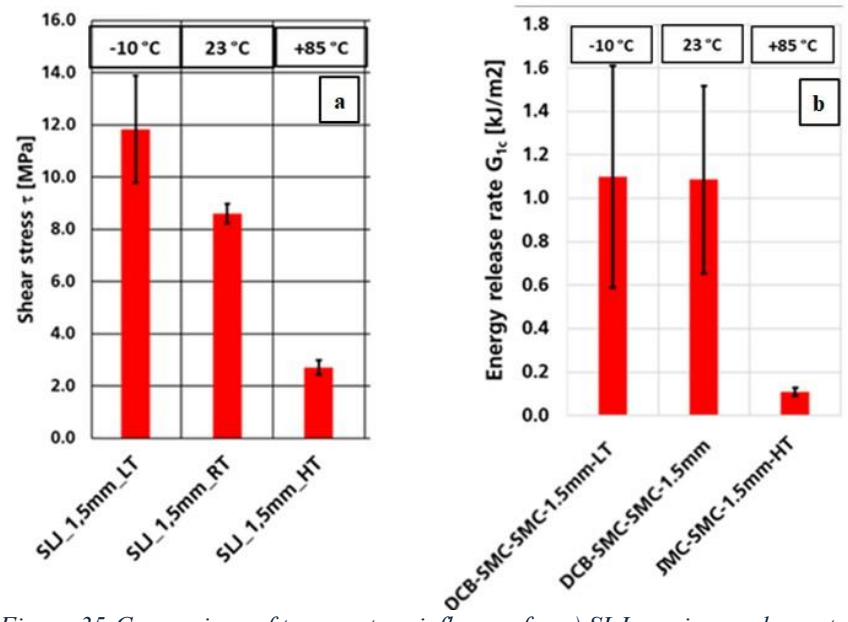

Figure 35:Comparison of temperature influence for a) SLJ specimens shear stress and b) DCB specimens fracture energy

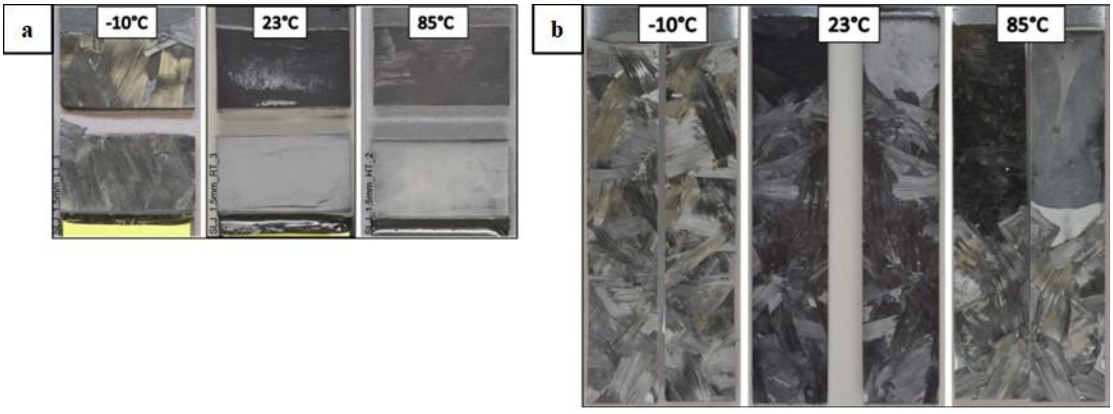

Figure 36:Fracture surfaces from temperature influence analysis: a) SLJ specimens and b) DCB specimens

6.5 Conclusion

The experimental findings clearly highlight the marked sensitivity of polyurethane–SMC joints to temperature changes. In DCB mode I tests, the fracture toughness remained stable between LT and RT but collapsed by approximately 90% at HT, reflecting severe thermal softening of the adhesive network. SLJ tests similarly demonstrated that apparent shear strength and overall load capacity decline as temperatures rise, with the adhesive transitioning from a ductile, high-strength performance at LT (12 MPa, 4500 N) to a much weaker and more ductile state at HT (2.7 MPa, 1000 N). The transition in failure locus from the substrate at subzero temperatures toward the adhesive at higher temperatures confirms that elevated thermal exposure promotes adhesive-dominated debonding and accelerates softening mechanisms, further verified by the recurring presence of cohesive-like adhesive residues at the interface.

Overall, these results emphasize that, while polyurethane adhesives may deliver robust mechanical performance at low and room temperatures, their reliability under elevated temperatures is substantially reduced. Thus, careful consideration of operational temperature range, surface preparation and possible minor interface weaknesses is imperative in the qualification and design of bonded SMC assemblies for critical applications.

Chapter 7: Adhesive properties comparison between alternative adherend materials: Glass-SMC bonded joints

7.1 Introduction

The mechanical response of adhesively bonded joints is not governed solely by the adhesive properties but emerges from the interaction between adhesive behavior and adherend stiffness, strength and damage tolerance. Despite this, adhesive characterization and cohesive modeling approaches often assume that calibrated adhesive properties are transferable across different adherend systems, neglecting the influence of substrate compliance and failure modes.

This chapter investigates the effect of adherend material by directly comparing bonded joints manufactured with carbon fiber–reinforced and glass fiber–reinforced SMC. By maintaining identical joint geometry, adhesive thickness and surface preparation, the analysis isolates the contribution of adherend mechanical properties to the observed joint response.

Beyond a comparative assessment of joint performance, this study aims to provide physical insight into how adherend stiffness and substrate damage mechanisms affect apparent fracture energy, load-bearing capacity and failure modes. The results are discussed not only in terms of material selection for structural applications, but also with respect to their implications for adhesive modeling assumptions and the transferability of cohesive zone material cards across different composite adherends.

7.2 Materials and methods

7.2.1 Specimen definition

Specimens for both DCB and SLJ tests for this phase follow the same dimensions as described in Section 3.4.1 and Section 3.4.3 (bonded area per SLJ, pre-crack length, adhesive thickness, etc.). To investigate the behavior of the adhesives also with different adherend system, the same specimens' dimensions and surface plasma preparations as the carbon-SMC specimens were employed. Mechanical test results are presented and discussed in Section 7.3 while fractographic evidence are presented in Section 7.4.

7.2.2 Mechanical Testing

The tests were carried out on a ZwickRoell Z010 Universal testing machine with a 10 kN load cell equipped with a fixture that connects to the specimen, ensuring correct alignment to minimize any bending moments.

All specimens were pre-loaded at 5 N and the test was conducted at a constant crosshead speed of 2 mm/min for DCB until total failure of the specimen, not performing the unloading part of the test described in the standard and for SLJ the test was conducted at 1.27 mm/min until failure.

For this phase samples with a 1.5 mm adhesive thickness and plasma surface treatment were tested for a total of 20 specimens, takin the plasma treated Carbon-SMC to Carbon-SMC data results from previous experiments (See Section 5.3):

- N° 10 specimens for DCB plasma treated specimens with Glass-SMC to Glass-SMC bonded adherends.
- N° 10 specimens for SLJ plasma treated specimens with Glass-SMC to Glass-SMC bonded adherends.

7.3 Mechanical tests Results

7.3.1 DCB results

Force-Displacement results from DCB test are reported in Figure 37 where only one most representative sample results for each series are shown to support the direct comparison of the different conditions. Between samples, the coefficient of variations of mean values is greater than 10%. Force–displacement curves from DCB tests comparing Carbon-SMC and Glass-SMC adherends reveal significant differences in joint behavior and mechanical performance. For Carbon-SMC specimens, an initial linear region is observed up to approximately 70 N, followed by an increase in stiffness leading to a peak load of about 100 N and an extended plateau, indicative of stable crack propagation and enhanced energy absorption. In contrast, the Glass-SMC specimens exhibit a shorter initial linear segment, plateauing at only 10 N and then a lower stiffness region leading to failure at around 45 N, with the curve revealing a more abrupt and brittle response.

Quantitatively, the mean fracture energy for Glass-SMC joints is 262 J/m², substantially lower than the 1085 J/m² measured for Carbon-SMC, confirming the more fragile behavior of glass-reinforced specimens. The associated standard deviations reflect the intrinsic variability of these material systems, but the trend of significantly reduced strength and toughness for Glass-SMC is consistent and clear. Peak load values also mirror this pattern, with Glass-SMC specimens reaching less than half the maximum load achieved by Carbon-SMC joints. These data demonstrate the marked influence of adherend and /or adhesive material selection on the effectiveness and failure mode of adhesively bonded SMC joints. Means and standard deviations values for fracture energy and peak force are showed in Table 13.

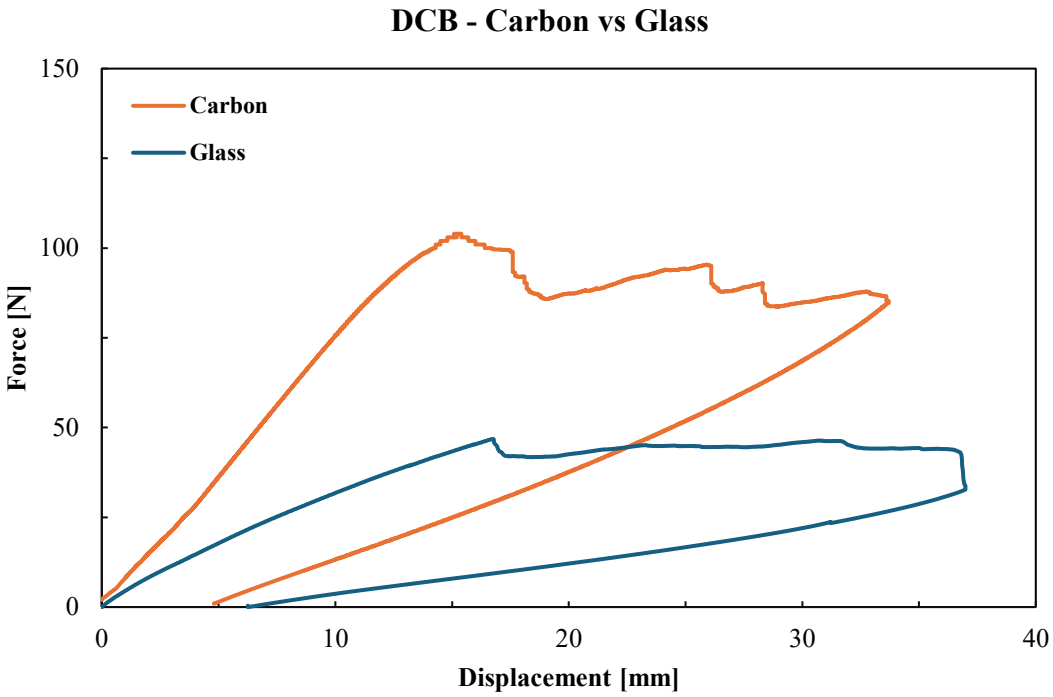

Figure 37: Results from mechanical testing of DCB: influence of different adherend material

Table 13: Mean experimental results for DCB with alternative adherend material

TEST	Adherend	Adhesive gap [mm]	Crack Length [mm]	Mean G_Ic [J/m^]	G_std. Dev.	Mean Peak Load [N]	Load_std. Dev.
DCB	Carbon-SMC	1.5	75	1085.46	432.88	83.5	43.28
	Glass-SMC	1.5	75	262	143	37.88	5.54

7.3.2 SLJ results

Force-Displacement results from SLJ test are reported in Figure 38 where only one most representative sample results for each series are shown to support the direct comparison of the different conditions. Between samples, the coefficient of variations of mean values is less than 10%. Force–displacement curves from SLJ tests with Carbon-SMC and Glass-SMC adherends reveal distinct differences in joint mechanical response and strength. The Carbon-SMC specimens exhibit an initial linear segment up to approximately 1500 N, followed by a clear ductile plateau and peak load around 3200 N, indicative of substantial energy absorption and plastic deformation before failure. In comparison, the Glass-SMC specimens present a less pronounced linear region, peaking at about 400 N, then display a progressive reduction in stiffness and fail at a much lower force (~1500 N), evidencing a more limited ductile region and earlier failure.

Quantitatively, the mean shear strength for Glass-SMC joints was only 5.2 MPa, significantly lower than the 8.6 MPa recorded for Carbon-SMC. Mean peak load for Glass-SMC reached 1570 N, less than half of Carbon-SMC's 3277 N. Standard deviations remain under 10%, demonstrating test consistency. Collectively, these findings confirm that the use of glass-based adherends leads to reduced joint strength and toughness in SLJ configurations, underlining the influence of adherend and adhesive composition on joint performance. Means and standard deviations values for shear stress and peak force are showed in Table 14.

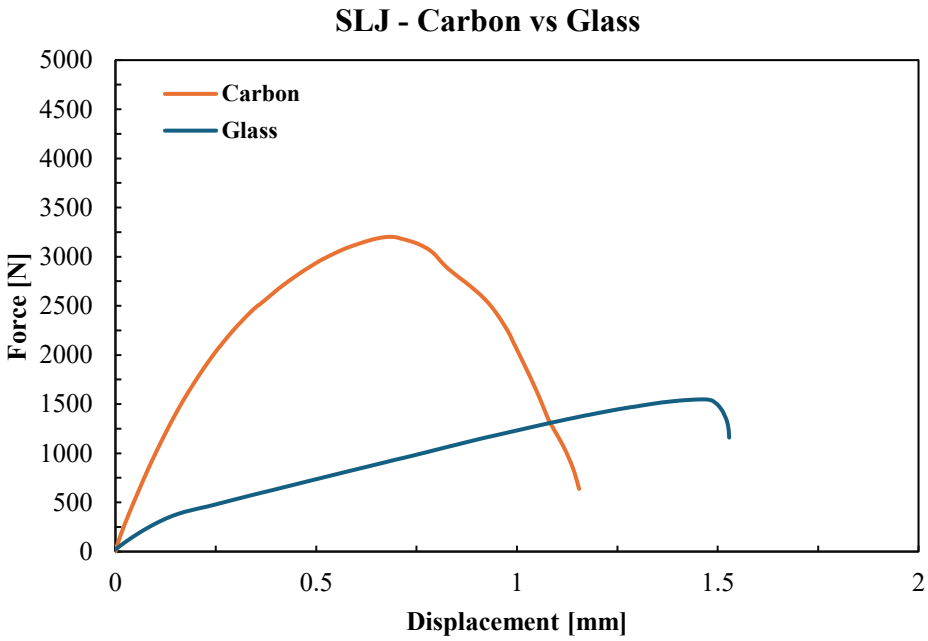

Figure 38: Results from mechanical testing of SLJ: influence of different adherend material

Table 14:Mean experimental results for SLJ with alternative adherend material

TEST	Adherend	Bonded Area [mm^2]	Adhesive gap [mm]	Mean Shear Stress [Mpa]	Shear_std. Dev.	Mean Peak Load [N]	Load_std. Dev.
SLJ	Carbon-SMC	25.4 x 15	1.5	8.6	0.73	3276.6	278.13
	Glass-SMC	25.4 x 15	1.5	5.2	0.82	1570.08	254.18

7.4 Fracture Surfaces

Microscopic examination of the fracture surfaces revealed that joint failure in Glass-SMC adherends is characterized by interfacial debonding accompanied by the removal of fine substrate particles from the SMC material. This composite tearing at the interface highlights a critical weakness: while chemical adhesion between the polyurethane adhesive and the glass-fiber substrate may be sufficient, the poor interlaminar and surface strength of Glass-SMC limits the overall load-bearing capability of the joint. In contrast, Carbon-SMC adherends consistently demonstrated higher resistance to interfacial and substrate failure, with crack propagation largely contained within the adhesive or along the interface and minimal substrate damage.

This distinct behavior underscores the role of substrate composition and microstructural integrity in governing not only joint strength but also the locus and morphology of fracture under mechanical load.

Failure surfaces of most representative specimens are showed in Figure 39.

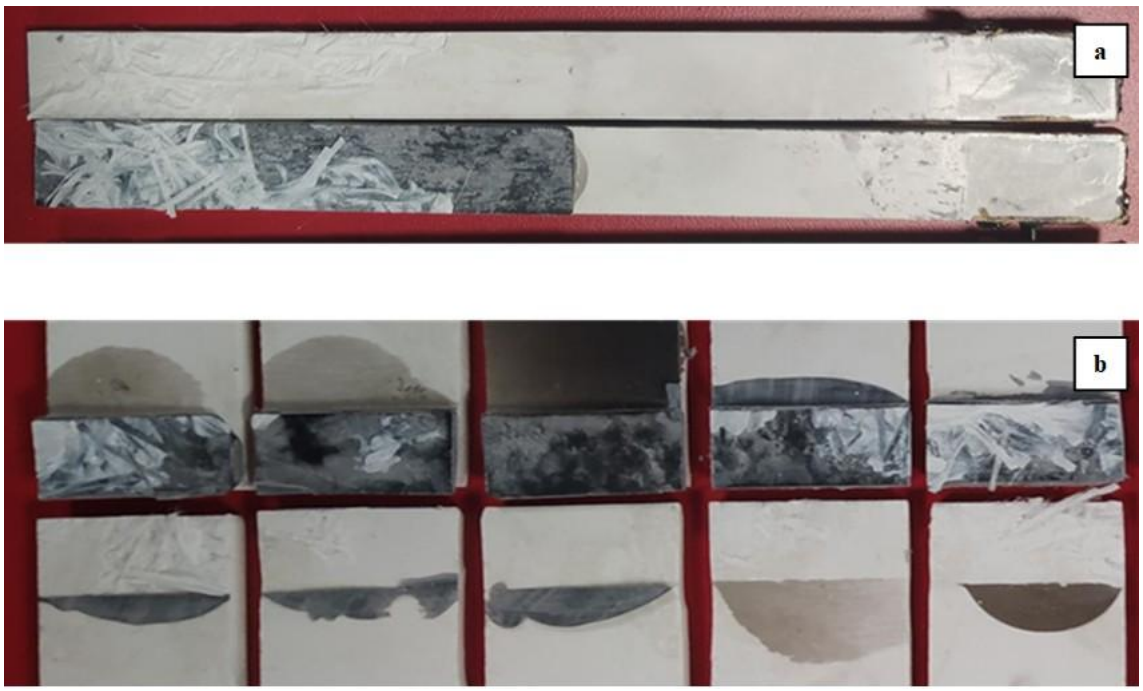

Figure 39: Fracture surfaces from different adherend material analysis: a) DCB specimens and b) SLJ specimens

7.5 Conclusion

The experimental results demonstrate that the observed deterioration in joint performance when using Glass-SMC adherends is not primarily driven by changes in adhesive behavior, but by the reduced stiffness, lower interlaminar toughness, and limited surface strength of the glass-reinforced substrate.

DCB tests revealed a reduction in fracture energy to approximately 260 J/m² for Glass-SMC systems, denoting an earlier onset of substrate-related damage and reduced constraint within the adhesive layer, leading to premature crack propagation and a more brittle global response. Conversely, the higher stiffness of Carbon-SMC promotes more stable crack growth and greater energy dissipation, enabling fuller exploitation of the adhesive's ductile fracture capabilities. SLJ tests showed mean shear strength dropping to 5 MPa (less than half that achieved with Carbon-SMC) thus confirming the intrinsic limitation arising from the lower mechanical properties and interlaminar toughness of Glass-SMC.

Fractographic evidence confirms that failure in Glass-SMC joints is governed by interfacial debonding coupled with substrate tearing, indicating that the adherend becomes the limiting factor rather than the adhesive itself. In contrast, Carbon-SMC adherends maintain structural integrity at the interface, resulting in failure modes more representative of the intrinsic adhesive performance.

From a modeling perspective, these findings highlight the key limitation in assuming direct transferability of adhesive material cards across different adherend systems, as also known from literature. Apparent fracture energies and strength parameters obtained from joints with compliant or damage-prone substrates may reflect adherend-controlled failure rather than true adhesive properties. Consequently, cohesive zone models calibrated on Carbon-SMC joints cannot be blindly applied to Glass-SMC systems without accounting for substrate stiffness and failure mechanisms. These results emphasize the need for adherend-aware adhesive characterization strategies when developing predictive and transferable FE models for bonded composite structures.

Chapter 8: Adhesive properties comparison between alternative adherend materials: Aluminum - SMC bonded joints

8.1 Introduction

Hybrid adhesive joints, combining composite and metal adherends, are increasingly relevant for advanced multi-material structures and engineering applications. In this section, DCB tests on Aluminum–Carbon-SMC specimens and SLJ tests on Aluminum–Aluminum joints are analyzed alongside baseline SMC configurations. DCB hybrid joints Aluminum-SMC were selected to elucidate fracture mechanics and interfacial behavior at the technically important metal–composite boundary, as requested by the industrial sponsor (same reason glass hybrid components were not tested) and driven by the need to simulate real-world crash or durability scenarios. For SLJ, the Aluminum–Aluminum configuration served as a reference case, both for benchmarking adhesive bulk strength on a high-integrity substrate and for drawing direct performance comparisons with SMC joints, where substrate failure mechanisms are limiting.

8.2 Materials and methods

8.2.1 Specimen definition

Specimens for both DCB and SLJ tests for this phase follow the same dimensions as described in Section 3.4.1 and Section 3.4.3. They will be kept the same for the subsequent mechanical testing specimens. Aluminum adherends for both DCB and SLJ specimens were e-coated treated for protection and surface preparation of the aluminum surface, leaving the cleaning and degreasing processes the only preparations prior to bonding. Mechanical test results are presented and discussed in Section 8.3 while fractographic evidence are presented in Section 8.4.

8.2.2 Mechanical Testing

The tests were carried out on a ZwickRoell Z010 Universal testing machine with a 10 kN load cell equipped with a fixture that connects to the specimen, ensuring correct alignment to minimize any bending moments. All specimens were pre-loaded at 5 N and the test was conducted at a constant crosshead speed of 2 mm/min for DCB until total failure of the specimen, not performing the unloading part of the test described in the standard and for SLJ the test was conducted at 1.27 mm/min until failure.

For this phase samples were tested for a total of 20 specimens, takin the plasma treated Carbon-SMC to Carbon-SMC data results from previous experiments as base data for comparison (See Section 5.3):

- N° 10 specimens for DCB plasma treated SMC to E-coated Aluminum with adhesive thickness of 2 mm.
- N° 10 specimens for SLJ E-coated Aluminum to E-coated Aluminum with adhesive thickness of 2 mm.

8.3 Mechanical testing Results

8.3.1 DCB results

Force-Displacement results from DCB test are reported in Figure 40 where only one most representative sample results for each series are shown to support the direct comparison of the different conditions. Force–displacement results from DCB tests conducted on SMC and Aluminum–SMC hybrid joints reveal distinct mechanical responses attributable to the adherend configuration. The SMC specimens exhibit a clear linear region up to approximately 15 N, with a peak load around 100 N and the expected plateau indicating ductile crack propagation. In hybrid Aluminum–SMC specimens, the initial linear response is observed only up to about 5 N, followed by a decrease in stiffness leading to damage initiation at roughly 45 N, about half the stiffness of the fully SMC joint. The mean fracture energy for Aluminum–SMC is approximately 985 J/m², marginally lower than the 1085 J/m² for SMC only. Coefficient of variation in both configurations exceeds 10%, indicating substantial variability, likely arising from differences in adherend surface state and local bonding conditions. Means and standard deviations values for fracture energy and peak force are showed in Table 15.

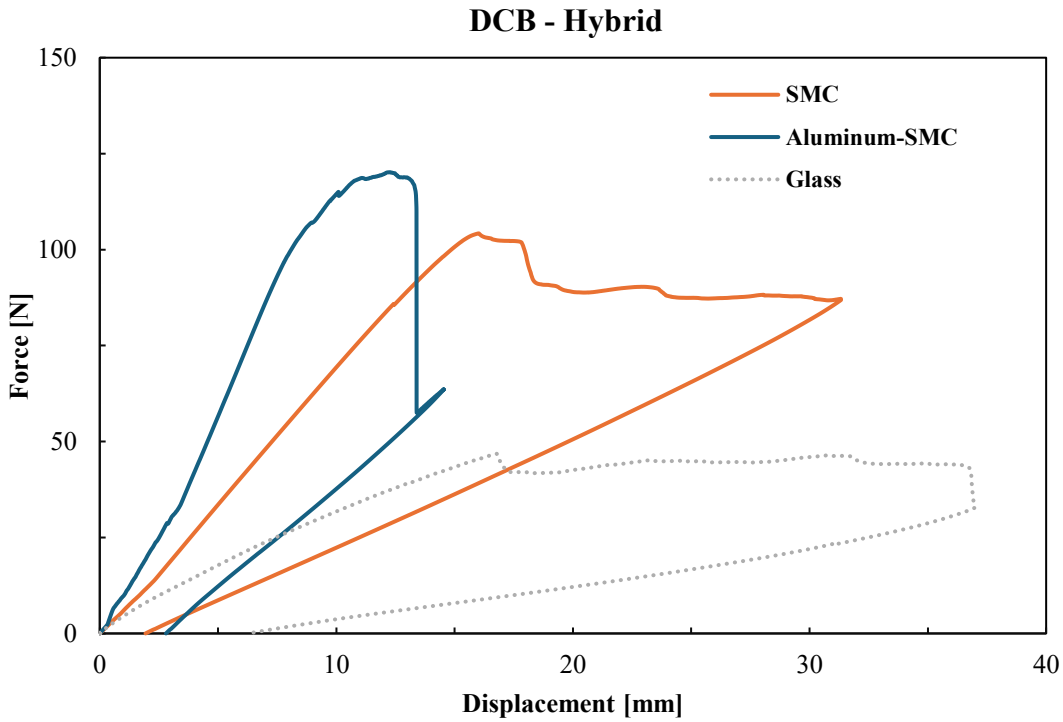

Figure 40: Results from mechanical testing of DCB: influence of the aluminum adherend material (Glass fiber curve was added for comparison)

Table 15: Mean experimental results for comparison of DCB SMC hybrid specimens

TEST	Adherend	Adhesive gap [mm]	Crack Length [mm]	Mean G_Ic [J/m^]	G_std. Dev.	Mean Peak Load [N]	Load_std. Dev.
DCB	Carbon-SMC	1.5	75	1085.46	432.88	83.5	43.28
	Aluminum - C-SMC	1.5	75	985.47	251.22	98.547	25.122

8.3.2 SLJ results

Force-Displacement results from SLJ test are reported in Figure 41 where only one most representative sample results for each series are shown to support the direct comparison of the different conditions. Between samples, the coefficient of variations of mean values is less than 10%. Force–displacement curves from SLJ tests comparing Carbon-SMC and Aluminum–Aluminum adherends present distinctly different joint behaviors. The Carbon-SMC joints display classic ductile response, with a gradual increase up to a peak load near 2700 N and sustained energy absorption before failure. In contrast, the Aluminum–Aluminum joints demonstrate an initial linear segment up to roughly 300 N, followed by a rapid increase to a peak force approaching 3200 N. The characteristic linear rise and sharp maximum are typical of SLJ tests with high-strength metallic substrates.

Mean shear strength for the Aluminum–Aluminum joints reach 8.6 MPa, exceeding the 7.1 MPa observed for the Carbon-SMC configuration. Peak loads and measured values for both cases exhibit coefficients of variation below 10%, confirming experimental reproducibility. The failure profile of Aluminum–Aluminum joints represent the true shear strength of the bulk adhesive under ideal substrate conditions, limiting substrate failure mechanisms such as fiber tear or interlaminar debonding, which were observed in plasma-treated SMC joints. These results highlight the influence of substrate mechanical properties on the measured strength and failure characteristics of adhesively bonded joints. Means and standard deviations values for shear stress and peak force are showed in Table 16.

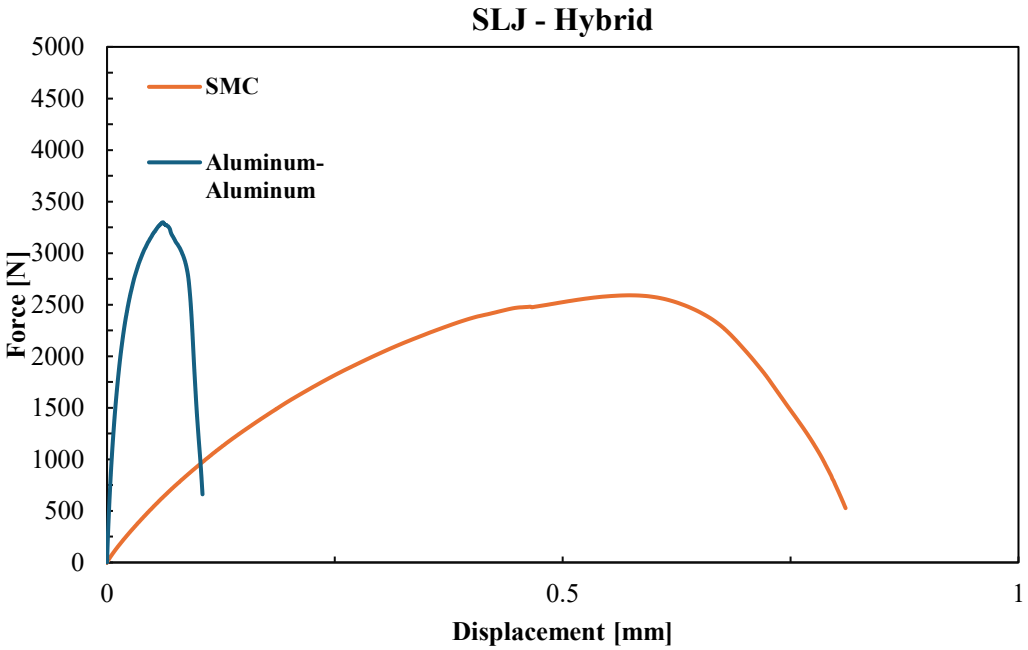

Figure 41: Results from mechanical testing of SLJ: influence of the aluminum adherend material

Table 16:Mean experimental results for comparison of SLJ SMC hybrid specimens

TEST	Adherend	Bonded Area [mm^2]	Adhesive gap [mm]	Mean Shear Stress [Mpa]	Shear_std. Dev.	Mean Peak Load [N]	Load_std. Dev.
SLJ	Carbon-SMC	25.4 x 15	2	7.05	0.55	2686.05	209.55
	Aluminum Aluminum	25.4 x 15	2	8.57	0.98	3265.17	373.38

8.4 Fracture Surfaces

Detailed inspection of the fracture surfaces revealed mode-dependent failure in hybrid joints. For DCB specimens, both configurations showed a consistent fracture starting with an almost adhesive debonding at the SMC–adhesive interface, leaving behind a very thin adhesive layer and ending with a crack propagation through the adherend SMC material.

SLJ tests on aluminum–aluminum joints revealed a fully cohesive fracture path, with separation occurring within the bulk adhesive layer itself while non-hybrid SMC configurations showed also a cohesive failure mode, although characterized by a small patch and a thin veil of adhesive material left on the interface.

This stark contrast highlights the influence of substrate type and interfacial chemistry: the SMC–adhesive joint is limited by the weaker interfacial region, while the high-strength aluminum–aluminum joint allows expression of the intrinsic cohesive toughness of the adhesive. Failure surfaces of most representative specimens are showed in Figure 42.

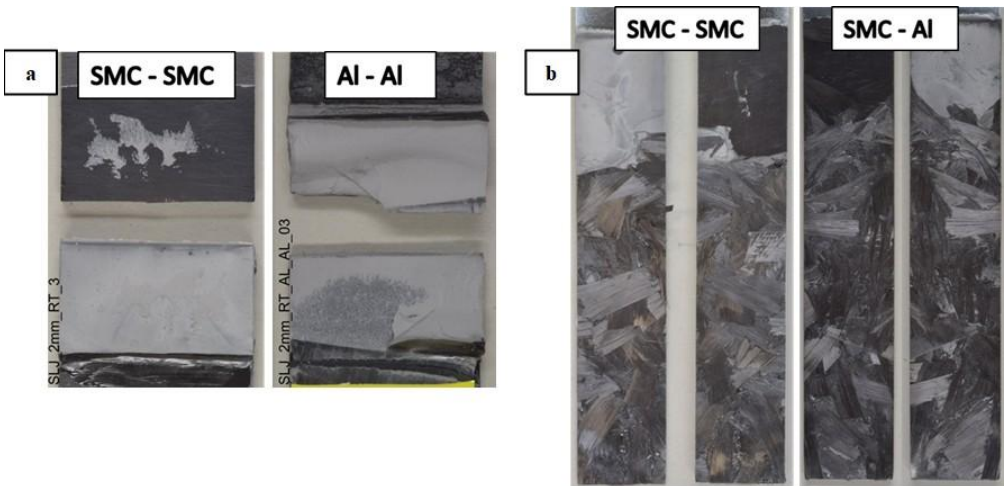

Figure 42: Fracture surfaces from adherend material influence analysis: a) SLJ specimens SMC to SMC (left) and aluminum-aluminum (right) and b) DCB specimens SMC to SMC (left) and aluminum-SMC (right)

8.5 Conclusion

Hybrid adhesive joints comprising carbon–SMC and aluminum adherends demonstrate intermediate mechanical performance between purely composite and purely metallic configurations. DCB tests on hybrid specimens yielded roughly half the stiffness of all–SMC joints but reached a mean fracture energy of about 1000 J/m², accurately representing adhesive behavior at a technically relevant interface. In SLJ configurations, joints between aluminum adherends attained a mean shear strength of 8.6 MPa, which reflects the full development of the adhesive's intrinsic properties when paired with a robust, non-failing metallic substrate.

Fractographic evidence corroborated the distinction between failure modes: adhesive debonding dominated at the SMC interface, while cohesive fracture characterized aluminum–aluminum joints, emphasizing the differing interfacial and bulk contributions to joint strength.

Chapter 9: Mixed mode and fatigue analysis of adhesively bonded joints

9.1 Introduction

This phase of this experimental campaign was dedicated to evaluating joint behavior under complex loading conditions, integrating both mixed-mode (Mode I + Mode II) and cyclic fatigue tests. Mixed-mode testing was specifically chosen to simultaneously activate opening and shear failure mechanisms within a single specimen configuration, overcoming the limitations encountered during previous ENF tests and eliminating the need for separate characterizations. This approach allowed for the forced induction of Mode II shear damage through a controlled Mode I force, providing a more representative simulation of realistic multiaxial service conditions.

Fatigue testing further extended the analysis, yielding data critical for the characterization and calibration of simulation tools, as well as for the long-term reliability assessment of adhesive joints. By replicating service-like cyclic loading, these experiments enabled direct observation of crack initiation and propagation at the adhesive–SMC interface (completing the failure modes encountered earlier) and contributed essential insight into the material's durability under operational stresses. Advanced measurement techniques, including Digital Image Correlation, were employed throughout to map strain evolution and capture the progression of damage with high spatial and temporal resolution.

Collectively, these advanced experimental protocols bridge fundamental adhesive science with practical engineering requirements, supplying a comprehensive dataset for future predictive modeling and robust design of bonded assemblies.

9.2 Specimen definition

Specimens for both DCB and SLJ tests for this phase follow the same dimensions as described in Section 3.4.1and Section 3.4.3. They will be kept the same for the subsequent mechanical testing specimens. Adherend manufacturing follows the same press molding and cutting procedure as the Carbon SMC; the shape and dimensions of both the following specimens type are fundamentally the same as the DCB specimens so: total length L = 200 mm, length from specimen tip prior to crack e = 25 mm, pre-crack length a = 75 mm, adherend thickness h = 4.1 mm, width b = 20 and adhesive gap 1.5 mm. Mechanical test results are presented and discussed in Section 9.4 while fractographic evidence are presented in Section 9.5.

9.3 Mechanical Testing

For this phase were tested plasma treated SMC to SMC bonded samples with a 1.5 mm adhesive thickness for a total of 20 manufactured specimens:

- Only n° 7 specimens out of 10 for DCB mixed-mode loading conditions were analyzed due to early flexural damage and hinge debonding on the remaining specimen, invalidating the characterization analysis.
- Only n° 6 specimens out of 10 for DCB fatigue cycling were analyzed due to hinge debonding and short time-scheduling to be able to continue the campaign and observe the remaining specimen's behavior at high number of cycles.

9.3.1 Mixed Mode

The tests were carried out on a ZwickRoell Z010 Retroline machine with a 1 kN load cell. For the mixed mode test, the machine was equipped with a special fixture that ensures correct alignment and connectivity to minimize any unwanted movements. During this test, no hinges are required because the test is more like a mix between a DCB and an ENF test with both a tensile and a flexural force component.

Depending on the sample dimensions and the mixed mode of interest, the specimen can be positioned on the special fixture in a series of different configurations, enabling each one a different mix ratio of Mode I and Mode II forces. For this study, only one mix ratio was analyzed due to incompatibility between specimen and fixture dimensions; to be able to precisely explore more mix ratios both the specimen and fixture length dimensions should have been significatively longer. Specifically, a 0.4 mix ration equivalent to a 60% Mode I and a 40% Mode II was analyzed in this case. The specimens were pre-loaded at 5 N and the test was conducted at a constant crosshead speed of 2 mm/min for mixed mode until failure. Pictures of the testing phase are presented in Figure 43.

9.3.2 Fatigue cycling

The tests were carried out on Instron Universal testing machines with a 1 kN load cell. For the fatigue test, a DIC (Digital Image Correlation) camera and lights were positioned in front of the specimen to record and analyze strain data from a dotted speckle pattern and an optical camera on the other side of the specimen to record crack initiation and propagation. For fatigue specimen, the resulting parameters were width b, crack length a, force at failure Fc and relative displacement δc adopted to obtain the fracture toughness, GI. The

employed testing procedure is not an international standard like ASTM from previous tests, but rather a custom designed from TUDelft university research group based on the DCB test (See Figure 44 for reference).

The specimen is first secured and aligned to the machine fixture with the use of pins that connects to the blocks bonded on the specimen arms, then with the aid of an automated looping program, custom designed from the Instron software, the test can start with a cyclic phase that lasts for a pre-determined number of cycles; after the cycle limit is reached, a classic DCB quasi-static phase starts with a linear ramp trait of 2 mm/min until the recorded displacement reaches a fixed value called Dmax, then the test stops itself in that configuration for 4 seconds, called measurement phase, to be able to record pictures from both DIC and optical cameras; after the measurements phase has ended, the specimen starts to unload with a speed of 15 mm/min and the loop starts again with the cycling phase, then measurements phase and so on until catastrophic failure of the specimens or until the crack propagates up to 50 mm from the initial length. Pictures of the testing opening phase are presented in Figure 50.

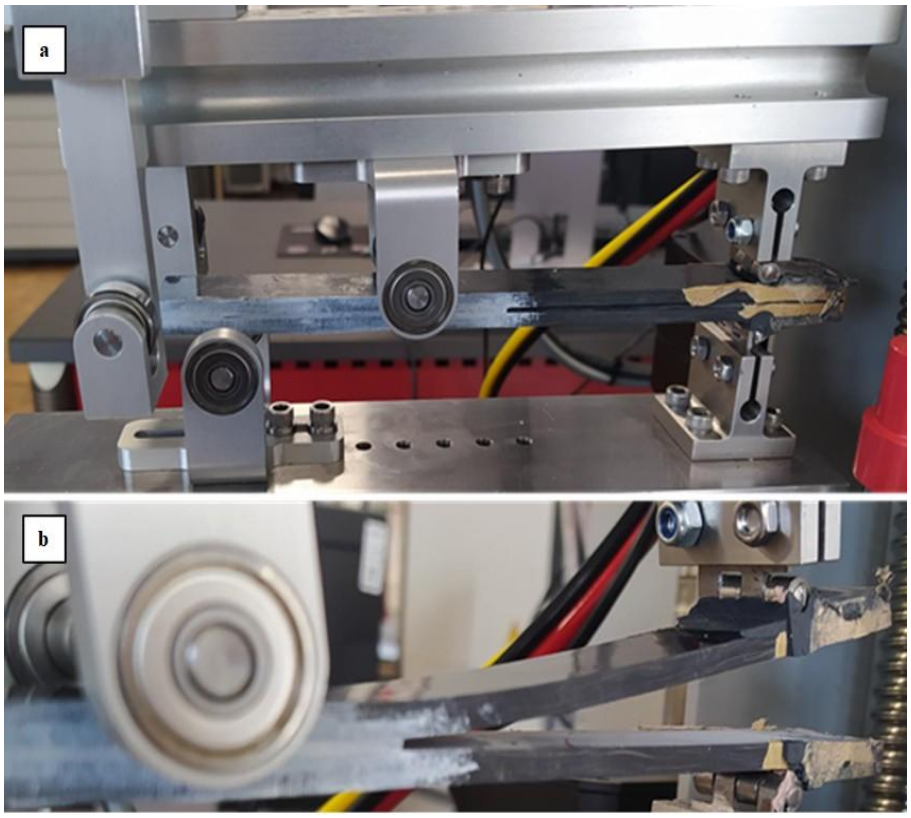

Figure 43: Mixed Mode specimens during mechanical tests: a) specimen fixed in the special fixture and b) detail of specimen during load.

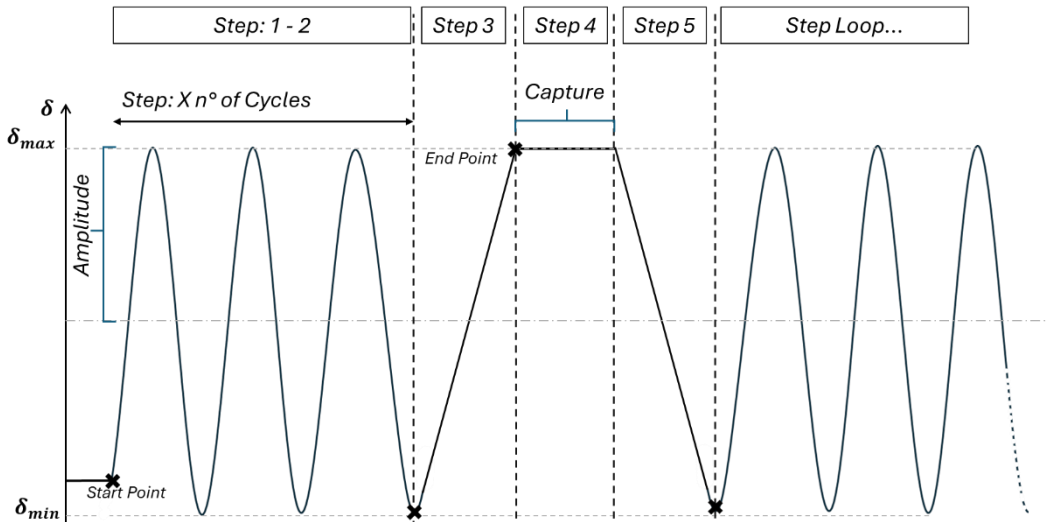

Figure 44:Details of the testing procedure for DCB fatigue specimens: from the starting position (start point), the specimen was cycled initially up to 100 cycles, then stopped to "end point" for measures and then cycled again up to the next measuring phase.

9.4 Mechanical testing Results

9.4.1 Mixed Mode

Force-Displacement results from Mixed Mode test are reported in Figure 45. Force–displacement curves from Mixed Mode DCB tests exhibit a variety of responses across individual specimens, with initial linear stiffness followed by sharp drops in force characteristic of unstable crack propagation. The coefficient of variation exceeds 10%, indicating moderate scatter likely due to differences in mode mixity and local interface conditions among specimens. Calculated mean apparent fracture energies are approximately 290 J/m² for Mode I and 220 J/m² for Mode II. The results confirm an average mode mixity close to 40%, with standard deviations for energy release rates reflecting the inherent complexity and sensitivity of mixed-mode fracture mechanics in these adhesive joints. Peak forces at 5% displacement also display variability, further emphasizing the importance of rigorous joint preparation and test method control in mixed-mode fracture testing. Means and standard deviations values for fracture energy and peak force are showed in Table 17.

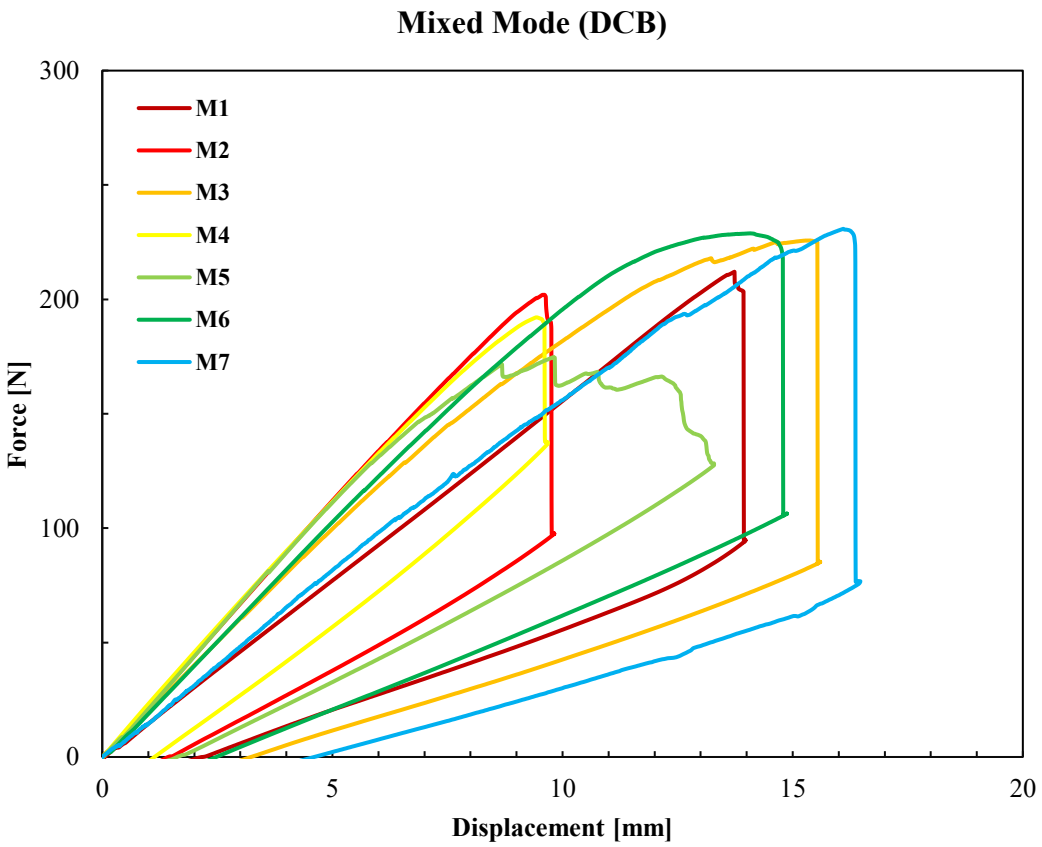

Figure 45:Results from mechanical testing of DCB Mixed Mode

Table 17: Mean experimental results from DCB mixed mode specimens

TEST	Spec. N°	Force at 5% [N]	Mode I energy G_c [J/m^2]	Mode II energy G_c [J/m^2]	Mode Mixity G_II / G [%]
Mixed Mode	1	212.10	0.57	0.47	40.77
	2	185.28	0.19	0.14	41.25
	3	148.42	0.17	0.13	39.14
	4	141.16	0.37	0.27	40.57
	5	142.11	0.33	0.24	39.18
	6	188.78	0.25	0.18	40.07
	7	189.16	0.17	0.13	40.63
	Mean Values	172.43	0.29	0.22	40.23
	Std. Dev.	26.08	0.14	0.11	0.75

9.4.2 Fatigue behaviour

Results from Fatigue test are reported in Figure 46, Figure 47, Figure 48 and Figure 49 in forms of different plots respectively: crack length vs n° of cycles, fracture energy vs n° of cycles, measured forces vs n° of cycles and finally a plot with a log(da)/log(dN) vs cyclic range valueΔG interval calculated as both peak and valley responses were taken into account to obtain $\Delta GI = \sqrt{G}max - \sqrt{G}min$, where Gmax was calculated by the load and displacement at the cyclic peak and Gmin was got using the load and displacement at the cyclic valley. The fatigue test results provide multifaceted insight into crack propagation and durability of the adhesive joints under cyclic loading.

- The "log da/dN vs ΔGI" diagram demonstrates a clear Paris-law-like behavior in the mid-range of crack growth rates across samples, with the da/dN values spanning over three log decades and sample-specific linear fits (dashed lines), confirming a regime where crack extension rate is strongly dependent on the energy release rate per cycle (ΔGI). The slopes of these fits and the vertical clustering of the curves, reflect variability in crack growth resistance and possibly differences in local joint quality among nominally identical samples.

- The "GI vs Crack Length" plots reveal a monotonically decreasing trend of fracture energy with increasing crack length for all tested specimens. Initial GI value commonly ranges from 500 J/m² up to nearly 800 J/m², but these values fall below 200 J/m² as the crack extends toward 50 mm. This decreasing trend illustrates the expected reduction in driving force for crack growth as the crack progresses deeper into the specimen and highlights intrinsic material/property gradients along the bond.

- "Crack Length vs Number of Cycles" traces indicate fast growth in the early cycles for most samples, particularly during the first 5,000–10,000 cycles, after which crack length evolution either plateaus or, for some specimens, increases rapidly again near final failure. Several samples show sudden crack jumps, while others display more stable propagation, reflecting classic fatigue crack arrest and advancement phenomena. None of the samples appear to sustain more than approximately 40,000 cycles, with failure habitually occurring before this limit.

- The relationship between "Force vs Number of Cycles" confirms that the maintained load or force at the crack tip decreases steeply after the first thousand cycles and then decays more gradually as the crack advances in length, indicating progressive degradation in joint stiffness and load transfer capability as fatigue damage accumulates.
- Optical and Digital Image Correlation (DIC) images corroborate these findings by directly visualizing localized strain accumulation at the crack tip across selected cycles and crack lengths. Red and orange zones in the contour plots indicate maximal longitudinal strain concentrations, validating the link between macroscopic crack advance and local strain-field evolution.

Overall, the fatigue behavior of these adhesive joints is characterized by:

- Rapid crack extension and significant energy dissipation within the first quarter of total life,
- Progressive decrease in fracture energy and critical ΔGI as crack grows,
- Apparent Paris regime for crack propagation rates,
- Uniform adhesive failure mode without cohesive/ substrate rupture,
- Failure thresholds consistently below 40,000 cycles under the applied loading regime.

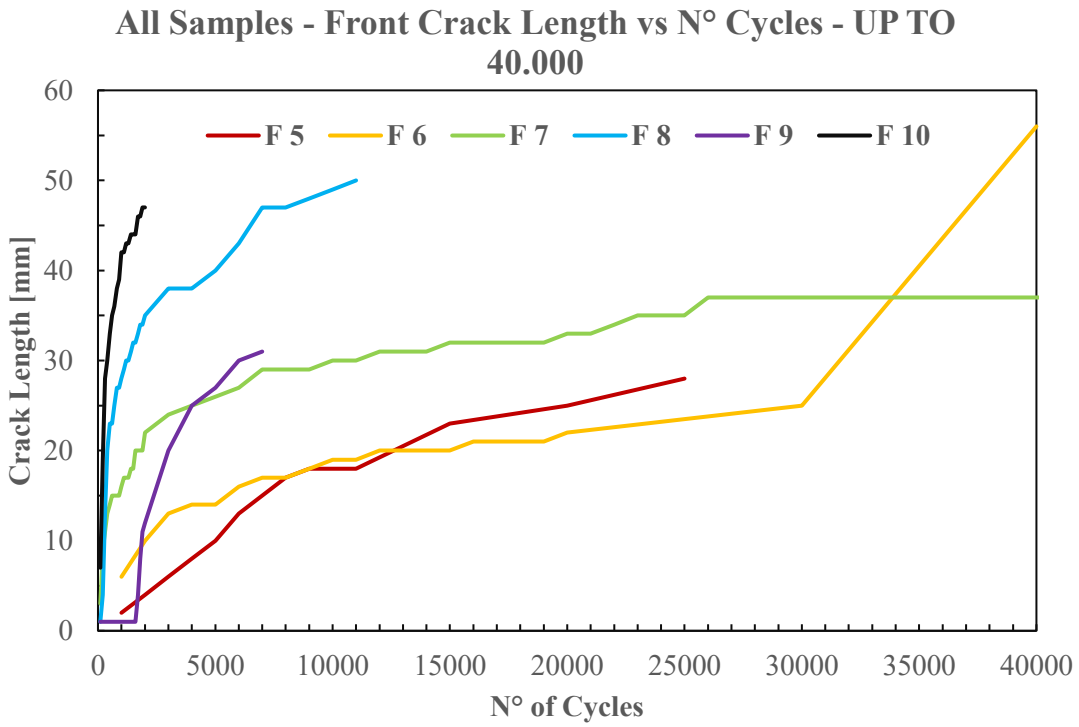

Figure 46: Results from fatigue DCB tests: crack length vs n° of cycles

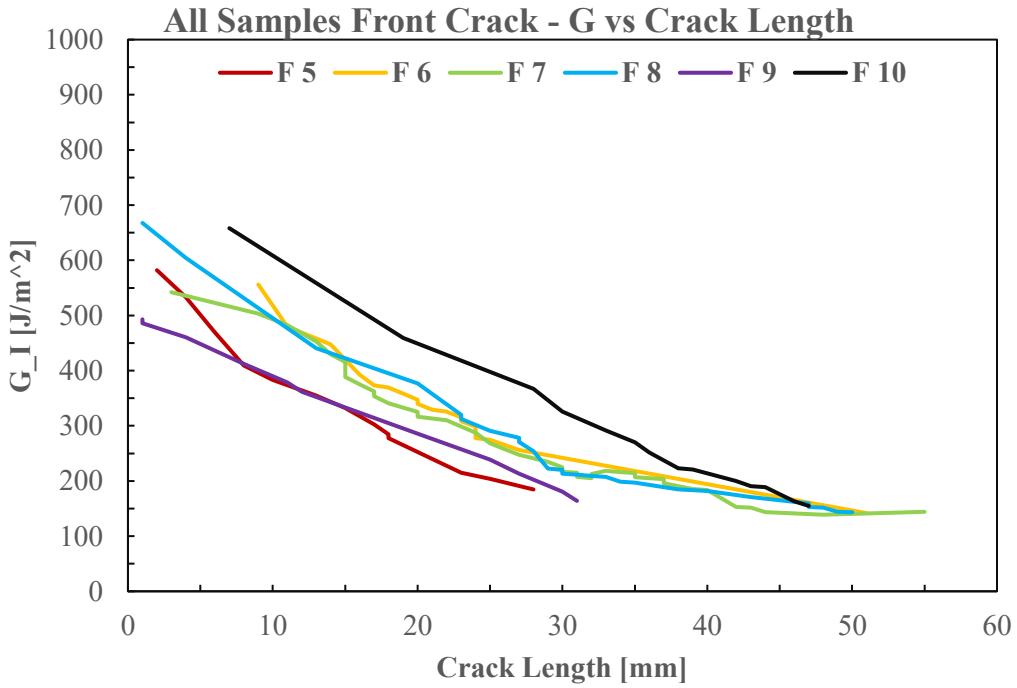

Figure 47:Results from fatigue DCB tests: fracture energy vs crack length

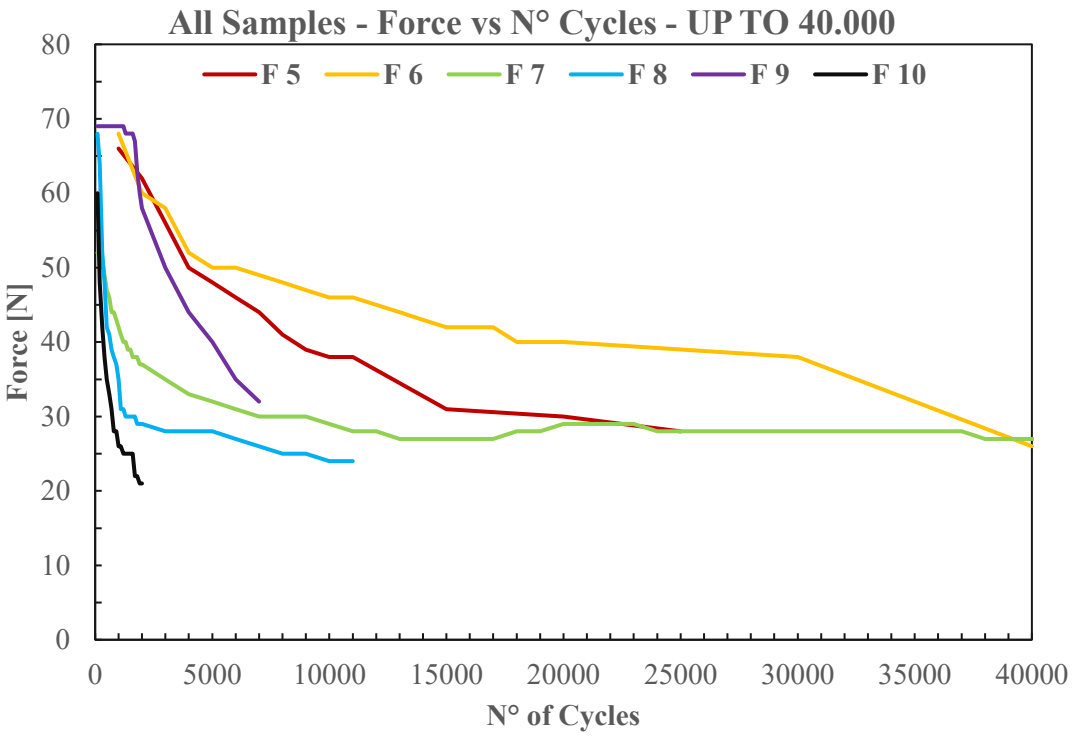

Figure 48:Results from fatigue DCB tests: force vs n° of cycles

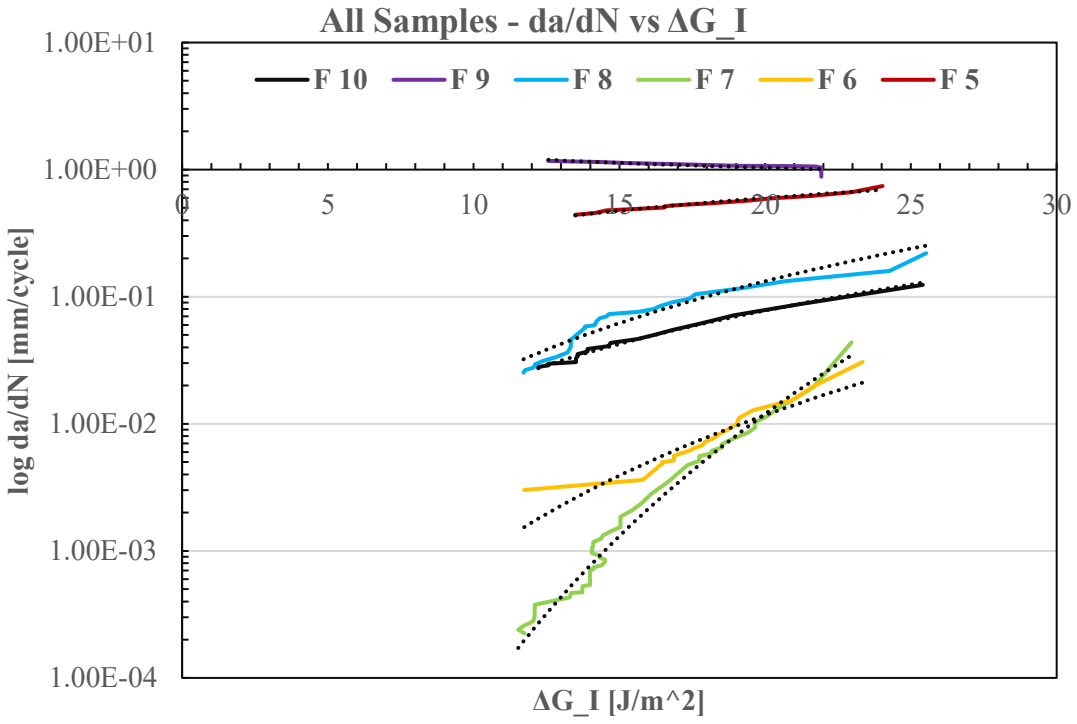

Figure 49:Results from fatigue DCB tests: log da/dN vs fracture energy

9.5 Fracture Surfaces

9.5.1 Mixed Mode

Inspection of fracture surfaces revealed that, even with the introduction of mixed-mode loading, failure was dictated by flexural rupture of the SMC substrate. The adhesive bond proved so robust that it shifted the locus of failure away from the interface and into the substrate material itself. This outcome precludes direct measurement of adhesive mixed-mode fracture energy but validates the adhesive's ability to sustain complex, multi-axial stresses without becoming the limiting factor in joint performance.

9.5.2 Fatigue behaviour

During cyclic testing, cracks consistently initiated and propagated directly at the SMC–adhesive interface. In several specimens, crack growth occurred simultaneously on both adherend interfaces due to a complex stress state at the crack front. Fracture surface examination after fatigue testing revealed consistent interfacial failure. Notably, in several specimens, crack paths switched or bifurcated between upper and lower adherend interfaces: a phenomenon indicative of multi-axial or asymmetric stress states at the crack front, as well as localized geometric or material heterogeneity. Digital Image Correlation (DIC) mapping consistently demonstrated intense and sharply localized strain fields at the crack tip, with redundant adhesive bulk remaining largely undeformed. No evidence was found for cohesive failure within the adhesive: all samples eventually failed along the pre-existing interface, consistent with the adhesive's high toughness and with a not-robust plasma treating bonding. This behavior aligns with cohesive zone model predictions, where damage accumulates within a small process zone at the interface. Failure surfaces of most representative specimens are showed in Figure 51, also in Figure 52 are shown some notable failure mechanism and relative strain deformation field visible on the crack tip. Also, an example of how crack optical measurements were taken during tests in visible in Figure 53.

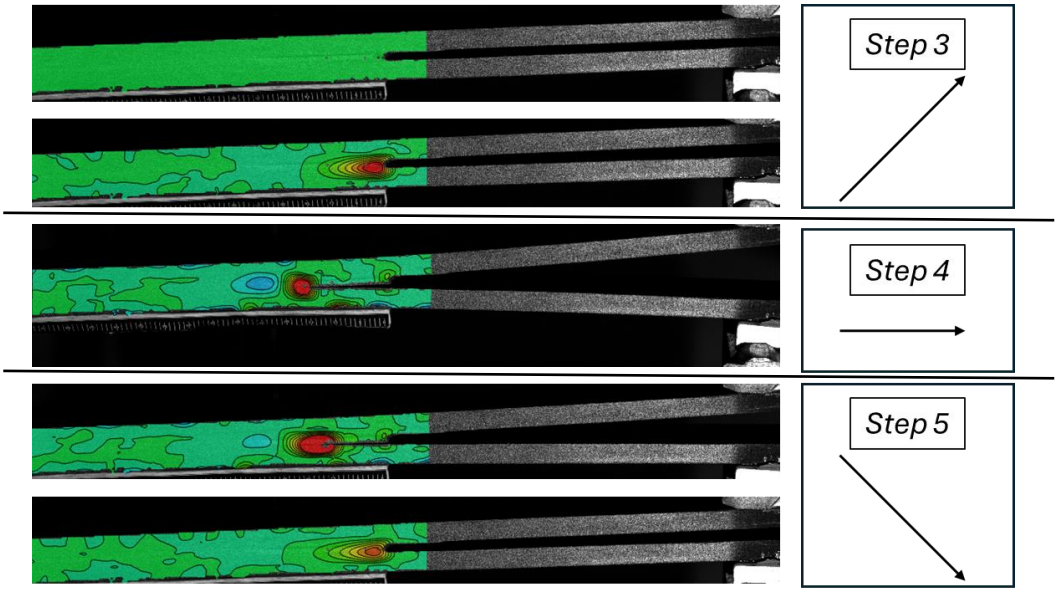

Figure 50: DCB specimen during fatigue testing steps

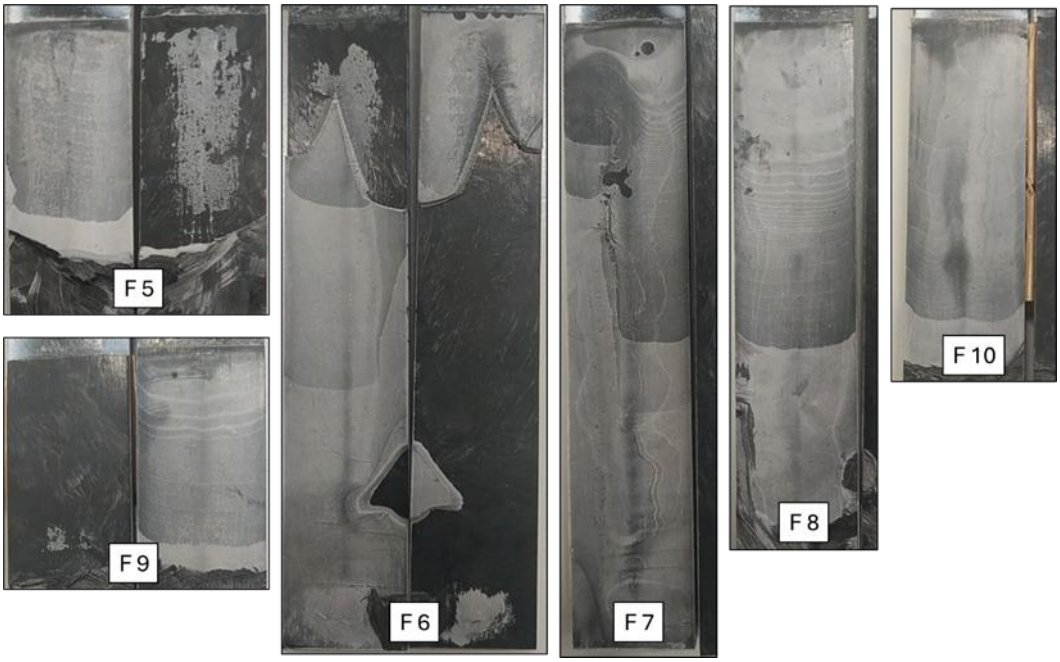

Figure 51: Fracture surfaces for DCB fatigue testing showing the crack front waves on adhesive surface

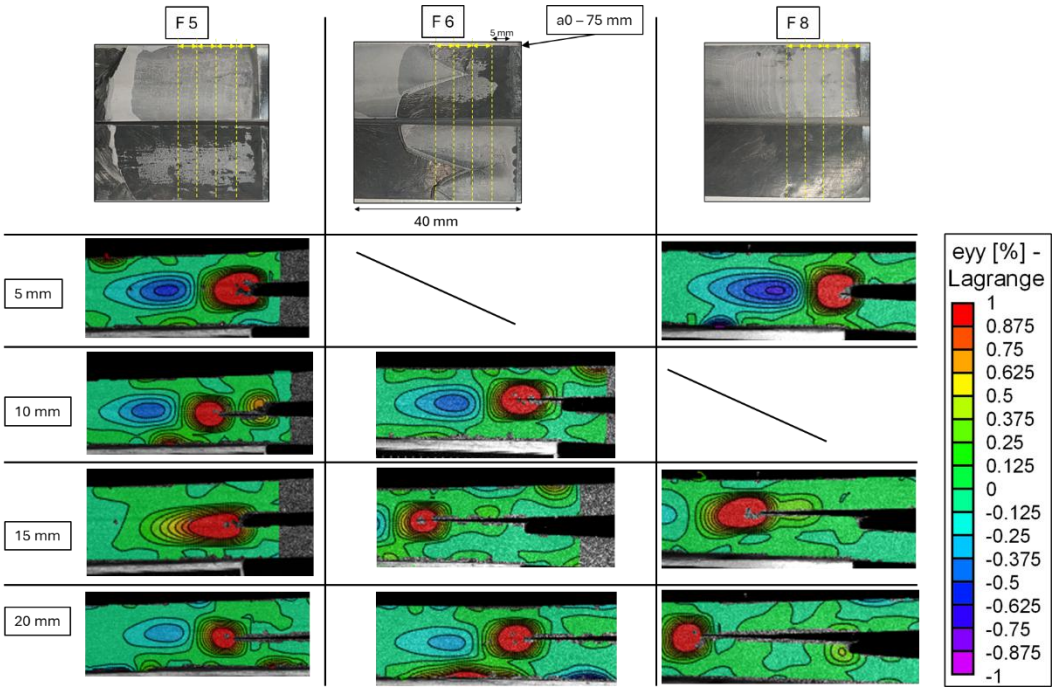

Figure 52: Behavior of "vertical - y" deformation by DIC on various key point of specimens depending on fracture surfaces

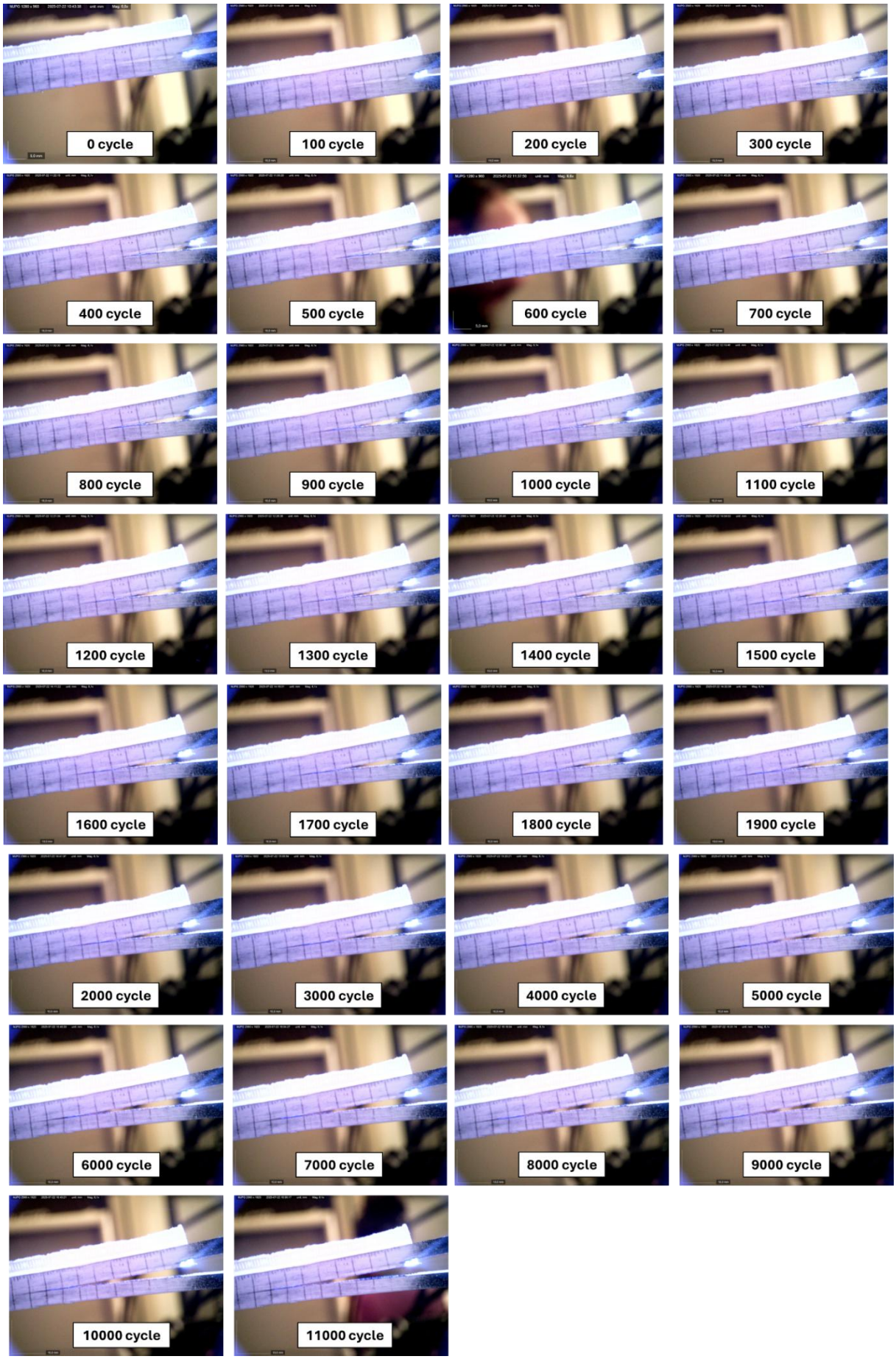

Figure 53: Crack length pictures from the back of the specimen to measure crack advancement during test

9.6 Conclusion

The fatigue testing of SMC–adhesive joints under cyclic loading unequivocally demonstrated that the locus of failure remains at the interface throughout the lifespan of the specimen, with no transition to cohesive or substrate failure even at advanced stages. The multi-modal, sometimes alternating crack trajectory (confirmed by DIC and sequential optical imaging) indicates the activation of complex stress fields during cycling and confirms that crack advance can be highly sensitive to local interface variations and mixed-mode loading effects.

The rapid crack initiation and steady propagation at comparatively low cycle counts (<20,000 cycles) reflect the interface's central role in governing joint durability. However, the adhesive itself exhibited sustained performance, deferring ultimate failure to the weakest adhesion paths and highlighting the importance of interfacial optimization in joint design.

From a modeling perspective, the observed correspondence between strain localization, crack tip advance and process zone size provides a valuable experimental basis for future calibration and validation of advanced durability and lifetime prediction models, particularly those based on CZM or similar fracture mechanics approaches.

Chapter 10: Empowering dataset with characterization on bulk adhesive specimens

10.1 Introduction

The following experimental campaign was undertaken to rigorously characterize the intrinsic mechanical properties of the bulk polyurethane adhesive. While supplier datasheets may provide baseline values, these parameters frequently diverge from the true in situ response observed within assembled joints, especially when subjected to complex stress states encountered in full-vehicle simulations. A systematic assessment of tensile, shear and fracture properties on bulk adhesive specimens thus provides essential inputs for constitutive modeling, enabling accurate material card development for advanced finite element codes such as Abaqus. These experimentally validated bulk properties serve not only as an upper-bound reference for joint performance, but also as a critical foundation for calibrating and validating the cohesive and viscoelastic behaviors required in modern simulation workflows.

10.2 Specimen definition

All bulk adhesive specimens were manufactured, as already outlined in Section 3.3.5.with a custom-design gluing jig for each type of specimens. CT and Dogbone specimens were manufactured by injecting the adhesive with a mechanical gun into the gluing jig and then left to cure. Thick Shear specimens were bonded with aluminum adherends designed to be ASTM-compliant. Rod joint specimens were bonded with steel cylindric adherends. Both Thick Shear and Rod joint were bonded to obtain 1.5 mm adhesive gap between the adherends, to be comparable with adhesive thicknesses used in the previous experimental campaigns. Mechanical test results are presented and discussed in Section 10.4 while fractographic evidence are presented in Section 10.5.

10.3 Mechanical Testing

For this phase a total of 40 specimens were tested:

- N° 10 specimens for Dogbone samples.
- N° 10 specimens for TLS samples.
- N° 10 specimens for Rod joint samples.
- N° 10 specimens for CT samples.

10.3.1 Dogbone

The tests were carried out on a Z020 by ZwickRoell Universal testing machines with a 1 kN load cell equipped with a pneumatic gripping fixture at 6 bar, ensuring that the specimens were correctly held and aligned to minimize any bending moments. A video extensometer (ZwickRoell's VideoXtens) was pointed towards the specimen to observe/measure strain. The specimen was re-loaded at 5 N, the test was conducted at a constant crosshead speed of 5 mm/min until the extensometer have registered a strain variation of 0.5 mm, then the test speed was set to 50 mm/min up to failure. Elastic modulus calculation is performed over a precisely defined strain interval because of the non-linear behavior of the adhesive between 0.5% and 1% of the first trait of the curve. Pictures of the testing phase are presented in Figure 54.

10.3.2 Thick Lap Shear

The tests were carried out on a Universal testing machine with a 20 kN load cell (Z020 by ZwickRoell) equipped with a clamping fixture, ensuring that the specimens were correctly held and aligned to minimize any bending moments. The shear modulus of elasticity determined as for the dogbone specimen above, so from the interval between 0.5% and 1% of the regression linear trait of the stress-strain curve A video extensometer (ZwickRoell's VideoXtens) was pointed towards the specimen to observe/measure strain. The specimen was pre-loaded at 20 N and the test was conducted at a constant crosshead speed of 2455 N/min until failure.

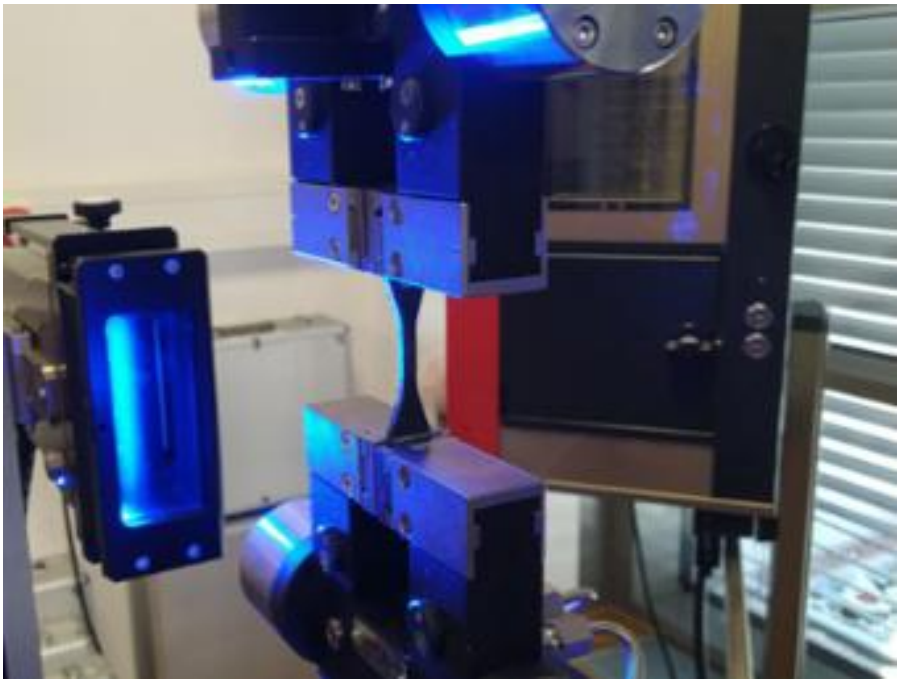

Figure 54: Testing of Dogbone specimens

Figure 56: Testing of Rod Joint specimen

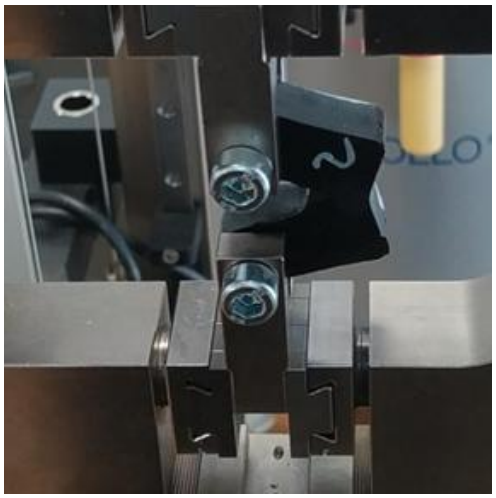

Figure 56: Testing of Compact Tension specimen

10.3.3 Rod Joint

The tests were carried out on a Universal testing machine with a 20 kN load cell (Z020 by ZwickRoell) equipped with a fixture that connects to the specimen via pins, ensuring that the specimens were correctly held and aligned to minimize any bending moments. The specimen was pre-loaded at 20 N and the test was conducted at a constant crosshead speed of 2000 N/min until failure. Pictures of the testing phase are presented in Figure 55.

10.3.4 Compact Tension

The tests were carried out on a Universal testing machine with a 20 kN load cell (Z020 by ZwickRoell) equipped with a fixture that connects to the specimen via pins within a hole derived directly on the specimen by design, ensuring that the specimens were correctly held and aligned to minimize any bending moments. The specimen was pre-loaded at 5 N and the test was conducted at a constant crosshead speed of 10 mm/min until failure. Pictures of the testing phase are presented in Figure 56.

10.4 Mechanical testing Results

10.4.1 Dogbone

Force-Displacement results from Dogbone test are reported in Figure 57. Between samples, the coefficient of variations of mean values is greater than 13%. Due to the testing methodology already described in Section 3.4.4, initial force-displacement data showed a change in stiffness related to the change of the test speed from 5 to 50 mm/min. The final data were post-processed to get rid of the dynamic effect of the speed change and obtaining more meaningful data. Force–displacement curves from bulk adhesive dogbone tests display nonlinear, ductile behavior for all specimens, lacking a distinct linear elastic region typical of stiffer materials. After applying a post-processing correction for changes in test speed, all specimens followed similar profiles: an initial segment of increasing stiffness, a broad maximum and abrupt force drops corresponding to final failure. Peak force and displacement at failure varied among the samples, with the lowest curve terminating near 200 N and several exceeding 350 N before failure.

Quantitative analysis reveals a mean ultimate tensile strength of 15.2 MPa (standard deviation: 0.97 MPa) and an average elongation at break of 38% (standard deviation: 6.97%), underscoring the adhesive's substantial ductility. The mean elastic modulus was 245 MPa, with a moderate spread among samples (standard deviation: 32 MPa) and the mean Poisson's ratio was 0.47 with low variability. These outcomes confirm the adhesive's ability to sustain high strains prior to fracture, characteristic of flexible, energy-absorbing systems. All numerical values, including mean and standard deviation. Means and standard deviations values for elastic modulus, stress and peak force are showed in Table 18.

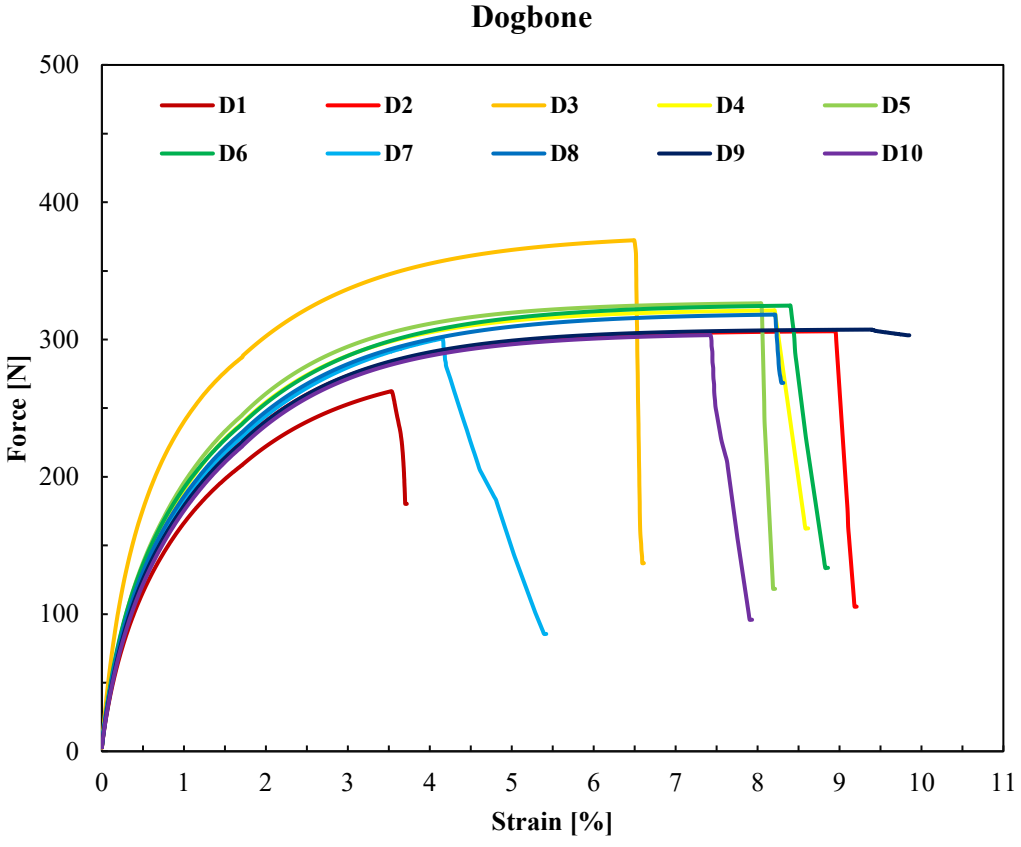

Figure 57:Results from mechanical testing of Dogbone specimens

Table 18: Mean experimental results for tensile elastic modulus from dogbone specimens

TEST	Spec. N°	Elastic Modulus [MPa]	Poisson's ratio	Stress at break [Mpa]	Elongation at break [%]
Dogbone	**1**	200	0.43	13	35.2
	2	240	0.48	15	42.99
	3	330	0.46	17	31.13
	4	250	0.48	15	38.61
	5	250	0.5	16	39.59
	6	250	0.5	15	39.41
	7	230	0.45	15	22.74
	8	250	0.47	16	41.56
	9	230	0.51	15	50.46
	10	220	0.46	15	38.23
	Mean Values	245	0.47	15.2	38
	Std. Dev.	32.32	0.02	0.97	6.97

10.4.2 Thick Lap Shear

Force-Displacement results from Thick Lap Shear test are reported in Figure 58. Between samples, the coefficient of variations of mean values is greater than 12%. Force–strain curves from the Thick Shear configuration show a variable initial elastic region for all specimens, generally extending up to about 100 N, after which the stiffness notably decreases leading to failure. Ultimate loads cluster around 900–1100 N, with mean shear stress at break measured at 2.94 MPa and relatively consistent between specimens (standard deviation: 0.33 MPa). Strain at break is uniformly low, averaging just 0.03 and the calculated shear moduli, although variable, average over 870 MPa. These values are physically inconsistent when compared to the tensile modulus of the material, both from manufacturer data and prior bulk tests. The characteristic shapes of the curves further deviate from classic lap shear specimen response, with most curves exhibiting pronounced softening and plateauing after initial elastic behavior without the sharp transition typical of uniform bulk shear deformation. The unexpectedly high measured shear modulus, exceeding tensile modulus by a factor of four, strongly suggests that the test did not characterize true bulk shear response, but rather captured interfacial slip phenomena, potentially arising from inadequate adhesion, geometric distortion, or non-uniform specimen stress distribution.

Consequently, these results should not be interpreted as representative of the adhesive's inherent shear performance, but rather as evidence of test configuration limitations and dominant interfacial effects. This highlights the need for careful design and validation of bulk shear experiments, particularly when targeting mechanical properties for simulation input or material card development. Means and standard deviations values for shear stress and peak force are showed in Table 19.

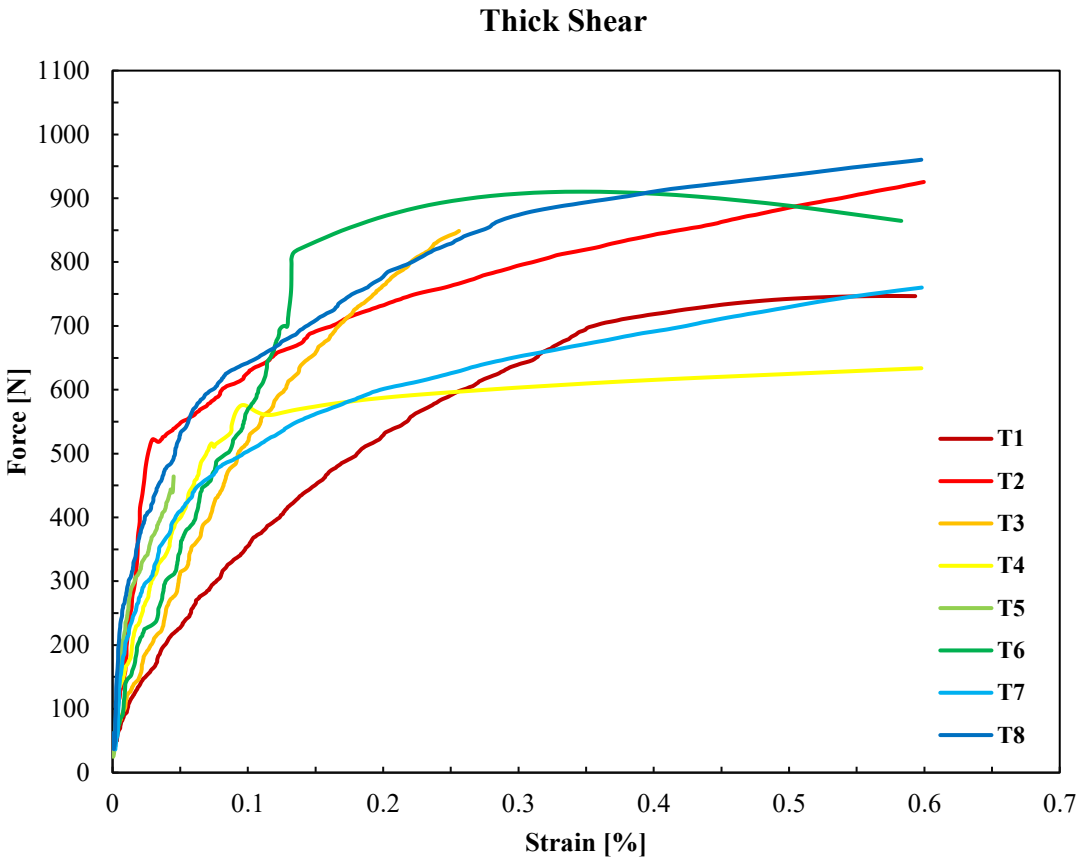

Figure 58:Results from mechanical testing of Thick Lap Shear specimens

Table 19: Mean experimental results for shear modulus from TLS specimens

TEST	Spec. N°	Shear Modulus [MPa]	Force at break [N]	Stress at break [Mpa]	Strain at break [%]
Thick Shear	**1**	463.45	747	2.24	0.03
	2	1515.4	1090	3.36	0.07
	3	426.21	993	3.03	0.02
	4	1263.84	1060	3.28	0.01
	5	552.69	1040	3.21	0.04
	6	843.05	912	2.83	0.02
	7	679.54	895	2.76	0.02
	8	1243.94	916	2.81	0.03
	Mean Values	873.51	956.62	2.94	0.03
	Std. Dev.	389.11	104.95	0.33	0.01

10.4.3 Rod Joint

Force-Displacement results from Rod Joint test are reported in Figure 59. Between samples, the coefficient of variations of mean values is greater than 16%, mostly due to anomalies and the initial slack in the mechanical setup that required corrective post-processing. After the displacement gap was compensated, most curves follow a comparable trend: a progressive rise to peak load between 500 and 800 N, followed by a non-instantaneous force drop characteristic of quasi-ductile or slip-driven failure. Some curves show multi-peak behavior, highlighting possible stick-slip phenomena or gradual debonding.

Quantitative results indicate a mean tensile stress at failure of 8.8 MPa (standard deviation: 1.5 MPa) and mean displacement at break of 4.2% (standard deviation: 0.11%), underscoring moderate ductility of the rod joint configuration. While failure loads and stress values across the batch are generally consistent, the wide curve variability underscores the sensitivity of this geometry to subtle mechanical and operational factors.

The outcome reflects the adhesive joint's ability to sustain substantial load and deformation before failure in rod configurations but also highlights the necessity for rigorous test alignment and data post-processing to ensure reproducibility and accurate interpretation. Means and standard deviations values for normal stress and peak force are showed in Table 20.

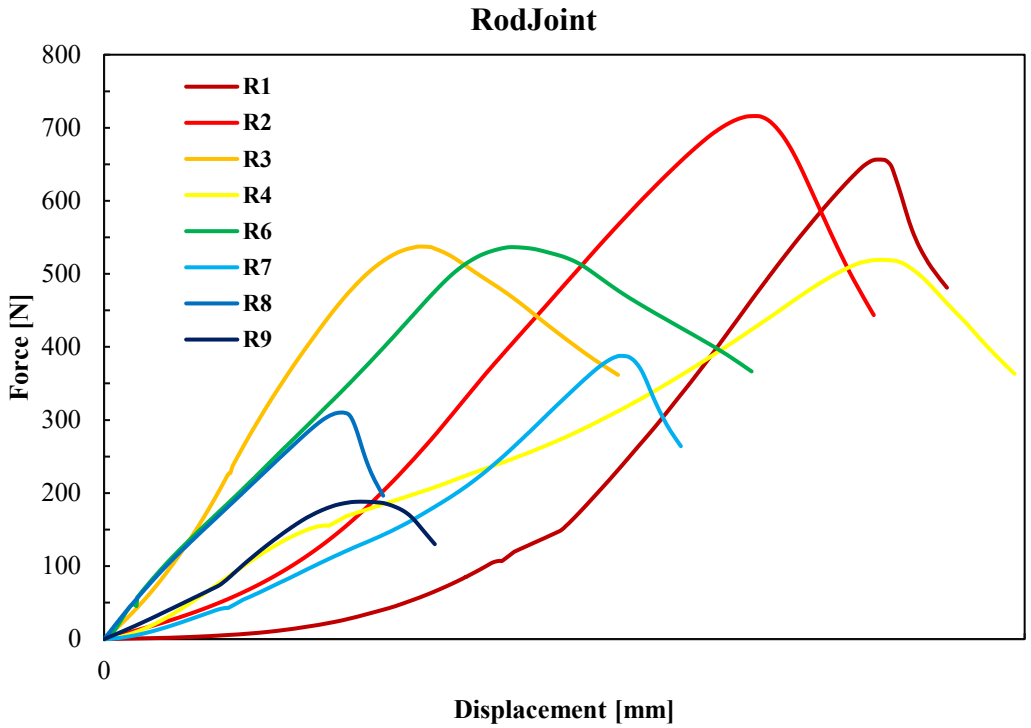

Figure 59:Results from mechanical testing of Rod Joint specimens

Table 20: Mean experimental results for tensile strength from rod joint specimens

TEST	Spec. N°	Force at break [N]	Stress at break [Mpa]	Elongation at break [%]
RodJoint	**1**	538.01	6.85	4.4
	2	724.54	9.23	4.3
	3	812.42	10.3	4.2
	4	720.42	9.18	4.3
	5	466.86	5.95	4.2
	6	751.24	9.57	4.1
	7	737.97	9.4	4.2
	8	805.16	10.3	4
	Mean Values	694.57	8.84	4.21
	Std. Dev.	116.8	1.48	0.11

10.4.4 Compact Tension

Force-Displacement results from CT test are reported in Figure 60. Between samples, the coefficient of variations of mean values is greater than 12%, showing consistent results through all the specimens. Force–displacement curves from CT tests show good repeatability in the initial elastic segment up to approximately 100 N for all specimens, followed by a progressive loss of stiffness as crack initiation and growth occur. Most curves reach their peak, typically between 250 and 350 N, after which force declines smoothly, indicating stable, ductile crack propagation rather than abrupt, brittle failure.

The mean peak force at crack initiation is about 297 N (standard deviation: 28 N), with a corresponding mean critical fracture energy G_c of 2000 J/m² (standard deviation: 332 J/m²). Consistency of key metrics aligns with the observed response in the curves, supported by the comparable spread in stress intensity factor values K_q (mean 0.96 MPa·m^{1/2}, standard deviation: 0.10), confirming robust repeatability across the batch.

These results quantitatively characterize the fracture resistance of the adhesive material in compact tension geometry, providing a reliable reference for toughness and crack stability in simulation-based assessments and engineering calculations. Means and standard deviations values for fracture energy and peak force are showed in Table 21.

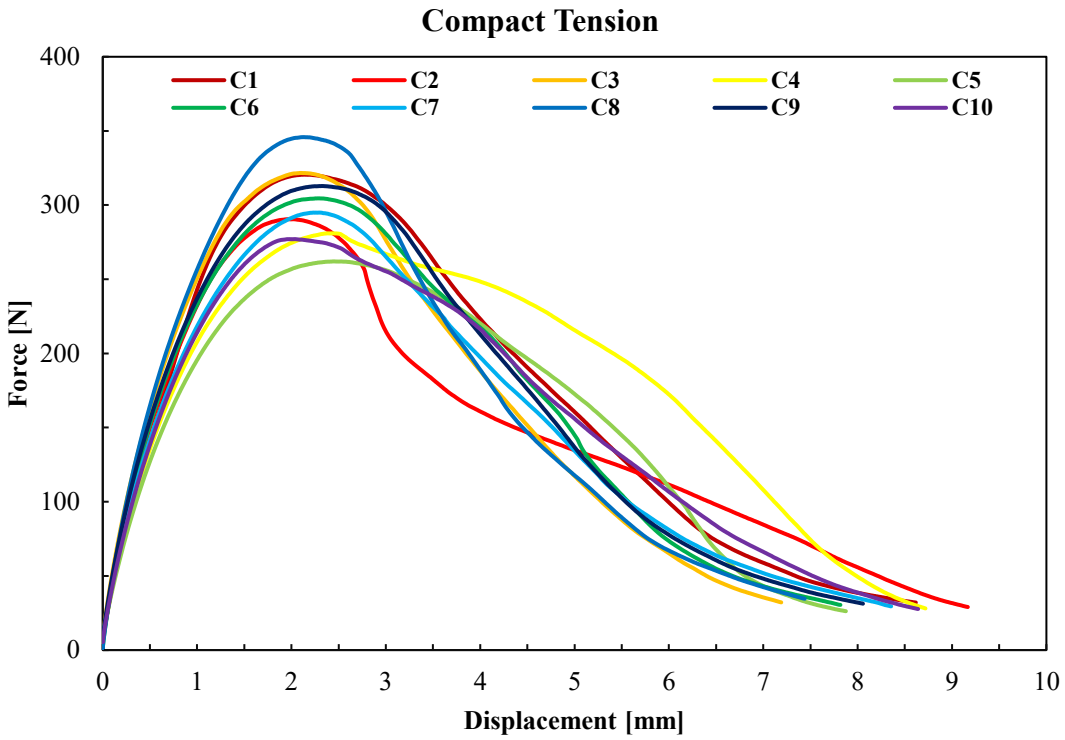

Figure 60:Results from mechanical testing of Compact Tension specimens

Table 21: Mean experimental results for fracture energy from CT specimens

TEST	Spec. N°	Force at break [N]	Force at 5% [N]	Critical fracture energy G_c [J/m^2]	Stress intensity factor K_q [MPa*m^1/2]
CT	**1**	320.5	271.8	2160.3	1.06
	2	290.5	239.7	1823.5	0.94
	3	321.7	274.6	2291.9	1.03
	4	281	217.3	1643.6	0.8
	5	262.1	199.3	1552.2	0.88
	6	304.5	252.7	2148.4	1
	7	249.9	235.5	1947.6	0.9
	8	345.8	293.1	2680.3	1.17
	9	312.8	254.3	2089	0.98
	10	277	218.7	1625.2	0.87
	Mean Values	296.58	245.7	1996.2	0.96
	Std. Dev.	28.25	27.77	332.47	0.1

10.5 Fracture Surfaces

10.5.1 Dogbone

Fractographic analysis of dogbone specimens revealed a fully ductile failure mode, consistent with the polymeric nature of polyurethane adhesives. Samples underwent extensive elongation before break, displaying negligible necking in the central gauge region. The smooth, featureless surfaces typical of ductile polymers were consistent across all samples and indicative of homogeneous deformation up to failure. The most representative failed samples are showed in Figure 61.

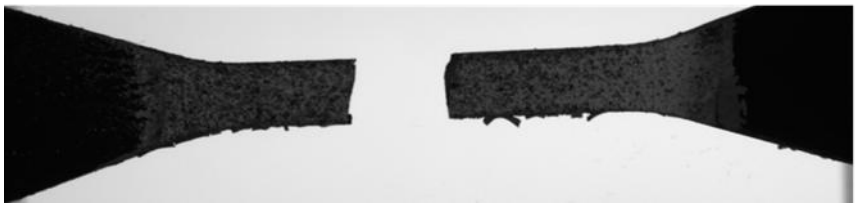

Figure 61: Dogbone specimen after fracture at peak load

10.5.2 Thick Lap Shear

For the thick lap shear configuration, the predominant failure mechanism was adhesive in nature, with fracture occurring at the aluminum–adhesive interface. Isolated residual patches of adhesive were sometimes observed, signaling partial failure initiation linked to suboptimal surface preparation or weak boundary layers. This agrees with published SEM studies showing adhesive-dominated failure for poorly adherent systems, particularly in tests where interface slip overtakes bulk material deformation. The most representative failed samples are showed in Figure 62.

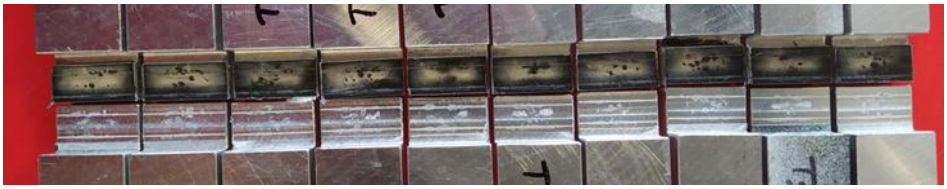

Figure 62:Thick Lap Shear specimen after fracture at peak load

10.5.3 Rod Joint

Rod joint fracture surfaces commonly exhibited a mix of adhesive and cohesive features. While adhesive debonding dominated, in several cases a central cohesive remnant was retained on one adherend, pointing to an initial interface-initiated crack propagating partially through the bulk adhesive. This points to the interplay between true interface weakness and local bulk fracture under multi-axial stress failure pathway not uncommon in complex polyurethane bonds. The most representative failed samples are showed in Figure 63.

Figure 63:Rod Joint specimen after fracture at peak load

10.5.4 Compact Tension

Compact tension specimens consistently featured stable crack propagation, with fracture originating from the sharp pre-crack and merely deviating during the terminal phases. In literature, this deviation is linked to microstructural heterogeneity or molding artifacts, a finding corroborated by the dense core occasionally seen in injection-molded samples. Such terminal deviations did not influence the calculated fracture energies, confirming the reliability of the test for toughness evaluation. The most representative failed samples are showed in Figure 64.

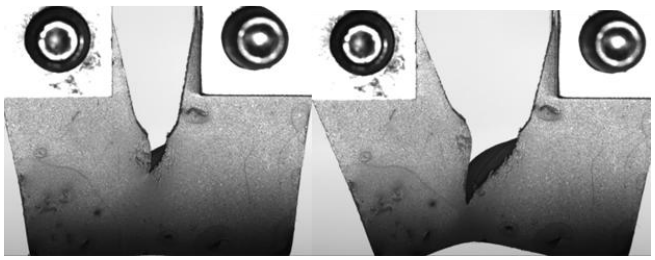

Figure 64:Compact Tension specimen after fracture at peak load

10.6 Conclusion

The bulk adhesive specimen campaign established, with high experimental certainty, the intrinsic mechanical and fracture properties that serve as the baseline for both engineering application and advanced material card calibration:

- Dogbone specimens consistently demonstrated fully ductile behavior, with mean ultimate strength of 15 MPa, elongation at break of 38% and modulus of 250 MPa, values reflecting the upper limit of toughness and plasticity for this polyurethane system.
- The thick lap shear test, dominated by interfacial slip and adhesive failure, yielded anomalously high moduli and low strains, underscoring the crucial impact of test setup and interface control in shear property extraction.
- Rod joint tests confirmed the presence of mixed adhesive–cohesive pathways and a mean tensile strength of 8.5 MPa, further mapping the true vs. effective strength for tensile loading in bonded geometries.
- Compact tension tests validated a mean fracture energy of 2000 J/m², aligning with literature for highly toughened adhesives, with stable propagation and only end-of-test path deviations due to molding effects.

Fractographic evidence consistently highlighted the dominance of ductile failure in the bulk (dogbone, compact tension) and adhesive or mixed-type failure in jointed or interfacial-dominated tests (thick shear, rod joint). Taken together, these results both define the mechanical “envelope” for polyurethane adhesives and provide a robust, experimentally validated foundation for simulation, design and the calibration of cohesive zone models and advanced FE material cards.

Chapter 11: Material Card Procedure

11.1 Introduction to Numerical Analysis

The purpose of this procedure is to define the methodology for generating a numerically calibrated material card for structural adhesives, suitable for use in advanced finite element analysis environments such as Abaqus and consistent with the requirements of Altair HyperStudy. The methodology outlined here is tailored for specific application to Carbon-SMC polyurethane adhesive bonded joints, commonly used in automotive context.

This material card generation process is inherently application- and mesh-dependent: each combination of joint geometry (e.g., DCB, SLJ), adherend/adhesive type and finite element mesh specification requires a dedicated calibration cycle. The preliminary mechanical characterization of both adherends (tensile, flexural, or shear properties) and the adhesive layer (tensile, shear and fracture tests) is a prerequisite for the qualification and creation of a reliable card.

All target test configurations are physically modeled to reflect the standards used for experimental validation (ASTM D5528 for DCB, ASTM D3165 for SLJ), ensuring a robust correspondence between experimental evidence and simulation. It is noted that, at the modeling level, nominal adhesive thicknesses, temperature (room temperature) and surface treatments (such as roughening or plasma treatment) are not explicitly simulated but must match experimental test conditions for the results to be valid.

The specific objective is to iteratively calibrate the material card parameters (elastic properties, failure stresses and fracture energies in each orthotropic direction, as well as the degradation parameter for the CZM) so that the simulated force–displacement results of virtual DCB and SLJ specimens provide the closest match to their experimental counterpart. When these results meet in-house and industry acceptance criteria, the card is validated and can be deployed in higher fidelity automotive structure simulations This section outlines the specific methodology employed in this research, combining targeted experimental characterization with an automated inverse engineering framework primarily utilizing Altair HyperMesh software as modeling tools, Abaqus software for base simulations and Altair HyperStudy software to calibrate and optimize the derived necessary constitutive parameters.

The FE models were constructed to geometrically replicate the test specimens according to the relevant standards: ASTM D3165 for the SLJ with adherend dimensions 25 x 110 x 4.1mm and ASTM D5528 for the DCB with adherend dimensions of 20 x 200 x 4.1 mm, both modeled with a nominal adhesive gap of 1.5 mm. The primary objective of this numerical work was to accurately simulate the experimental conditions described in Chapter 5, enabling a robust correlation between physical tests and virtual predictions.

11.2 Preliminary Operations

Before commencing the material card calibration workflow, several critical preparatory steps must be taken to ensure the reliability and reproducibility of the result:

- **Selection of Adhesive and Adherend Types:** Identify the specific adhesive system (e.g., polyurethane or epoxy) and its nominal thickness for the intended application. Similarly, select the adherend materials (e.g., Carbon-SMC, Glass-SMC, aluminum) and their respective thicknesses. Document the exact product names/codes and relevant datasheet values for initial guidance.

- **Surface Preparation:** Define and apply a consistent surface treatment protocol (such as sandblasting, plasma treatment, or primer application) for all experimental joints. Note that, while surface treatment is crucial for experimental qualification, it is not explicitly modeled in the FE simulations. Test and modeling conditions must be consistent for meaningful comparison.

- **Mechanical Property Acquisition:** Gather or experimentally determine the mechanical properties of both the adherends (tensile modulus, Poisson's ratio, strength) and the bulk adhesive (tensile, shear, fracture properties). Reference values may be taken from material datasheets, but direct quasi-static mechanical tests (e.g., ASTM-based tensile or fracture tests) are preferred for calibration fidelity.

- **Specification of Joint Types and Dimensions:** For each joint configuration to be modeled (typically DCB per ASTM D5528 and SLJ per ASTM D3165), fully specify dimensions, adherend stacking sequence (for composites) and adhesive gap. Ensure these matches precisely with those used in the experimental campaign.

- **Acquisition of Experimental Reference Data:** Generate or collect high-quality force–displacement data from experimental tests, ensuring coverage of both fracture (DCB) and shear (SLJ) regimes. These datasets serve as the objective benchmarks for model calibration.
- **Definition of Mesh and Model Discretization:** Plan the finite element mesh densities for both the adhesive (typically finer, e.g., 2.5 mm) and the adherends (coarser, e.g., 5 mm). The calibration is mesh-dependent, so the mesh must be consistent throughout the process.

Note: These preliminary operations are not only essential for reproducibility but are also a formal requirement for ensuring the validity of subsequent model calibration and for meeting typical industry standards.

11.3 Modeling

In this stage, detailed finite element models are constructed to replicate the Double Cantilever Beam (DCB) and Single Lap Joint (SLJ) test specimens according to their respective standards (ASTM D5528 for DCB, ASTM D3165 for SLJ). The modeling process uses Altair HyperMesh for pre-processing and Abaqus/Explicit as the finite element solver, ensuring seamless integration with Altair HyperStudy for subsequent optimization.

11.3.1 Adherends

- The composite (e.g., Carbon-SMC) adherends are modeled with 4-node continuum shell elements (S4R), chosen for their balance between computational efficiency and the ability to capture laminate effects. A uniform mesh size of 5 mm is assigned, reflecting a compromise between accuracy and computation time that has been validated in previous studies.
- Laminate layup is defined according to the actual tested material: for Carbon-SMC, the ply sequence ([0/90/45/-45]sym) and thickness (usually 8 plies for a 4.1 mm part) are explicitly assigned via a *SHELL SECTION, COMPOSITE definition, capturing quasi-isotropic behavior.
- Adherend properties (modulus, strength, failure criteria) are input either from direct experiment or provider datasheet but always finalized in line with the preliminary characterization phase.

11.3.2 Adhesive Layer

- The adhesive is modeled using three-dimensional cohesive elements (COH3D8), allowing direct simulation of interface fracture using a traction–separation law (CZM).
- A finer mesh (typically 2.5 mm) is adopted in the bondline to capture stress gradients and potential process zone effects, in accordance with best practices for cohesive zone modeling.
- The directionality and orientation of the cohesive elements (normal to the bonded surface) are carefully checked to avoid artificial stiffness or improper crack propagation.

11.3.3 Material Assignments and Properties

- Cohesive zone material parameters (elastic modulus, peak traction, fracture energies in all orthogonal directions and degradation) are set as variables, ready to be calibrated in subsequent stages.

- The tie constraint (*TIE) is employed at the interface between cohesive elements and adherend elements, rigidly linking nodes to prevent numerical sliding and enforce perfect adhesion at the cohesive zone.

11.3.4 Geometric and Boundary Definition

- Test geometries and boundary conditions are implemented according to standards (See Figure 65):
    - SLJ specimens: 25 × 110 × 4.1 mm adherends, bonded over a 15 × 25 mm overlap, 1.5 mm adhesive gap.
    - DCB specimens: 20 × 200 × 4.1 mm adherends, 75 mm initial crack/precrack, 1.5 mm adhesive gap.
- Reference nodes at specimen ends are defined for loading and boundary imposition. Kinematic coupling constraints ensure transfer of applied force/displacement rigidly to all nodes at the end faces.

11.3.5 Additional Notes

- Element deletion and hourglass control options are enabled for the cohesive and shell elements, promoting convergence in simulations with damage evolution.
- Mesh sensitivity/robustness is checked in early runs (especially for cohesive elements) to ensure that the response is not artificially mesh-dependent within the chosen density range.

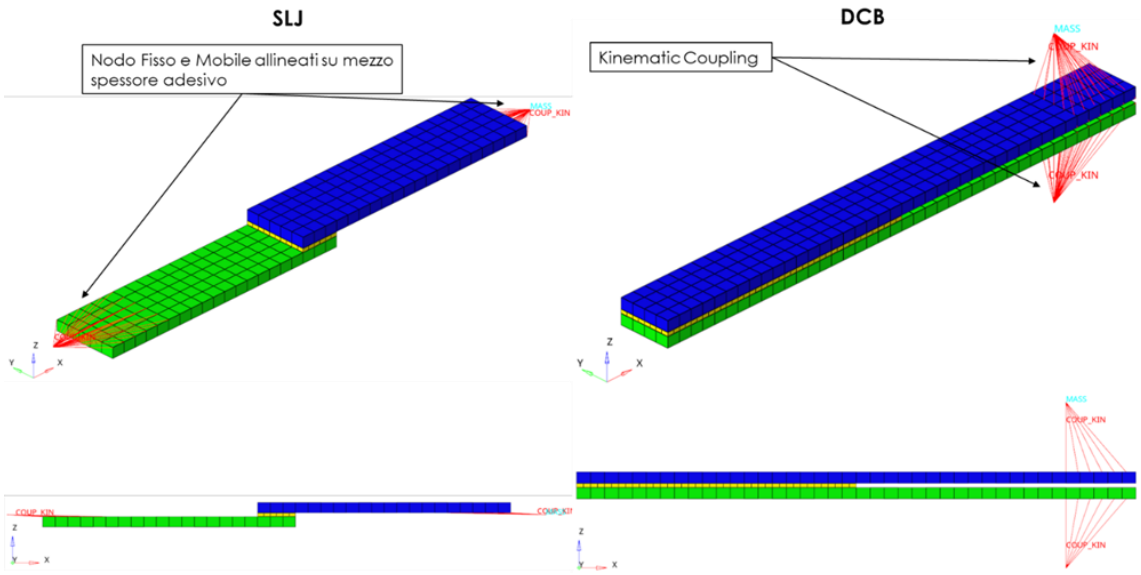

Figure 65: Results of SLJ (left - 408 nodes, 263 elements) and DCB (right - 1150 nodes, 643 elements) specimen modeling.

11.4 Simulations

Once the finite element models are built, the next crucial step involves accurately replicating the experimental loading and boundary conditions in the simulation environment, ensuring that the virtual setup matches the physical tests for rigorous comparison and calibration.

11.4.1 Boundary and Loading Conditions

- **Reference Nodes and Kinematic Coupling:** For each test model (DCB, SLJ), reference (control) nodes are defined at each specimen end. Kinematic coupling constraints link these reference nodes to all the nodes on the corresponding end face, ensuring that imposed boundary conditions (loads/displacements) are transferred uniformly to the model.

- **Fixed Node (ENCASTRE):** The "fixed" reference node is fully constrained in all degrees of freedom for most cases, representing the clamped or fixed end in the physical test. For the DCB test, rotational freedom about the hinge axis is preserved to mimic proper opening movement during the delamination event.

- **Loading Node and Prescribed Motion:** The "mobile" reference node is constrained in all degrees of freedom except for the direction of applied displacement (typically the loading direction). Tensile (opening or shear) loads are imposed via a prescribed velocity consistent with the experimental quasi-

static rate (usually through *INITIAL CONDITIONS, TYPE=VELOCITY or *BOUNDARY, TYPE=DISPLACEMENT in Abaqus).

11.4.2 Solution Control and Mass Scaling

- **Solver Choice:** All simulations are executed using the Abaqus/Explicit dynamic solver. While explicit solvers are conventionally used for dynamic problems, here they enable stable integration even with nonlinear behaviors such as damage evolution, cohesive debonding and element deletion.
- **Mass Scaling:** To control computational cost, a Fixed Mass Scaling factor (e.g., 2.5e-5 for DCB, 5e-5 for SLJ) is applied. Forcing a large mass value (e.g., 1E+15) on the mobile reference node further stabilizes the time increment, speeding up the simulation while maintaining accuracy and avoiding nonphysical inertia effects. This is an accepted practice for quasi-static loading in explicit simulations.

11.4.3 Output and Validation

- Force and displacement histories at reference nodes are extracted and processed identically to experimental data for quantitative comparison.
- Simulations are first performed as verification runs to test convergence and the consistency of boundary/loading settings. For both SLJ and DCB, particular care is paid for the correct replication of the mechanical constraints and free degrees of freedom, especially the hinge rotation for DCB and uniform displacement transfer for SLJ.

11.4.4 Notes

- Tie constraints between adherends and cohesive layers ensure consistent stress transfer across all mesh densities and material transitions, preventing artificial slip between regions.
- Special attention is given to the effect of kinematic constraints and scaling strategies to ensure that they do not artificially stiffen the response or modify the physical interpretation of the results.

An example of correlation between numerical model simulations and experimental evidence on failure modes are shown in Figure 66.

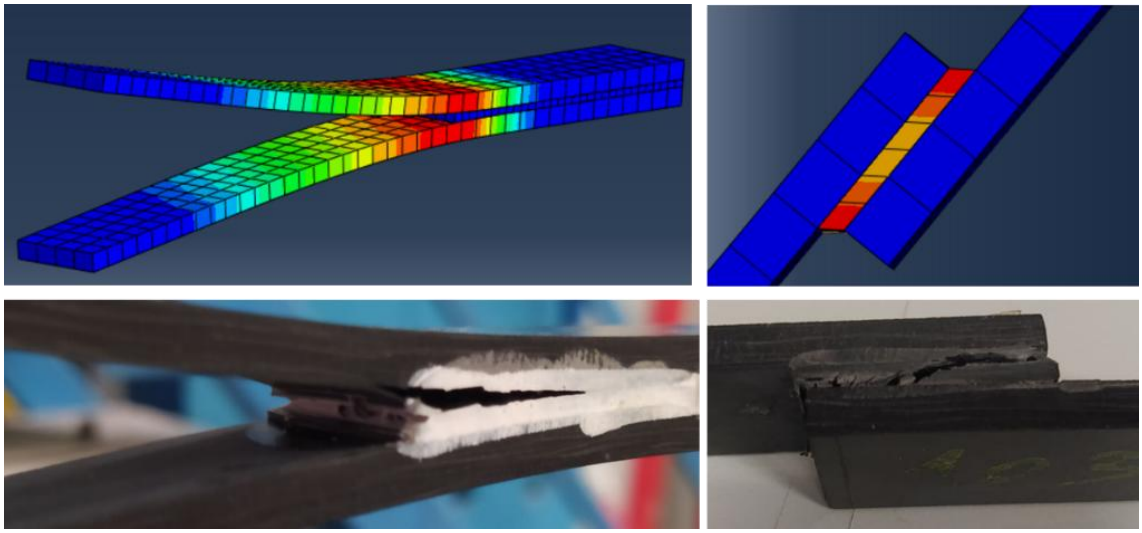

Figure 66: Comparison between numerical model simulations and experimental failure mode of DCB (left) and SLJ (right).

11.5 HyperStudy Software Intro

For this research, Altair HyperStudy was selected as the primary tool to orchestrate the model calibration process. HyperStudy is a multidisciplinary design exploration, optimization and stochastic study software. While it is broadly used for design optimization (minimizing mass or maximizing stiffness), its framework is perfectly suited for the inverse problem of material parameter identification.

The utility of HyperStudy in this context derives from its ability to partially automate the entire workflow, seamlessly integrating with the Abaqus solver to find the set of material parameters that provides the best fit to the experimental force-displacement curves from the SLJ and DCB tests. The core of the methodology relies on three key functionalities:

- **Design of Experiments (DOE):** Instead of random guessing, HyperStudy employs DOE algorithms to systematically generate a set of simulations. Each simulation uses a different combination of the unknown material parameters within a predefined range. This ensures the design space is explored efficiently, providing a comprehensive understanding of how each parameter influences the model's response.

- **Approximations (FIT):** Running hundreds of detailed FE simulations can be computationally prohibitive. To overcome this, HyperStudy uses the results from the DOE phase (or from any given data set) to construct a response surface. This is an analytical mathematical function that approximates the complex relationship between the input material parameters and the output force-displacement curve. Once built, this model can be evaluated almost instantly, replacing the expensive FE simulation in the optimization phase.
- **Optimization:** With the computationally efficient models in place, HyperStudy deploys powerful optimization algorithms to search for the optimal solution. In this work, the objective function was defined to minimize the root mean square error (RMSE) between the experimental curve and the curve predicted by the model. The optimization process therefore identifies the combination of cohesive law parameters that results in the closest possible match to the real-world test data, yielding a calibrated and validated material card.

11.6 Hyperstudy Procedure

With the experimental data and modeling tools established, an inverse engineering framework is configured to automate the calibration of the material card parameters. This involves several key steps to follow HyperStudy software that will be partially described in the following sections because of company-private-procedure [145].

11.6.1 Model Definition (Setup):

For each set of materials to be characterized (SMC and Parker LORD adhesive) a high-fidelity FEA model of the two experimental test specimens (identified as mandatory to obtain the material card were created as described on the previous chapter: tensile SLJ and energy fracture DCB coupon). These models incorporate the chosen constitutive material law and the key parameters (E, T, G) must be set as variables for optimization. The FEA solver (Abaqus) is integrated into HyperStudy.

- **Input and Output Parameters:** Within HyperStudy's Setup module, the material parameters to be calibrated (Young's modulus, peak traction, fracture energy and cohesive element degradation parameter) are defined as *input variables*. The simulation outputs that correspond to the experimental measurements (force-displacement curves, specific displacement values, peak forces) are defined as

responses. On Figure 67 some screens from the software interface are provided to show the process of parameterization of the .inp Abaqus input file.

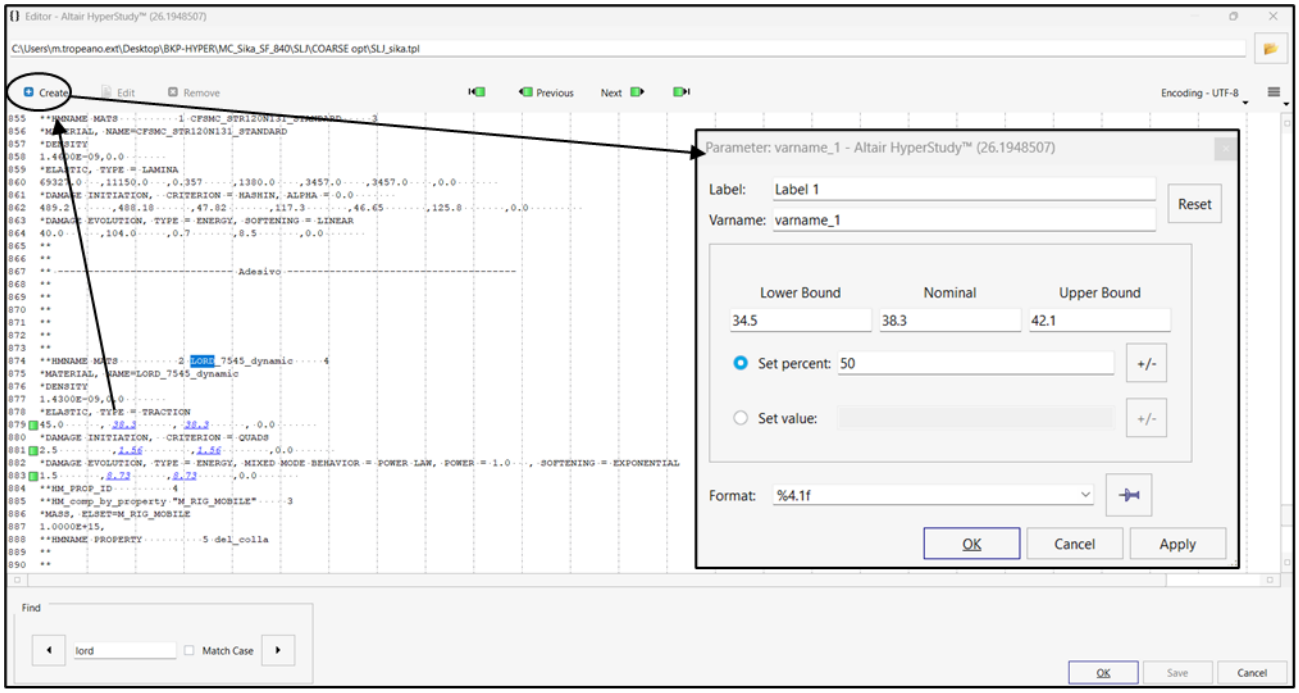

Figure 68: Parametrizing the file for input variables

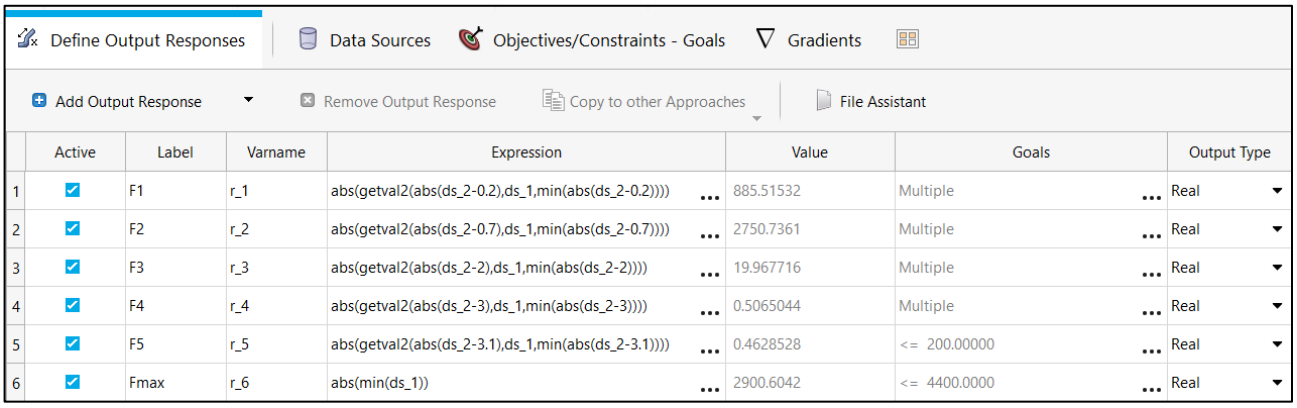

	Active	Label	Varname	Expression	Value	Goals	Output Type
1	☑	F1	r_1	abs(getval2(abs(ds_2-0.2),ds_1,min(abs(ds_2-0.2))))	885.51532	Multiple	Real
2	☑	F2	r_2	abs(getval2(abs(ds_2-0.7),ds_1,min(abs(ds_2-0.7))))	2750.7361	Multiple	Real
3	☑	F3	r_3	abs(getval2(abs(ds_2-2),ds_1,min(abs(ds_2-2))))	19.967716	Multiple	Real
4	☑	F4	r_4	abs(getval2(abs(ds_2-3),ds_1,min(abs(ds_2-3))))	0.5065044	Multiple	Real
5	☑	F5	r_5	abs(getval2(abs(ds_2-3.1),ds_1,min(abs(ds_2-3.1))))	0.4628528	<= 200.00000	Real
6	☑	Fmax	r_6	abs(min(ds_1))	2900.6042	<= 4400.0000	Real

Figure 68: Setting "objective points" on the software interface

- **Objective Function Definition:** An objective function is established to quantify the discrepancy between the numerical simulation results and the experimental data: when responses are mathematically defined in the software, the numerical responses were put “equal to” or were put “to aim” at the experimental corresponding results. This is done by visualizing the force-displacement plot of the chosen test and identifying some “checkpoints” on the entire curve to help the simulation: basically, the algorithm is forced to find solutions that can lead numerical force-displacement curves into passing through these points, ensuring the best curve overlap possible. For a more visual representation of the previous concept, a practical example is provided in Figure 69 and Figure 68. Constraints related to material parameter were also added and these “limits” ranges usually in a small portion around the selected point and given by either calculations of experimental standard deviation on that point or manually set by operator.

The Setup simulation parameters are ready and it can go for the first “run”, leaving a framework of software parameters settings that will be valid for the subsequent modules (FIT, Optimization and so on) avoiding the necessity of re-setting the responses for each different analysis and, more important, to leave a data set that can be read and analyzed by the subsequent modules.

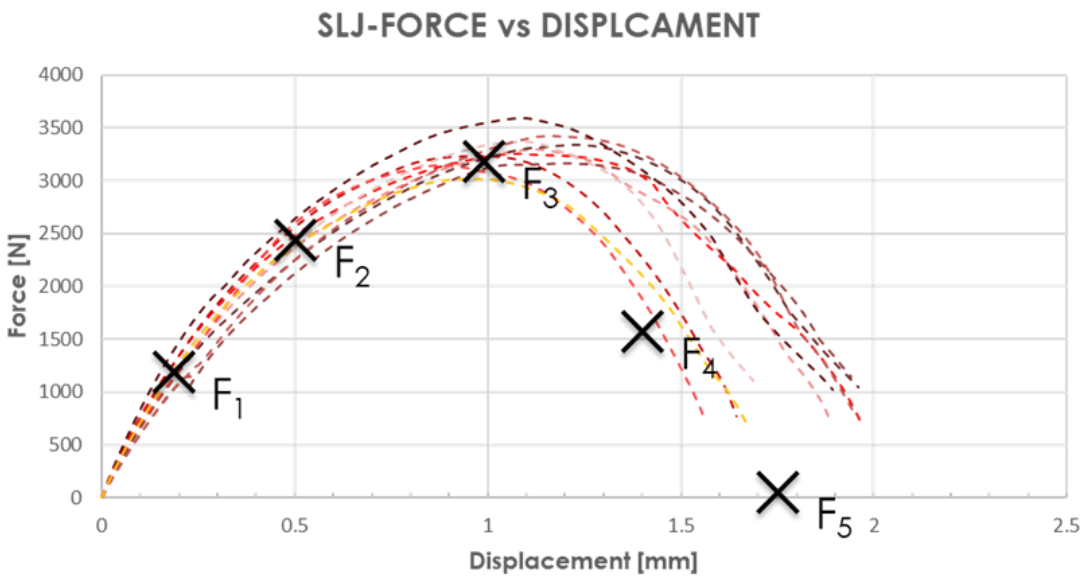

Figure 69: Selection of "objective points" on force-displacement curves of experimental SLJ data.

11.6.2 Design of Experiments (DOE)

Before proceeding to full optimization, a Design of Experiments (DOE) approach is employed.

The DOE module allows for a systematic exploration of the defined input parameter space. A set of specific parameter combinations is generated when the algorithm is selected and FEA simulations are automatically executed for each combination. This helps in understanding the sensitivity of the output responses to changes in the input material parameters, identifying influential parameters and creating a results database. For this study, the Latin HyperCube method was employed from the algorithm list presented by the software (See Figure 70). This sampling strategy was adopted because the adhesive and joint parameters investigated define a continuous, multidimensional design space. Compared to alternatives such as full factorial or Hammersley sampling, LHS provides a more efficient and unbiased exploration of parameter interactions with a limited number of runs, making it particularly suitable for sensitivity analysis and inverse calibration of cohesive zone models aimed at developing transferable adhesive material cards. This initial exploration is crucial for understanding the model's behavior.

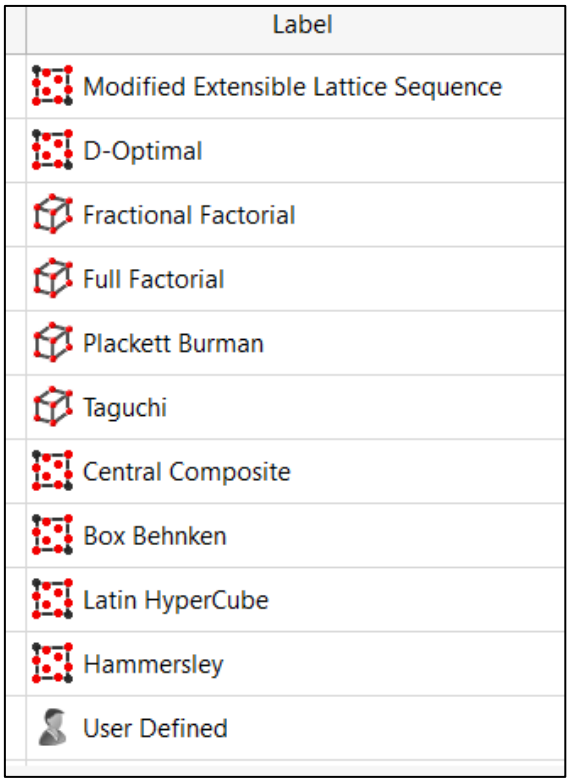

Figure 70: List of possible DOE algorithms

11.6.3 Response Surface (FIT)

Following the DOE, the FIT module in HyperStudy is utilized to construct a response surface model.

This involves using the results matrix from the DOE (input parameter sets and corresponding output responses) to generate an approximate mathematical model (polynomial or linear regression, Kriging and so on) that describes the relationship between the material input parameters and the simulation outputs. This response surface acts as a computationally inexpensive surrogate for the time-consuming FEA model. The accuracy of this fit is usually related to the quantity and quality of the base data set. For this study, the FAST - Fit

Automatically Selected by Training option was selected from the algorithm list presented by the software, that will automatically employ the best regression method depending on the base data set (See Figure 71).

When using HyperStudy's Fit module with the F.A.S.T. sampling settings, there is a potential risk of overfitting, particularly because the adhesive and joint response is highly nonlinear and the number of FE simulations is limited. Overfitting could cause the surrogate model to capture numerical noise rather than underlying physical trends, leading to inaccurate predictions outside the sampled parameter space. To mitigate this risk, cross-validation, appropriate selection of polynomial order and careful coverage of the parameter space (like using the Latin HyperCube algorithm) are essential to ensure that the metamodel remains physically meaningful and suitable for material card calibration.

The response surface significantly accelerates the subsequent optimization process by not only allowing rapid evaluation of the objective function without running full simulations for every parameter combination but also allowing to upload and use a pre-generated data set from external sources (excel files, analytical results, measurements and others).

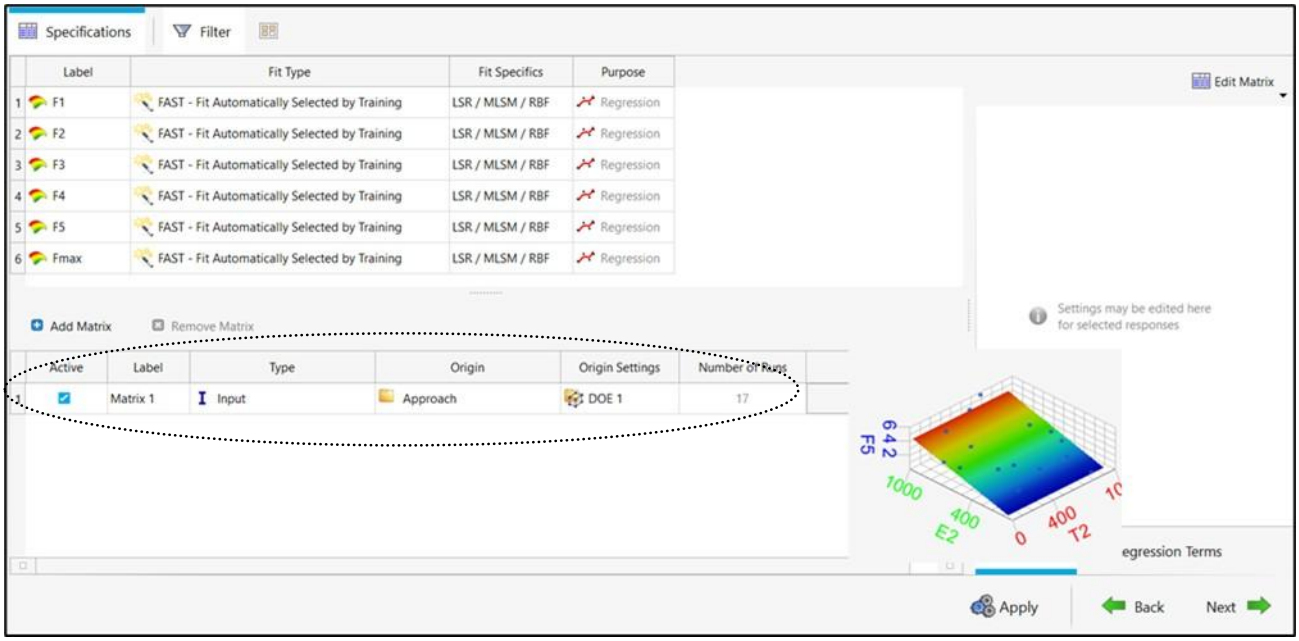

Figure 71: List of possible FIT algorithms, with particular focus on the selection of the inclusion matrix, necessary to read and process data without simulation and to generate an optimal "Response Surface"

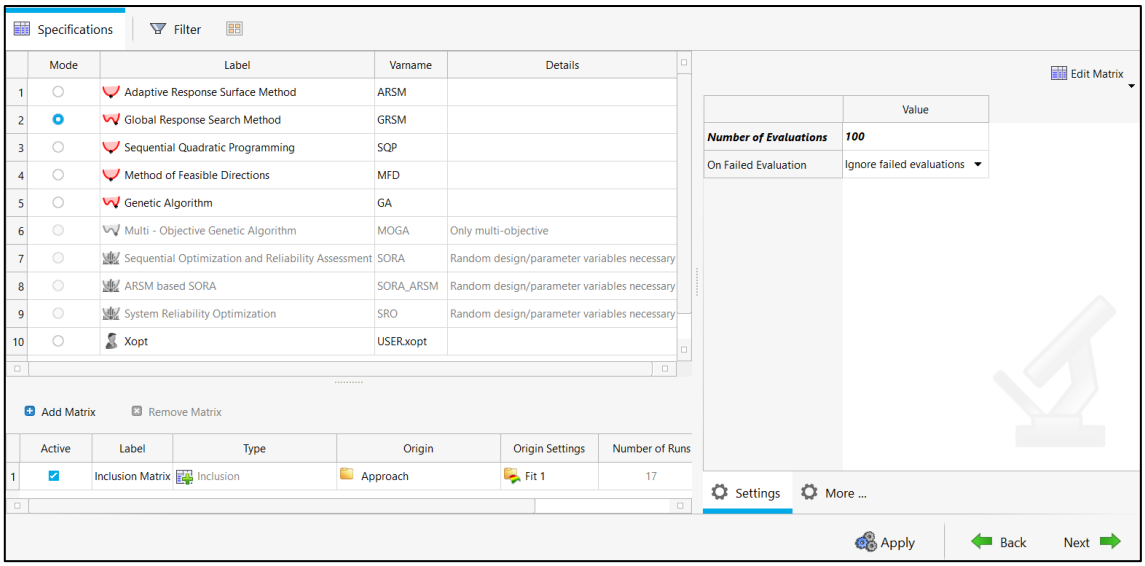

Figure 72: List of available algorithms in Optimization Tool

11.6.4 Optimization for Material Card Parameter Calibration

The final step is the Optimization of the material parameters.

With the response surface model in place an optimization algorithm is employed iteratively to search the parameter space, running FEA models, to find the set of material parameters that minimizes the defined objective function. The goal is to achieve the best possible match between the simulated material behavior and the experimental reference data. This iterative process refines all the parameters for the chosen constitutive law after each simulation and updating the response surface, resulting in the final calibrated material card. For this study, the GRSM - Global Response Search Method Algorithm was employed from the list presented by the software (See Figure 72).

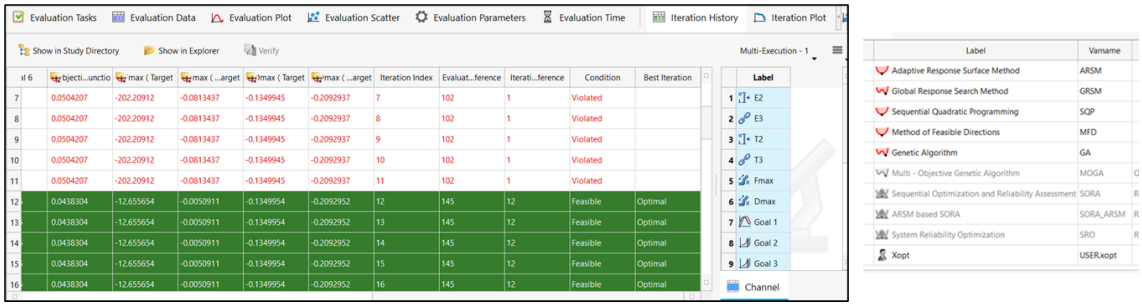

Figure 73: Results from optimization procedure: green rows represent "optimal" or feasible design while red one indicates that some constraints have been violated

In absence of a DOE+Response Surface dataset, the GRSM (and a few other Algorithms) are able not only to update, but also to create their own response surface.

The reason behind this concatenated methodology (Doe+FIT+Optimization) is linked to the different mathematical approaches that these algorithms uses: a GRSM method can be better at optimizing the results starting even from just one single simulation while inefficient in exploring the design space leading to more computational costs in terms of time expecially; on the opposite a DOE approach is not defined to "find" an optimal solution and it will a least need a regression analysis to identify a possible solution space (See Figure 73). In summary, the Choice to follow a Doe+FIT+Optimization procedure starting from experimental data was made to find an effective and accurate semi-automated numerical framework that is able to determine relevant adhesive and/or joint material parameters, useful for dynamic full-vehicle simulations that are already computational expensive providing a useful tool in the design of automotive/aerospace bonded structures.

11.6.5 Repeating the procedure

The generation of a high-fidelity adhesive material card is not a monolithic task but rather a structured, multi-stage procedure. It is important to distinguish between the core methodology employed for parameter identification and the overarching procedure in which this methodology is applied.

The fundamental methodology, which has been detailed, is a three-step process orchestrated by the HyperStudy software:

- Design of Experiments (DOE): To intelligently explore the parameter space.
- Fitting (Fit): To create a computationally efficient response surface.
- Optimization: To identify the set of parameters that minimizes the error between the numerical and experimental curves.

This core methodology drives the calibration. However, to ensure both accuracy and computational efficiency, it is applied iteratively within a four-stage procedure. Each stage builds upon the last, progressively refining the material card parameters by focusing on different aspects of the joint's behavior. The procedure is structured as follows:

Stage 1: SLJ Coarse Optimization. An initial optimization is performed on the SLJ model using wide parameter ranges. The objective of this phase is not to find the final values in shear direction, but to go near the best solution with less computational possible efforts exploring a wide range of possible variable sets.

Stage 2: SLJ Fine Optimization. Based on the insights from the coarse optimization, the parameter ranges are narrowed and a second more focused optimization is performed on the SLJ model. This stage aims to precisely calibrate the constitutive parameters governing the adhesive's behavior under shear loading.

Now, making use of the shear conditions analysis, the numbers that represent properties at Mode II loading conditions can be fixed and discarded from the variables set, making lighter the future simulations and getting closer to the material card generation.

Stage 3: DCB Stiffness Analysis. This is a targeted optimization focused only on the initial linear-elastic portion of the DCB test curve (typically the first 2-3 mm of displacement – See Figure 74 and Figure 75). By isolating this region, the tensile traction stiffness parameters of the cohesive law can be calibrated efficiently, as the simulations are extremely fast. This is a critical step, as the initial stiffness significantly influences the subsequent prediction of damage initiation.

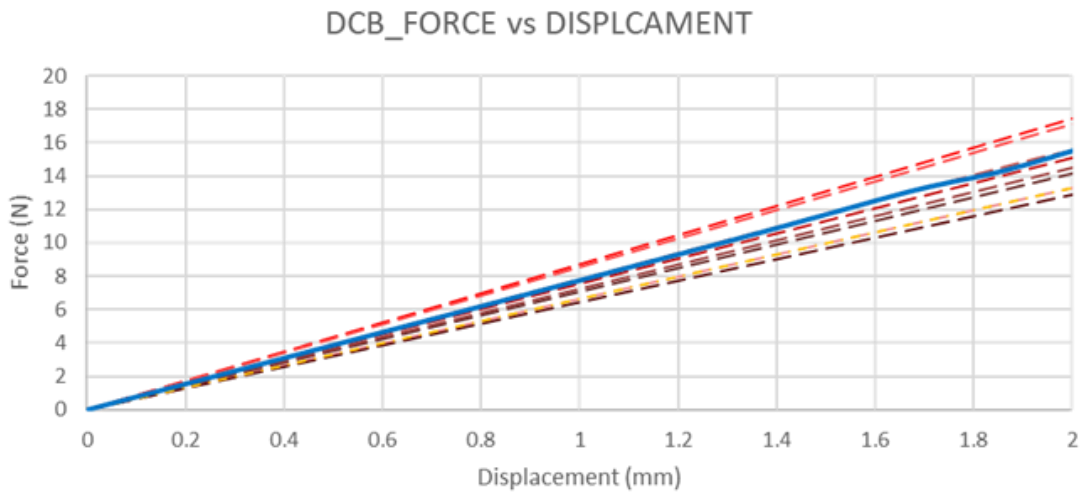

Figure 74: Initial linear trait selected for DCB first stiffness analysis

Stage 4: DCB Full-Curve Fine Optimization. The final stage involves a fine optimization on the complete force-displacement curve of the DCB model. Using the stiffness values determined in Stage 3 as a fixed starting point, this phase aims to precisely calibrate the parameters governing Mode I damage initiation and fracture propagation.

To avoid redundancy, the previous discussions were focused on the specific inputs and calibrated outcomes of each of the four stages.

Results from the Optimization procedure are clearly visible in Figure 76, with comparable curves trend and overall behavior of the numerical model compared to the experimental starting dataset. Once the procedure is complete, a set of 7 values should be obtained (E1, E2, T1, T2, G1, G2, DEGRAD). The properties in dir3 are defined as the same as those in dir2) which then represent the material card of the adhesive, generated from the experimental data of certain types of tests and calibrated on a specific mesh cut.

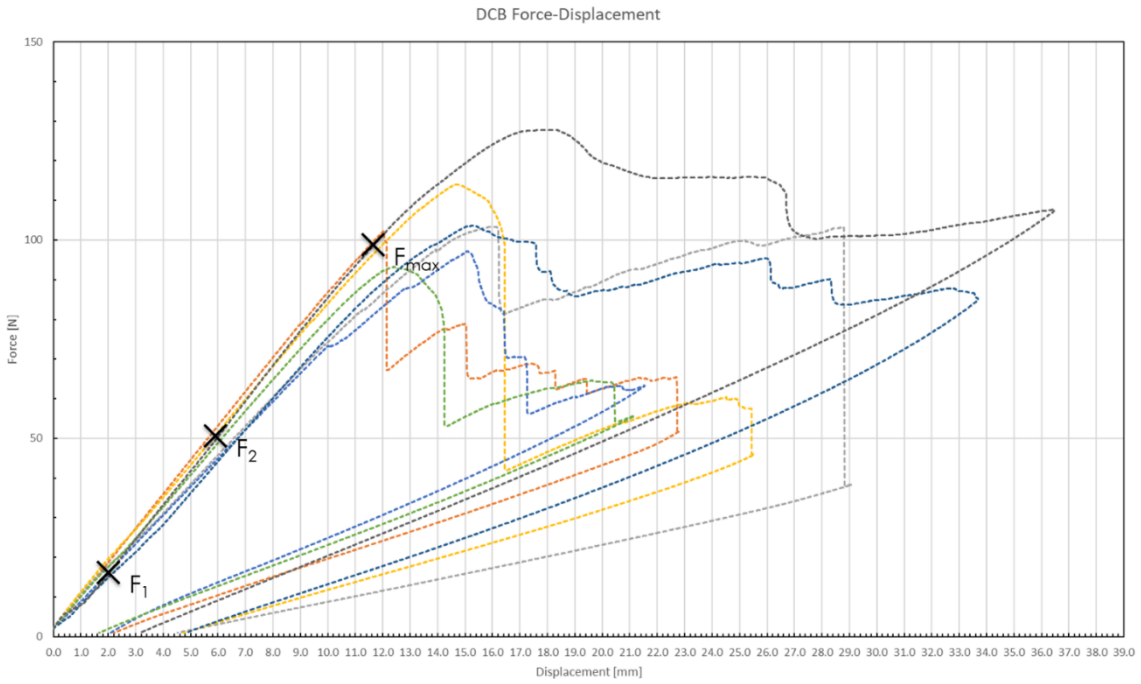

Figure 75: Marks of the output point of interest for the refinement analysis.

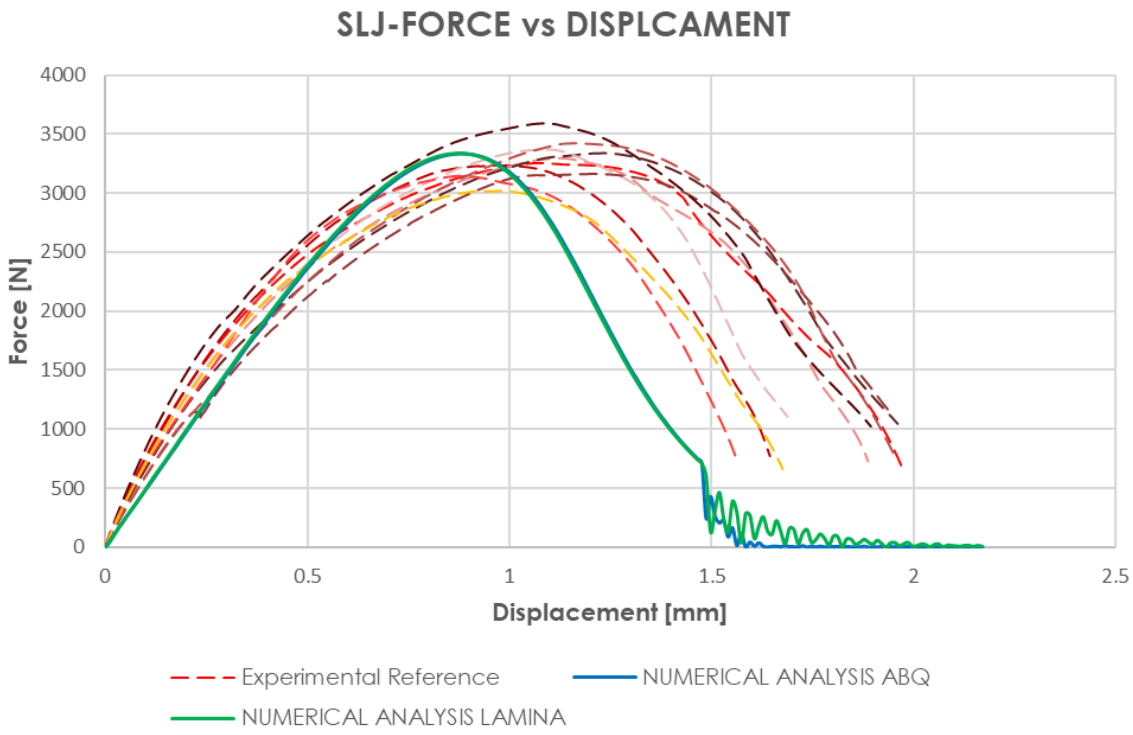

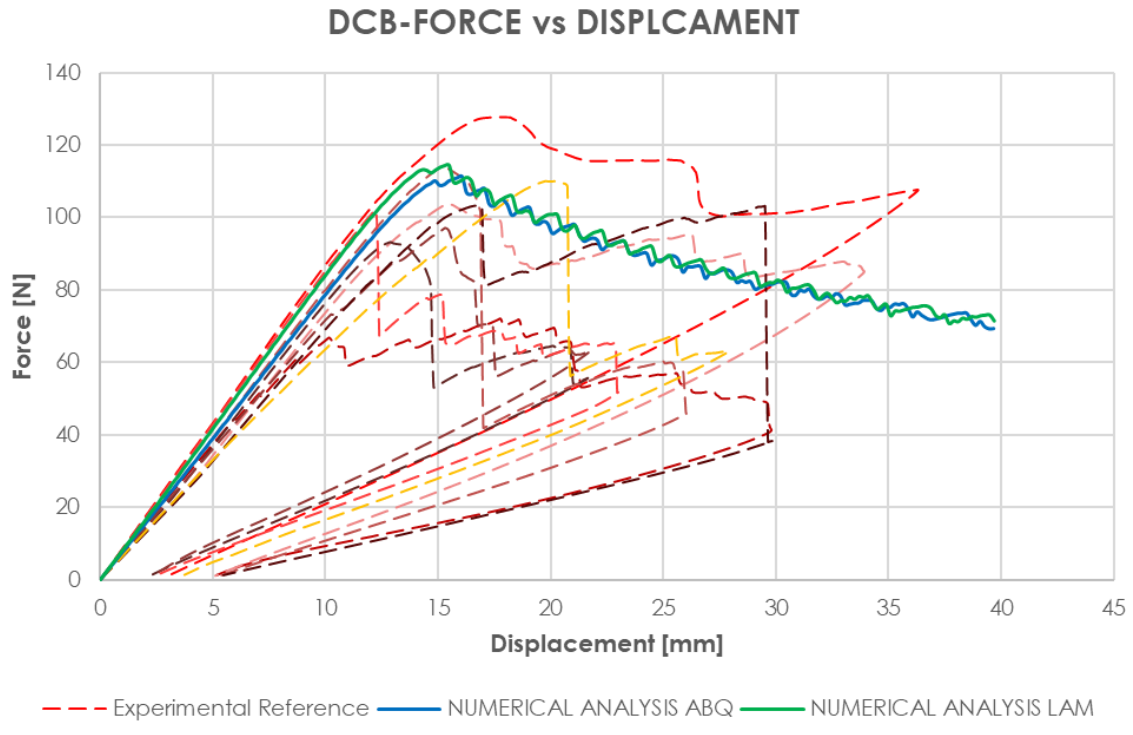

Figure 76: Results from optimization procedure based on experimental data from test specimens and numerical modeling

Chapter 12: Final Conclusions

This doctoral research successfully developed, validated and demonstrated an integrated methodology for the experimental characterization, modeling and numerical calibration of structural adhesively bonded joints, focusing on polyurethane adhesives to Carbon SMC composite joints. The work combined a systematic multi-scale experimental campaign with advanced data-driven modeling and optimization routines for generating accurate adhesive material cards suitable for finite element applications.

A series of dedicated experimental campaigns were conducted to progressively isolate and understand the mechanical behavior of the adhesive–substrate system.

The preliminary geometric investigation established the fundamental parameters for the testing methodology and revealed the key role of surface preparation in determining failure mode and joint stiffness.

The adhesive gap campaign confirmed that bondline thickness significantly affects joint strength and toughness. Optimum mechanical performance was achieved for gap was 1.5 mm, where ductility and energy absorption were maximized without excessive stress localization.

The temperature campaign demonstrated the strong thermo-mechanical sensitivity of the polyurethane adhesive: joints exhibited increased stiffness and substrate tearing at low temperature, ductile response at room temperature and a sharp degradation in both stiffness and fracture energy at high temperature due to polymer softening near the glass transition region.

When changing the adherend type, glass–SMC substrates showed inferior performance due to matrix-dominated fracture and low interlaminar strength, whereas hybrid aluminum–SMC joints provided more representative results of the adhesive's intrinsic capacity, showing clean cohesive or adhesive failures and a realistic shear strength of about 8 MPa.

The mixed-mode and fatigue campaigns provided crucial insights into complex and cyclic loading. Mixed-mode tests demonstrated that failure was dominated by SMC bending rather than adhesive cracking, confirming the adhesive's robustness even under multi-axial stress states.

Fatigue tests, supported by digital image correlation, revealed crack initiation directly at the interface, validating cohesive zone assumptions and providing essential data for durability modeling.

Finally, bulk adhesive characterization defined the intrinsic material properties (tensile strength of 15 MPa, strain at break of 38% and fracture energy of approximately 2000 J/m²) establishing the baseline mechanical response for cohesive law calibration and validation.

A key contribution of this thesis is the formulation of a semi-automatic, physically grounded material card generation procedure for structural adhesives. The procedure integrates:

1. Experimental data acquisition
2. Inverse parameter identification through optimization of cohesive zone model (CZM) parameters
3. Finite element validation against independent experimental results (e.g., DCB and SLJ joints).

This procedure allows cohesive parameters such as stiffness, strength and fracture energy to be extracted in a reproducible manner, minimizing user dependence. The resulting material cards were implemented and validated in commercial CAE software environments (Abaqus/Explicit), demonstrating excellent agreement between simulation and experiment across all configurations.

From a scientific standpoint, this research provides one of the most comprehensive experimental–numerical frameworks. It addresses a major gap in the literature by linking physical characterization to validated numerical tools for industrial simulation. From an industrial perspective, the developed material card generation methodology enables efficient, reliable digital validation of bonded joints in full-vehicle simulations, reducing experimental effort, cost and time in product development cycles.

The ability to predict joint stiffness, peak load and failure mode under arbitrary loading conditions using a calibrated cohesive model represents a significant advancement for the virtual design of composite structures:

- The mechanical behavior of the studied polyurethane adhesive is highly dependent on temperature, bondline thickness and substrate properties, yet consistently exhibits ductile and energy-absorbing behavior under structural loading.
- The failure mechanisms transition from cohesive to adhesive depending on surface preparation and adherend type, emphasizing the importance of interface engineering.

- The developed CZM-based material card procedure accurately reproduces experimental results and can be generalized to other adhesive systems with minimal experimental input.
- The combined experimental–numerical workflow provides a validated and transferable digital material representation of the adhesive, enabling predictive modeling of SMC composite joints under both static and dynamic conditions.

Future work will focus on extending the methodology to rate-dependent and fatigue degradation laws, as well as implementing environmental sensitivity functions to fully capture long-term adhesive durability. These advancements will further enhance the predictive capability of cohesive models, supporting the transition from empirical testing to simulation-driven adhesive joint design in sustainable lightweight structures.

Bibliography

[1] Banea MD, Da Silva LFM. Adhesively bonded joints in composite materials: An overview. Proceedings of the Institution of Mechanical Engineers, Part L: Journal of Materials: Design and Applications 2009;223:1–18. https://doi.org/10.1243/14644207JMDA219.

[2] Ashcroft IA, Hughes DJ, Shaw SJ. Adhesive bonding of fibre reinforced polymer composite materials. Assembly Automation 2006;20:150–61. https://doi.org/10.1108/01445150010321797.

[3] Bodjona K, Lessard L. Hybrid bonded-fastened joints and their application in composite structures: A general review. Journal of Reinforced Plastics and Composites 2016;35:764–81. https://doi.org/10.1177/0731684415627296.

[4] Mazumdar SK, Mallick PK. Static and fatigue behavior of adhesive joints in SMC-SMC composites. Polym Compos 1998;19:139–46. https://doi.org/10.1002/pc.10084.

[5] Sun X, Engler-Pinto C, Huang L, Huang S, Tang H, Cui H,Investigation of Mechanical Behavior of Chopped Carbon Fiber Reinforced Sheet Molding Compound (SMC) Composites. SAE Technical Papers 2020;2020-April:1–10. https://doi.org/10.4271/2020-01-1307.

[6] Romanenko V, Duhovic M, Schommer D, Hausmann J, Eschl J. Advanced process simulation of compression molded carbon fiber sheet molding compound (C-SMC) parts in automotive series applications. Compos Part A Appl Sci Manuf 2022;157:106924. https://doi.org/10.1016/j.compositesa.2022.106924.

[7] Chen B, Dillard DA. Numerical analysis of directionally unstable crack propagation in adhesively bonded joints. Int J Solids Struct 2001;38:6907–24. https://doi.org/10.1016/S0020-7683(01)00006-3.

[8] Matthews FL, Kilty PF, Godwin EW. A review of the strength of joints in fibre-reinforced plastics. Part 2. Adhesively bonded joints. Composites 1982;13:29–37. https://doi.org/10.1016/0010-4361(82)90168-9.

[9] Godwin EW, Matthews FL. A review of the strength of joints in fibre-reinforced plastics. Part 1. Mechanically fastened joints. Composites 1980;11:155–60. https://doi.org/10.1016/0010-4361(80)90008-7.

[10] Tiefenthaler M, Stelzer PS, Chung CN, Reisecker V, Major Z. Characterization of the fracture mechanical behavior of C-SMC materials. 16th Youth Symposium on Experimental Solid Mechanics, YSESM 2018 2018:1–5. https://doi.org/10.14311/APP.2018.18.0001.

[11] Aliha MRM, Kucheki HG, Berto F. Numerical analysis of crack initiation angles and propagation paths in adhesively bonded joints under mixed mode I/II loading using a novel test specimen. Procedia Structural Integrity 2021;39:393–402. https://doi.org/10.1016/j.prostr.2022.03.108.

[12] Adams R, Cawley P. A review of defect types and nondestructive testing techniques for composites and bonded joints. NDT and E International 1988;21:208–22. https://doi.org/10.1016/0963-8695(88)90113-2.

[13] Adams RD. Strength predictions for lap joints, especially with composite adherends. A review. J Adhes 1989;30:219–42. https://doi.org/10.1080/00218468908048207.

[14] Alfred Franklin V, Christopher T. Fracture energy estimation of DCB specimens made of glass/epoxy: An experimental study. Advances in Materials Science and Engineering 2013;2013. https://doi.org/10.1155/2013/412601.

[15] Budzik MK, Wolfahrt M, Reis P, Kozłowski M, Sena-Cruz J, Papadakis L,Testing mechanical performance of adhesively bonded composite joints in engineering applications: an overview. Journal of Adhesion 2022;98:2133–209. https://doi.org/10.1080/00218464.2021.1953479.

[16] Moroni F, Pirondi A, Pernechele C, Vescovi L, Collini L. Influence of material and manufacturing technology on the failure behavior of composite laminate bonded joints. Procedia Structural Integrity 2019;18:516–24. https://doi.org/10.1016/j.prostr.2019.08.195.

[17] Bernasconi A, Jamil A, Moroni F, Pirondi A. A study on fatigue crack propagation in thick composite adhesively bonded joints. Int J Fatigue 2013;50:18–25. https://doi.org/10.1016/j.ijfatigue.2012.05.018.

[18] Azari S, Jhin G, Papini M, Spelt JK. Fatigue threshold and crack growth rate of adhesively bonded joints as a function of load/displacement ratio. Compos Part A Appl Sci Manuf 2014;57:59–66. https://doi.org/10.1016/j.compositesa.2013.11.001.

[19] Blackman B, Kinloch A. Fracture tests on structural adhesive joints. European Structural Integrity Society 2001;28:225–67. https://doi.org/10.1016/S1566-1369(01)80036-4.

[20] Li J, Yan Y, Zhang T, Liang Z. Experimental study of adhesively bonded CFRP joints subjected to tensile loads. Int J Adhes Adhes 2015;57:95–104. https://doi.org/10.1016/j.ijadhadh.2014.11.001.

[21] Asgari Mehrabadi F. Experimental and numerical failure analysis of adhesive composite joints. International Journal of Aerospace Engineering 2012;2012. https://doi.org/10.1155/2012/925340.

[22] Marzi S, Biel A, Stigh U. On experimental methods to investigate the effect of layer thickness on the fracture behavior of adhesively bonded joints. Int J Adhes Adhes 2011;31:840–50. https://doi.org/10.1016/j.ijadhadh.2011.08.004.

[23] Yang S, Xu W, Liang L, Wang T, Wei Y. An experimental study on the dependence of the strength of adhesively bonded joints with thickness and mechanical properties of the adhesives. J Adhes Sci Technol 2014;28:1055–71. https://doi.org/10.1080/01694243.2014.884753.

[24] Moroni F, Pirondi A. Cohesive zone model simulation of fatigue debonding along interfaces. Procedia Eng 2011;10:1829–34. https://doi.org/10.1016/j.proeng.2011.04.304.

[25] Heide-Jørgensen S, Teixeira de Freitas S, Budzik MK. On the fracture behaviour of CFRP bonded joints under mode I loading: Effect of supporting carrier and interface contamination. Compos Sci Technol 2018;160:97–110. https://doi.org/10.1016/j.compscitech.2018.03.024.

[26] Azevedo JCS, Campilho RDSG, da Silva FJG, Faneco TMS, Lopes RM. Cohesive law estimation of adhesive joints in mode II condition. Theoretical and Applied Fracture Mechanics 2015;80:143–54. https://doi.org/10.1016/j.tafmec.2015.09.007.

[27] Floros IS, Tserpes KI, Löbel T. Mode-I, mode-II and mixed-mode I+II fracture behavior of composite bonded joints: Experimental characterization and numerical simulation. Compos B Eng 2015;78:459–68. https://doi.org/10.1016/j.compositesb.2015.04.006.

[28] Cañas J, Justo J, París F. Evaluation of the interlaminar fracture toughness on composite materials using DCB test on symmetric and unsymmetric configurations. Compos Struct 2022;297:1–12. https://doi.org/10.1016/j.compstruct.2022.115944.

[29] Costa M, Viana G, Créac'hcadec R, da Silva LFM, Campilho RDSG. A cohesive zone element for mode I modelling of adhesives degraded by humidity and fatigue. Int J Fatigue 2018;112:173–82. https://doi.org/10.1016/j.ijfatigue.2018.03.014.

[30] Jia Z, Yuan G, Hui D, Feng X, Zou Y. Effect of high strain rate and low temperature on mode II fracture toughness of ductile adhesive. Int J Adhes Adhes 2018;86:105–12. https://doi.org/10.1016/j.ijadhadh.2018.09.003.

[31] Da Silva LFM, De Magalhães FACRG, Chaves FJP, De Moura MFSF. Mode II fracture toughness of a brittle and a ductile adhesive as a function of the adhesive thickness. Journal of Adhesion 2010;86:891–905. https://doi.org/10.1080/00218464.2010.506155.

[32] Bernasconi A, Lima RAA, Cardamone S, Campbell RB, Slocum AH, Giglio M. Effect of temperature on cohesive modelling of 3M Scotch-Weld™ 7260 B/A epoxy adhesive. Journal of Adhesion 2020;96:437–60. https://doi.org/10.1080/00218464.2019.1665519.

[33] Manterola J, Cabello M, Zurbitu J, Renart J, Turon A, Jumel J,Effect of the width-to-thickness ratio on the mode I fracture toughness of flexible bonded joints. Eng Fract Mech 2019;218:106584. https://doi.org/10.1016/j.engfracmech.2019.106584.

[34] Ni J, Min J, Wan H, Lin J, Wang S, Wan Q. Effect of adhesive type on mechanical properties of galvanized steel/SMC adhesive-bonded joints. Int J Adhes Adhes 2020;97:102482. https://doi.org/10.1016/j.ijadhadh.2019.102482.

[35] Saleh MN, Budzik MK, Saeedifar M, Zarouchas D, Teixeira De Freitas S. On the influence of the adhesive and the adherend ductility on mode I fracture characterization of thick adhesively-bonded joints. Int J Adhes Adhes 2022;115:103123. https://doi.org/10.1016/j.ijadhadh.2022.103123.

[36] Springer GS, Wang TK. Creep, Strength and Moisture Absorption of Adhesive Bonded FRP Joints. Journal of Reinforced Plastics and Composites 1985;4:212–25. https://doi.org/10.1177/073168448500400206.

[37] Stigh U andersson T. An experimental method to determine the complete stress-elongation relation for a structural adhesive layer loaded in peel. European Structural Integrity Society 2000;27:297–306. https://doi.org/10.1016/S1566-1369(00)80026-6.

[38] Wang WX, Nakata M, Takao Y, Matsubara T. Experimental investigation on test methods for mode II interlaminar fracture testing of carbon fiber reinforced composites. Compos Part A Appl Sci Manuf 2009;40:1447–55. https://doi.org/10.1016/j.compositesa.2009.04.029.

[39] Wang W, Lopes Fernandes R, Teixeira De Freitas S, Zarouchas D, Benedictus R. How pure mode I can be obtained in bi-material bonded DCB joints: A longitudinal strain-based criterion. Compos B Eng 2018;153:137–48. https://doi.org/10.1016/j.compositesb.2018.07.033.

[40] Carlberger T, Stigh U. Influence of layer thickness on cohesive properties of an epoxy-based adhesive-an experimental study. Journal of Adhesion 2010;86:816–35. https://doi.org/10.1080/00218464.2010.498718.

[41] Banea MD, Da Silva LFM, Campilho RDSG. The effect of adhesive thickness on the mechanical behavior of a structural polyurethane adhesive. Journal of Adhesion 2014;91:331–46. https://doi.org/10.1080/00218464.2014.903802.

[42] Mall S, Ramamurthy G. Effect of bond thickness on fracture and fatigue strength of adhesively bonded composite joints. Int J Adhes Adhes 1989;9:11. https://doi.org/10.1016/0143-7496(89)90135-8.

[43] Wu Z, Yuan H, Niu H. Stress Transfer and Fracture Propagation in Different Kinds of Adhesive Joints. J Eng Mech 2002;128:562–73. https://doi.org/10.1061/(asce)0733-9399(2002)128:5(562).

[44] Tamborrino R, Palumbo D, Galietti U, Aversa P, Chiozzi S, Luprano VAM. Assessment of the effect of defects on mechanical properties of adhesive bonded joints by using non destructive methods. Compos B Eng 2016;91:337–45. https://doi.org/10.1016/j.compositesb.2016.01.059.

[45] Xu W, Wei Y. Influence of adhesive thickness on local interface fracture and overall strength of metallic adhesive bonding structures. Int J Adhes Adhes 2013;40:158–67. https://doi.org/10.1016/j.ijadhadh.2012.07.012.

[46] Yan C, Mai YW, Ye L. Effect of bond thickness on fracture behaviour in adhesive joints. Journal of Adhesion 2001;75:27–44. https://doi.org/10.1080/00218460108029592.

[47] Shah OR, Tarfaoui M. Effect of adhesive thickness on the Mode i and II strain energy release rates. Comparative study between different approaches for the calculation of Mode i and II SERR's. Compos B Eng 2016;96:354–63. https://doi.org/10.1016/j.compositesb.2016.04.042.

[48] Liao L, Huang C, Sawa T. Effect of adhesive thickness, adhesive type and scarf angle on the mechanical properties of scarf adhesive joints. Int J Solids Struct 2013;50:4333–40. https://doi.org/10.1016/j.ijsolstr.2013.09.005.

[49] Gulino M, Moroni F, Pirondi A. Metal-metal and metal-composite joints with 3D printed aluminium substrates: effect of surface treatment on the mode I fracture toughness. Journal of Adhesion 2025;101:115–43. https://doi.org/10.1080/00218464.2023.2285074.

[50] Oshima S, Yoshimura A, Hirano Y, Ogasawara T. Experimental method for mode I fracture toughness of composite laminates using wedge loaded double cantilever beam specimens. Compos Part A Appl Sci Manuf 2018;112:119–25. https://doi.org/10.1016/j.compositesa.2018.05.036.

[51] Merzkirch M, Powell LA, Foecke T. Measurements of mode I interlaminar properties of carbon fiber reinforced polymers using digital image correlation. Key Eng Mater 2017;742 KEM:652–9. https://doi.org/10.4028/www.scientific.net/KEM.742.652.

[52] Hu P, Han X, Da Silva LFM, Li WD. Strength prediction of adhesively bonded joints under cyclic thermal loading using a cohesive zone model. Int J Adhes Adhes 2013;41:6–15. https://doi.org/10.1016/j.ijadhadh.2012.10.009.

[53] Cabello M, Zurbitu J, Renart J, Turon A, Martínez F. A general analytical model based on elastic foundation beam theory for adhesively bonded DCB joints either with flexible or rigid adhesives. Int J Solids Struct 2016;94–95:21–34. https://doi.org/10.1016/j.ijsolstr.2016.05.011.

[54] Fernández-Cañadas LM, Ivañez I, Sanchez-Saez S, Barbero EJ. Effect of adhesive thickness and overlap on the behavior of composite single-lap joints. Mechanics of Advanced Materials and Structures 2021;28:1111–20. https://doi.org/10.1080/15376494.2019.1639086.

[55] Davies P, Sohier L, Cognard JY, Bourmaud A, Choqueuse D, Rinnert E,Influence of adhesive bond line thickness on joint strength. Int J Adhes Adhes 2009;29:724–36. https://doi.org/10.1016/j.ijadhadh.2009.03.002.

[56] Tankut N. The effect of adhesive type and bond line thickness on the strength of mortise and tenon joints. Int J Adhes Adhes 2007;27:493–8. https://doi.org/10.1016/j.ijadhadh.2006.07.003.

[57] Wang Z, Li C, Sui L, Xian G. Effects of adhesive property and thickness on the bond performance between carbon fiber reinforced polymer laminate and steel. Thin-Walled Structures 2021;158:107176. https://doi.org/10.1016/j.tws.2020.107176.

[58] Lopes Fernandes R, Budzik MK, Benedictus R, Teixeira de Freitas S. Multi-material adhesive joints with thick bond-lines: Crack onset and crack deflection. Compos Struct 2021;266. https://doi.org/10.1016/j.compstruct.2021.113687.

[59] Armanios E, Bucinell R, Wilson D, Tomblin J, Harter P, Seneviratne W,Characterization of Bondline Thickness Effects in Adhesive Joints. Journal of Composites Technology and Research 2002;24:80. https://doi.org/10.1520/ctr10972j.

[60] Chen B, Dillard DA, Dillard JG, Clark RL. Crack path selection in adhesively-bonded joints: The role of material properties. Journal of Adhesion 2001;75:405–34. https://doi.org/10.1080/00218460108029613.

[61] Moslemi M, Khoshravan M. Cohesive zone parameters selection for mode-i prediction of interfacial delamination. Strojniski Vestnik/Journal of Mechanical Engineering 2015;61:507–16. https://doi.org/10.5545/sv-jme.2015.2521.

[62] Sekiguchi Y, Katano M, Sato C. Experimental study of the Mode I adhesive fracture energy in DCB specimens bonded with a polyurethane adhesive. Journal of Adhesion 2017;93:235–55. https://doi.org/10.1080/00218464.2015.1070101.

[63] Tang JH, Sridhar I, Srikanth N. Static and fatigue failure analysis of adhesively bonded thick composite single lap joints. Compos Sci Technol 2013;86:18–25. https://doi.org/10.1016/j.compscitech.2013.06.018.

[64] Yamada SE. Elastic/plastic fracture analysis for bonded joints. Eng Fract Mech 1987;27:315–28. https://doi.org/10.1016/0013-7944(87)90149-4.

[65] Devries KL, Borgmeier P. Testing of Adhesive Joints. Mechanical Testing and Evaluation 2018;8:836–44. https://doi.org/10.31399/asm.hb.v08.a0003324.

[66] Canãs J, Távara L, Blázquez A, Estefani A. Overview of Gc Tests Used to Evaluate Composite-Composite Adhesive Joints. Journal of Multiscale Modelling 2019;10:1–14. https://doi.org/10.1142/S1756973718420027.

[67] da Silva LFM, Campilho RDSG. Design of adhesively-bonded composite joints. Elsevier Ltd; 2015. https://doi.org/10.1016/B978-0-85709-806-1.00002-1.

[68] da Silva LFM, Dillard DA, Blackman B, Adams RD. Testing Adhesive Joints: Best Practices. 2012. https://doi.org/10.1002/9783527647026.

[69] Budhe S, Banea MD, de Barros S, da Silva LFM. An updated review of adhesively bonded joints in composite materials. Int J Adhes Adhes 2017;72:30–42. https://doi.org/10.1016/j.ijadhadh.2016.10.010.

[70] Jahn J, Weber M, Boehner J, Steinhilper R. Assessment Strategies for Composite-metal Joining Technologies-A Review. Procedia CIRP 2016;50:689–94. https://doi.org/10.1016/j.procir.2016.05.034.

[71] Blanco N, Gamstedt EK, Costa J. Mechanical hinge system for delamination tests in beam-type composite specimens. Compos Sci Technol 2008;68:1837–42. https://doi.org/10.1016/j.compscitech.2008.01.011.

[72] Nemati Giv A, Ayatollahi MR, Ghaffari SH, da Silva LFM. Effect of reinforcements at different scales on mechanical properties of epoxy adhesives and adhesive joints: a review. Journal of Adhesion 2018;94:1082–121. https://doi.org/10.1080/00218464.2018.1452736.

[73] Maggiore S, Banea MD, Stagnaro P, Luciano G. A review of structural adhesive joints in hybrid joining processes. Polymers (Basel) 2021;13. https://doi.org/10.3390/polym13223961.

[74] dos Reis MQ, Banea MD, da Silva LFM, Carbas RJC. Mechanical characterization of a modern epoxy adhesive for automotive industry. Journal of the Brazilian Society of Mechanical Sciences and Engineering 2019;41:1–11. https://doi.org/10.1007/s40430-019-1844-2.

[75] Martínez-Landeros VH, Vargas-Islas SY, Cruz-González CE, Barrera S, Mourtazov K, Ramírez-Bon R. Studies on the influence of surface treatment type, in the effectiveness of structural adhesive bonding, for carbon fiber reinforced composites. J Manuf Process 2019;39:160–6. https://doi.org/10.1016/j.jmapro.2019.02.014.

[76] Zhang Y, Luo R, Zhang J, Xiang Q. The reinforcing mechanism of carbon fiber in composite adhesive for bonding carbon/carbon composites. J Mater Process Technol 2011;211:167–73. https://doi.org/10.1016/j.jmatprotec.2010.08.028.

[77] Cheng F, Hu Y, Zhang X, Hu X, Huang Z. Adhesive bond strength enhancing between carbon fiber reinforced polymer and aluminum substrates with different surface morphologies created by three sulfuric acid solutions. Compos Part A Appl Sci Manuf 2021;146:106427. https://doi.org/10.1016/j.compositesa.2021.106427.

[78] Wang S, Min J, Lin J, Sun C, Yang S. Effect of Atmospheric Pressure Plasma Treatment on the Lap-Shear Strength of Adhesive-Bonded Sheet Molding Compound Joints. Automotive Innovation 2018;1:237–46. https://doi.org/10.1007/s42154-018-0027-7.

[79] Qiao Y, Shin Y, Ramos JL, Engelhard MH, Seffens RJ, Merkel DR,Plasma treatment on both adhesive tape and adherends for significantly enhanced CFRTP-related adhesive joints. Appl Surf Sci 2024;649:159092. https://doi.org/10.1016/j.apsusc.2023.159092.

[80] Pástor M, Hagara M. A comparison of modern and classical experimental methods of mechanics in strain investigation. Applied Mechanics and Materials 2014;611:501–5. https://doi.org/10.4028/www.scientific.net/AMM.611.501.

[81] Lin J, Sun C, Min J, Wan H, Wang S. Effect of atmospheric pressure plasma treatment on surface physicochemical properties of carbon fiber reinforced polymer and its interfacial bonding strength with adhesive. Compos B Eng 2020;199:108237. https://doi.org/10.1016/j.compositesb.2020.108237.

[82] Dillard JG, Spinu IM. An investigation of the effect of plasma treatment on the surface properties and adhesion in sheet molded composite (smc) material. J Adhes 1990;31:137–59. https://doi.org/10.1080/00218469008048221.

[83] Lopes Fernandes R, Teixeira de Freitas S, Budzik MK, Poulis JA, Benedictus R. From thin to extra-thick adhesive layer thicknesses: Fracture of bonded joints under mode I loading conditions. Eng Fract Mech 2019;218:106607. https://doi.org/10.1016/j.engfracmech.2019.106607.

[84] Rośkowicz M, Godzimirski J, Komorek A, Jasztal M. The effect of adhesive layer thickness on joint static strength. Materials 2021;14:1–14. https://doi.org/10.3390/ma14061499.

[85] Campilho RDSG, Moura DC, Banea MD, Da Silva LFM. Adhesive thickness effects of a ductile adhesive by optical measurement techniques. Int J Adhes Adhes 2015;57:125–32. https://doi.org/10.1016/j.ijadhadh.2014.12.004.

[86] Yudhanto A, Almulhim M, Kamal F, Tao R, Fatta L, Alfano M,Enhancement of fracture toughness in secondary bonded CFRP using hybrid thermoplastic/thermoset bondline architecture. Compos Sci Technol 2020;199:108346. https://doi.org/10.1016/j.compscitech.2020.108346.

[87] Borges CSP, Nunes PDP, Akhavan A, Marques EAS, Carbas RJC, Alfonso L,Influence of mode mixity and loading rate on the fracture behaviour of crash resistant adhesives. Theoretical and Applied Fracture Mechanics 2020;107:102508. https://doi.org/10.1016/j.tafmec.2020.102508.

[88] Chai H. Bond thickness effect in mixed-mode fracture and its significance to delamination resistance. Int J Solids Struct 2021;219–220:63–80. https://doi.org/10.1016/j.ijsolstr.2021.03.006.

[89] Costa M, Carbas R, Marques E, Viana G, da Silva LFM. An apparatus for mixed-mode fracture characterization of adhesive joints. Theoretical and Applied Fracture Mechanics 2017;91:94–102. https://doi.org/10.1016/j.tafmec.2017.04.014.

[90] Carrere N, Martin E, Leguillon D. Comparison between models based on a coupled criterion for the prediction of the failure of adhesively bonded joints. Eng Fract Mech 2015;138:185–201. https://doi.org/10.1016/j.engfracmech.2015.03.004.

[91] Gheibi MR, Shojaeefard MH, Saeidi Googarchin H. A comparative study on the fracture energy determination theories for an automotive structural adhesive: Experimental and numerical investigation. Eng Fract Mech 2019;212:13–27. https://doi.org/10.1016/j.engfracmech.2019.03.019.

[92] Chen Q, Guo H, Avery K, Su X, Kang H. Fatigue performance and life estimation of automotive adhesive joints using a fracture mechanics approach. Eng Fract Mech 2017;172:73–89. https://doi.org/10.1016/j.engfracmech.2017.01.005.

[93] Ribeiro FMF, Campilho RDSG, Carbas RJC, da Silva LFM. Strength and damage growth in composite bonded joints with defects. Compos B Eng 2016;100:91–100. https://doi.org/10.1016/j.compositesb.2016.06.060.

[94] Anyfantis KN, Tsouvalis NG. A novel traction-separation law for the prediction of the mixed mode response of ductile adhesive joints. Int J Solids Struct 2012;49:213–26. https://doi.org/10.1016/j.ijsolstr.2011.10.001.

[95] Teixeira JMD, Campilho RDSG, Silva FJG, Moreira FJP, Silva DFO. Comparative evaluation of different fracture tests for the tensile fracture toughness of a ductile adhesive. Procedia Manuf 2019;38:1268–75. https://doi.org/10.1016/j.promfg.2020.01.221.

[96] Moroni F, Pirondi A. A procedure for the simulation of fatigue crack growth in adhesively bonded joints based on the cohesive zone model and different mixed-mode propagation criteria. Eng Fract Mech 2011;78:1808–16. https://doi.org/10.1016/j.engfracmech.2011.02.004.

[97] Pirondi A, Moroni F. Improvement of a cohesive zone model for fatigue delamination rate simulation. Materials 2019;12. https://doi.org/10.3390/ma12010181.

[98] Di Caprio F, Saputo S, Sellitto A. Numerical-Experimental Correlation of Interlaminar Damage Growth in Composite Structures: Setting Cohesive Zone Model Parameters. Advances in Materials Science and Engineering 2019;2019. https://doi.org/10.1155/2019/2150921.

[99] Chen CR, Mai YW. Comparison of cohesive zone model and linear elastic fracture mechanics for a mode I crack near a compliant/stiff interface. Eng Fract Mech 2010;77:3408–17. https://doi.org/10.1016/j.engfracmech.2010.09.009.

[100] Krueger R. Virtual crack closure technique: History, approach and applications. Appl Mech Rev 2004;57:109–43. https://doi.org/10.1115/1.1595677.

[101] Nojavan S, Schesser D, Yang QD. A two-dimensional in situ fatigue cohesive zone model for crack propagation in composites under cyclic loading. Int J Fatigue 2016;82:449–61. https://doi.org/10.1016/j.ijfatigue.2015.08.029.

[102] Chen Q, Guo H, Avery K, Kang H, Su X. Mixed-mode fatigue crack growth and life prediction of an automotive adhesive bonding system. Eng Fract Mech 2018;189:439–50. https://doi.org/10.1016/j.engfracmech.2017.11.004.

[103] Giuliese G, Pirondi A, Moroni F. A Cohesive Zone Model for Three-dimensional Fatigue Debonding/Delamination. Procedia Materials Science 2014;3:1473–8. https://doi.org/10.1016/j.mspro.2014.06.238.

[104] Moazzami M, Akhavan-Safar A, Ayatollahi MR, Poulis JA, da Silva LFM, Teixeira De Freitas S. A degradable mode I cohesive zone model developed for damage and fracture analysis of dissimilar composite/metal adhesive joints subjected to cyclic ageing conditions. Theoretical and Applied Fracture Mechanics 2023;127:104076. https://doi.org/10.1016/j.tafmec.2023.104076.

[105] Jaillon A, Jumel J, Lachaud F, Paroissien E. Mode I cohesive zone model parameters identification and comparison of measurement techniques based on uncertainty estimation. Int J Solids Struct 2020;191–192:577–87. https://doi.org/10.1016/j.ijsolstr.2019.12.014.

[106] Law VJ, Mohan J, O'Neill FT, Ivankovic A, Dowling DP. Air based atmospheric pressure plasma jet removal of FreKote 710-NC prior to composite-to-composite adhesive bonding. Int J Adhes Adhes 2014;54:72–81. https://doi.org/10.1016/j.ijadhadh.2014.05.001.

[107] Valoroso N, Sessa S, Lepore M, Cricrì G. Identification of mode-I cohesive parameters for bonded interfaces based on DCB test. Eng Fract Mech 2013;104:56–79. https://doi.org/10.1016/j.engfracmech.2013.02.008.

[108] Pascoe JA, Alderliesten RC, Benedictus R. Methods for the prediction of fatigue delamination growth in composites and adhesive bonds - A critical review. Eng Fract Mech 2013;112–113:72–96. https://doi.org/10.1016/j.engfracmech.2013.10.003.

[109] Mackerle J. Finite element analysis and simulation of adhesive bonding, soldering and brazing: A bibliography (1976-1996). Model Simul Mat Sci Eng 1997;5:159–85. https://doi.org/10.1088/0965-0393/5/2/006.

[110] Pardoen T, Ferracin T, Landis CM, Delannay F. Constraint effects in adhesive joint fracture. J Mech Phys Solids 2005;53:1951–83. https://doi.org/10.1016/j.jmps.2005.04.009.

[111] Alfredsson KS. On the instantaneous energy release rate of the end-notch flexure adhesive joint specimen. Int J Solids Struct 2004;41:4787–807. https://doi.org/10.1016/j.ijsolstr.2004.03.008.

[112] Blackman BRK, Kinloch AJ, Paraschi M. The determination of the mode II adhesive fracture resistance, GIIC, of structural adhesive joints: An effective crack length approach. Eng Fract Mech 2005;72:877–97. https://doi.org/10.1016/j.engfracmech.2004.08.007.

[113] Sekiguchi Y, Hayashi A, Sato C. Analytical determination of adhesive layer deformation for adhesively bonded double cantilever beam test considering elastic–plastic deformation. Journal of Adhesion 2020;96:647–64. https://doi.org/10.1080/00218464.2018.1489799.

[114] Li G, Li C. Linking bilinear traction law parameters to cohesive zone length for laminated composites and bonded joints. Adv Aircr Spacecr Sci 2014;1:177–96. https://doi.org/10.12989/aas.2014.1.2.177.

[115] Krasucki F, Münch A, Ousset Y. Numerical simulation of debonding of adhesively bonded joint. Int J Solids Struct 2002;39:6355–83. https://doi.org/10.1016/S0020-7683(02)00480-8.

[116] Budzik MK, Heide-Jørgensen S. Branching and softening of loading path during onset of crack at elastic-brittle interface. Mechanics of Materials 2018;127:1–13. https://doi.org/10.1016/j.mechmat.2018.08.013.

[117] Heide-Jørgensen S, Budzik MK. Effects of bondline discontinuity during growth of interface cracks including stability and kinetic considerations. J Mech Phys Solids 2018;117:1–21. https://doi.org/10.1016/j.jmps.2018.04.002.

[118] Ma M, Zhou Z, Jiang W, Yao W, Li P. Experimental and numerical study on DCB specimens bonded with similar and dissimilar materials. Heliyon 2022;8:e11037. https://doi.org/10.1016/j.heliyon.2022.e11037.

[119] Škec L, Alfano G, Jelenić G. Complete analytical solutions for double cantilever beam specimens with bi-linear quasi-brittle and brittle interfaces. vol. 215. 2019. https://doi.org/10.1007/s10704-018-0324-5.

[120] Cui H. Simulation of ductile adhesive failure with experimentally determined cohesive law. Compos B Eng 2016;92:193–201. https://doi.org/10.1016/j.compositesb.2016.02.018.

[121] Pirondi A, Moroni F. A progressive damage model for the prediction of fatigue crack growth in bonded joints. Journal of Adhesion 2010;86:501–21. https://doi.org/10.1080/00218464.2010.484305.

[122] Gustafson PA, Waas AM. Efficient and robust traction laws for the modeling of adhesively bonded joints. Collection of Technical Papers - AIAA/ASME/ASCE/AHS/ASC Structures, Structural Dynamics and Materials Conference 2008. https://doi.org/10.2514/6.2008-1847.

[123] Park K, Choi H, Paulino GH. Assessment of cohesive traction-separation relationships in ABAQUS: A comparative study. Mech Res Commun 2016;78:71–8. https://doi.org/10.1016/j.mechrescom.2016.09.004.

[124] Gordon TL, Fakley ME. The influence of elastic modulus on adhesion to thermoplastics and thermoset materials. Int J Adhes Adhes 2003;23:95–100. https://doi.org/10.1016/S0143-7496(02)00064-7.

[125] Scarselli G, Corcione C, Nicassio F, Maffezzoli A. Adhesive joints with improved mechanical properties for aerospace applications. Int J Adhes Adhes 2017;75:174–80. https://doi.org/10.1016/j.ijadhadh.2017.03.012.

[126] Rajan S, Sutton MA, McMakin W, Compton E, Kidane A, Gurdal Z,Characterization of Mode I and Mode II traction–separation laws for cohesive separation of uncured thermoset tows. Int J Fract 2020;221:25–38. https://doi.org/10.1007/s10704-019-00399-1.

[127] Nageswara Rao B, Acharya AR. Evaluation of fracture energy GIC using a double cantilever beam fibre composite specimen. Eng Fract Mech 1995;51:317–22. https://doi.org/10.1016/0013-7944(94)00251-C.

[128] Li H, Yuan H, Li X. Assessment of low cycle fatigue crack growth under mixed-mode loading conditions by using a cohesive zone model. Int J Fatigue 2015;75:39–50. https://doi.org/10.1016/j.ijfatigue.2015.01.008.

[129] Roth S, Kuna M. Fatigue Modelling with a Cyclic Cohesive Zone Approach. Procedia Materials Science 2014;3:325–30. https://doi.org/10.1016/j.mspro.2014.06.056.

[130] Choi H, Park K, Paulino GH. Mixed-mode fatigue crack growth using cohesive zone modeling. Eng Fract Mech 2020;240:107234. https://doi.org/10.1016/j.engfracmech.2020.107234.

[131] de Moura MFSF, Gonçalves JPM. Cohesive zone model for high-cycle fatigue of composite bonded joints under mixed-mode I+II loading. Eng Fract Mech 2015;140:31–42. https://doi.org/10.1016/j.engfracmech.2015.03.044.

[132] Suo Z, Hutchinson JW. Sandwich test specimens for measuring interface crack toughness. Materials Science and Engineering A 1989;107:135–43. https://doi.org/10.1016/0921-5093(89)90382-1.

[133] Škec L, Alfano G, Jelenić G. On Gc, Jc and the characterisation of the mode-I fracture resistance in delamination or adhesive debonding. Int J Solids Struct 2018;144–145:100–22. https://doi.org/10.1016/j.ijsolstr.2018.04.020.

[134] Pirondi A, Nicoletto G. Mixed Mode I/II fatigue crack growth in adhesive joints. Eng Fract Mech 2006;73:2557–68. https://doi.org/10.1016/j.engfracmech.2006.04.009.

[135] Penado FE. A Closed Form Solution for the Energy Release Rate of the Double Cantilever Beam Specimen with an Adhesive Layer. J Compos Mater 1993;27:383–407. https://doi.org/10.1177/002199839302700403.

[136] Figueiredo JCP, Campilho RDSG, Marques EAS, Machado JJM, da Silva LFM. Adhesive thickness influence on the shear fracture toughness measurements of adhesive joints. Int J Adhes Adhes 2018;83:15–23. https://doi.org/10.1016/j.ijadhadh.2018.02.015.

[137] International A. Standard test method for mode I interlaminar fracture toughness of unidirectional fiber-reinforced polymer matrix composites. American Standard of Testing Methods 2014;03:1–12. https://doi.org/10.1520/D5528.

[138] International A. Standard Test Method for Mixed Mode I-Mode II Interlaminar Fracture Toughness of Unidirectional Fiber Reinforced Polymer Matrix Composites. ASTM International 2006:15. https://doi.org/10.1520/D6671.

[139] International A. Standard test method for determination of the mode II interlaminar fracture toughness of unidirectional fiber-reinforced polymer matrix composites. Astm 2014:1–18. https://doi.org/10.1520/D7905.

[140] International A. Standard Test Method for Strength Properties of Adhesives in Shear by Tension Loading of Single-Lap-Joint Laminated Assemblies. American Society for Testing and Materials International 2023;02:1–4. https://doi.org/10.1520/D3165-07R14.2.

[141] International A. Standard Test Method for Tensile Properties of Plastics. ASTM Book of Standards 2001:1–13. https://doi.org/10.1520/D0638-22.1.

[142] International A. Standard Test Method for Thick-Adherend Metal Lap-Shear Joints for Determination of the Stress-Strain Behavior of Adhesives in Shear by tension loading 2005;10:1–8. https://doi.org/10.1520/D5656-10R17.2.

[143] International A. Standard test method for Tensile Strength of Adhesives by means of Bar and Rod specimens 2002;15:1–3. https://doi.org/10.1520/D2095-96R23.

[144] International A. Standard Test Methods for Plane-Strain Fracture Toughness and Strain Energy Release Rate of Plastic Materials. Annul Book of ASTM Standards 1996;99:1–9. https://doi.org/10.1520/D5045-99R07E01.2.

[145] Luo Z. Benchmark of HyperStudy Optimization Algorithms. n.d.

Finanziato dall'Unione europea- Next Generation EU, Missione 4, Componente 2, Investimento 3.3 (D.M. 117/2023) CUP J33C22001480009